Distribution Agreement

Signature:

______________________________________ _____________

Sean M. Bresler Date

Excited State: CaO, Cs, Rb

By

Sean M. Bresler
Doctor of Philosophy

Chemistry

Michael C. Heaven, Ph.D.
Advisor

R. Brian Dyer, Ph.D.
Committee Member

Francesco Evangelista, Ph.D.
Committee Member

Accepted:

Lisa A. Tedesco, Ph.D.
Dean of the James T. Laney School of Graduate Studies

Date

Excited State: CaO, Cs, Rb

By

Sean M. Bresler
B.S., Chemistry, Miami University, 2012
B.A., Mathematics, Miami University, 2012

Advisor: Michael C. Heaven, Ph.D.

An abstract of
A dissertation submitted to the Faculty of the
James T. Laney School of Graduate Studies of Emory University
in partial fulfillment of the requirements for the degree of
Doctor of Philosophy
in Chemistry
2021

Abstract

Excited State: CaO, Cs, Rb

By Sean M. Bresler

Investigation of Rb, Cs, and CaO using gas phase spectroscopy will be described. These molecules have been studied using the following techniques: laser-induced fluorescence (LIF), dispersed fluorescence, and laser induced photo-chemistry. Various experiments were designed or modified including the following: flow cells, static cells, vacuum chambers, and ion collection systems. Programs were written to control all of these experiments and to produce the data reported.

Previous research suggests that diode pumped alkali lasers (DPAL) are a potential route for high-powered laser design for use in ballistics defense and communication due to their potentially favorable power scaling and useful wavelengths. Various complications of these lasers are described, as well as attempts to quantify various deleterious processes.

Laser induced fluorescence spectra for jet-cooled CaO have been used to examine the higher vibrational levels of the $A'^1\Pi(X\sigma\pi^{-1})$ state (v = 10 - 17) and the v = 6-8 vibrational levels of the $C^1\Sigma^+(B\sigma\sigma^{-1})$ state. A perturbation of v = 17 of the A' state was evident, caused by a spin-orbit mediated interaction with the $b^3\Sigma^+(\Omega = 1)(X\sigma\sigma^{-1})$ v = 14 level. Ro-vibrational constants for the A' state were obtained by fitting to the data for nominally unperturbed levels. The average radiative lifetime for the $A'^1\Pi(X\sigma\pi^{-1})$ state $v = 10 - 17$ levels was 10.6µs with no measurable dependence on v. This was consistent with the theoretical prediction of a relatively small transition dipole moment for the $A'^1\Pi - X^1\Sigma^+$ band system. A homogeneous perturbation of the $C^1\Sigma^+(B\sigma\sigma^{-1})$ v = 7 level was examined by means of dispersed laser induced fluorescence (DLIF) and radiative lifetime measurements. The DLIF spectra clearly demonstrate that the perturbing $\Omega = 0^+$ state is a component of a triplet state. Intense transitions from this state to the $a^3\Pi(0^+)(X\sigma\pi^{-1})$ state were observed. Configurational assignments are presented that support assignment of the perturbing state as the v = 12 vibrational level of the previously unobserved $g^3\pi(0^+)(B\sigma\pi^{-1})$ state.

Excited State: CaO, Cs, Rb

By

Sean M. Bresler
B.S., Chemistry, Miami University, 2012
B.A., Mathematics, Miami University, 2012

Advisor: Michael C. Heaven, Ph.D.

A dissertation submitted to the Faculty of the
James T. Laney School of Graduate Studies of Emory University
in partial fulfillment of the requirements for the degree of
Doctor of Philosophy
in Chemistry
2021

Acknowledgements

Time ordered (oldest to newest)

(Name, Most current higher-educational affiliation)

Jane Conley And James A. Bresler - UArizona, tOSU

Scott C. Bresler and Kelly J. (Bresler) Tanner - UofM, tOSU

Michael Chambers - Georgetown/NIH

Brian B. Laird - KU

Laurie J. Butler - UofC

Robert W. Field - MIT

Heather Allen - tOSU

Micheal C. Heaven - Emory

Heaven Group-at-Large - Emory, Including :

Jacob Stewart - Connecticut College

Joshua Bartlett

Kyle Mascaritolo

Michael Sullivan

Jiande Han

Amanda (Reed) Dermer - Knox College

Mallory (Theis) Green - Max Plank Institute

Daniel Frohman

Pearl Jean

Joel Schmitz

Thomas Persinger

Noah Jaffe

Arianna Rodriguez

R. Brian Dyer - Emory

Francesco Evangelista - Emory

Nicholas Stair - Lives in a Van (voluntary)

Sebastian (my cat)

PRMTG and Mana Burn members

Marin M. Kress - UMass-Boston

Contents

List of Figures

List of Tables

List of Algorithms

Chapter 1

Product channels of Rb removal

1.1 Abstract

Branching fractions for product channels of the reactions of Rb(6^2P) with H_2, CH_4 and C_2H_6 involving energy transfer and chemical transformation have been measured using time-resolved pulsed laser techniques. Removal of Rb(6^2P) atoms was monitored using laser induced fluorescence (LIF) measurements. The RbH product was detected using LIF of the A-X transition in the $500 - 530$ nm spectral range. Pump-probe measurements indicated a collisional loss of rubidium atoms due to the reactions of Rb(6^2P) with H_2 and C_2H_6 with branching fractions $\gamma^{ch}_{\mathrm{H}_2} = 0.217 \pm 0.03$ and $\gamma^{ch}_{\mathrm{C}_2\mathrm{H}_6} = 0.107 \pm 0.03$, respectively. The measurements for Rb(6^2P) + C_2H_6 did not provide conclusive evidence for a reactive loss channel. We detected RbH (v = 0, 1, and 2) produced from Rb(6^2P) in the presence of H_2. Surprisingly, the RbH product was not detected with CH_4 or C_2H_6, despite the fact that high-level ab initio calculations show the existence of favorable pathways for RbH formation.

The branching fractions for the energy transfer product channels were found to be $\gamma^{rel}_{H_2} = 0.79 \pm 0.05$, $\gamma^{rel}_{C_2H_6} = 0.92 \pm 0.05$ and $\gamma^{rel}_{CH_4} = 0.98 \pm 0.05$ for H_2,C_2H_6 and CH_4, respectively. The undetectable loss of Rb via the reaction with methane suggests that C_2H_6 may be the more stable diluting agent for use in the diode pumped Rb vapor laser system.

1.2 Introduction

Reactions of excited alkali metal atoms with hydrogen and hydrocarbon molecules are of interest because they can be used as models for testing the validity of theoretical electronic-to-vibration (E − V) energy transfer and chemical processes involving electronic excitation [1–4]. In addition, these reactions play important roles in the active media of diode-pumped alkali lasers (DPAL) [5–8] and laser-chemistry techniques for the separation of alkali-metal isotopes [9, 10].

Siara and Krause [11] have studied the excitation transfer between the 6^2P fine-structure sub-states in rubidium, as well as effective quenching cross sections of these states due to collisions with H_2, HD, D_2, N_2, CH_4, and CD_4 using sensitized fluorescence techniques. In recent studies [7], experimental and theoretical techniques were employed to characterize the removal of Rb(6^2P) by hydrogen, methane and ethane. Fan et al. [2] determined the nascent quantum state distributions of the RbH product resulting from the reactions of Rb($5^2D_{3/2,\,5/2}$, $7^2S_{1/2}$) with H_2 using a laser pump-probe technique. It was found that the nascent RbH product molecules were distributed among the three lowest vibrational (v = 0, 1, and 2) levels of the ground electronic state. Chen et al. [12] have investigated the E–V energy transfer between electronically excited rubidium atoms Rb($5^2P_{1/2,\,3/2}$) and hydrogen molecules using the coherent anti-Stokes Raman spectroscopy (CARS) technique. They found that during E − V energy transfer processes H_2 molecules are excited to the v = 1 and v = 2 vibrational levels with relative populations of 37% and 63%, respectively.

Renewed interest in the reactions involving excited alkali metal atoms is due to the fact that the saturated hydrocarbons methane and ethane are often used as collisional energy transfer agents in DPAL systems. These lasers use optical pumping of the D_2 line ($n^2P_{3/2} \rightarrow n^2S_{1/2}$) and lasing on the D_1 line (where n = 3, 4, 5, and 6 for Na, K, Rb and Cs, respectively) [13–15]. Collisional energy transfer is used to move the population from $n^2P_{3/2}$ to the $n^2P_{1/2}$ state. The collision partner used for this step must have a negligible rate constant for $\mathrm{n}p \leftarrow \mathrm{n}s$ quenching and be chemically inert with respect to the alkali vapor. Saturated hydrocarbons CH_4 and C_2H_6 have proven to be effective energy transfer agents [5, 6, 15]. The reactions of these species with alkali atoms that have been excited to the n*p* states are markedly endothermic. Despite this circumstance, the optically pumped alkali vapor does react with saturated hydrocarbons over an extended period of laser operation [13, 16, 17]. This process produces both metal containing products and carbon particles. The reactions degrade DPAL performance through the loss of the alkali metal, the production of light scattering particles in the laser medium, and photochemically induced cell window damage. A possible pathway for the reaction that overcomes the high barrier involves the production of higher excited atomic states via energy pooling processes. For example, in the case of Rb the energy pooling is of the form [18]

$$\mathrm{Rb}(5^2\mathrm{P}) + \mathrm{Rb}(5^2\mathrm{P}) \rightarrow \mathrm{Rb}^* + \mathrm{Rb}(5^2\mathrm{S}) \tag{1.1}$$

where '$*$' indicates 7^2S or 5^2D (we have also observed emission from Rb(6^2P) following pulsed excitation of the D1 or D_2 lines). It has been established that the higher excited states become populated during DPAL operation. As described below, Rb(6^2P) and higher energy states have enough energy to abstract H atoms from H_2,CH_4 and C_2H_6, but the corresponding reactions for Rb(6^2S or 4^2D) are endothermic.

In the present study we examine the reactive removal of Rb(6^2P) by H_2, CH_4 or C_2H_6. The 6^2P state was chosen as it is the first level with sufficient energy for exothermic extraction and insertion reactions. Use of this level avoids the complication of energy transfer between levels that are above the barrier to reaction. The 6^2P kinetics are relevant to the other states populated by pooling because, as presented in the theoretical section of this paper, transfer to the ground state potential energy surface will occur prior to reaction. The measurements were carried out by means of pulsed laser pump-probe methods. The energy levels of importance for these experiments are shown in Fig. 1.1. A pulsed laser was used to excite Rb to the $6^2P_{3/2}$ level. Under low pressure conditions, radiative relaxation of the form

$$\mathrm{Rb}(6^2\mathrm{P}) \rightarrow \mathrm{Rb}(6^2\mathrm{S}) + \mathrm{h}\nu_1 \rightarrow \mathrm{Rb}(5^2\mathrm{P}) + \mathrm{h}\nu_2 \tag{1.2}$$

$$\mathrm{Rb}(6^2\mathrm{P}) \rightarrow \mathrm{Rb}(4^2\mathrm{D}) + \mathrm{h}\nu_3 \rightarrow \mathrm{Rb}(5^2\mathrm{P}) + \mathrm{h}\nu_4 \tag{1.3}$$

contributes significantly to the total removal of Rb(6^2P). The removal of Rb(6^2P) via collisional transfer or chemical processes may also contribute to the removal kinetics via the elementary reactions

$$\begin{aligned} \mathrm{Rb}(6^2\mathrm{P}) + \mathrm{H}_2 &\rightarrow \mathrm{Rb}(6^2\mathrm{S}\ \text{or}\ 4^2\mathrm{D}) + \mathrm{H}_2 \\ &\rightarrow \mathrm{RbH} + \mathrm{H} \end{aligned} \tag{1.4}$$

$$\begin{aligned} \mathrm{Rb}(6^2\mathrm{P}) + \mathrm{CH}_4 &\rightarrow \mathrm{Rb}(6^2\mathrm{S}\ \text{or}\ 4^2\mathrm{D}) + \mathrm{CH}_4 \\ &\rightarrow \text{reactive products} \end{aligned} \tag{1.5}$$

$$\begin{aligned}\mathrm{Rb}(6^2\mathrm{P}) + \mathrm{C_2H_6} &\rightarrow \mathrm{Rb}(6^2\mathrm{S} \text{ or } 4^2\mathrm{D}) + \mathrm{CH_4} \\ &\rightarrow \text{reactive products}\end{aligned} \tag{1.6}$$

The only reactive product channel for Reaction 1.4 is RbH + H. Fan et al. [2] detected the presence of RbH from the reaction of $\mathrm{Rb}(5^2\mathrm{D}_{3/2,\,5/2}, 7^2\mathrm{S}_{1/2})$ with H_2 but the branching fractions for the reactive and collisional product channels of Reaction 1.4 have not been determined. No information is available about product channels of Reactions 1.5 and 1.6. To detect the reactive channels, a delayed probe laser pulse was used in the present study to observe the ground state recovery following excitation to $\mathrm{Rb}(6^2\mathrm{P})$. Incomplete population recovery was used as evidence of reactive loss.

1.3 Experimental

A schematic view of the apparatus used for the present measurements is shown in Fig. 1.2. The fluorescence cell and experimental technique have been described in detail in a recent publication [7]. Briefly, the fluorescence cell was constructed from a six-way cross for the flow of gases, the passage of the excitation and probe laser beams, and observation of laser induced fluorescence (LIF).

The Rb $6^2\mathrm{P}_{3/2} \leftarrow 5^2\mathrm{S}_{1/2}$ transition was excited by 10 ns light pulses (λ = 420.29 nm) generated by an excimer pumped dye laser (Lambda Physik, Compex Pro 201/FL3002 combination). Another similar laser combination was used to probe the Rb number density via LIF of the same atomic transition. The delay between the laser pulses was controlled by a digital pulse delay generator (Quantum Composers model 9614).

To reduce window scattering problems for the laser beams, two baffle arms were attached to the photolysis cell. UV grade fused silica windows were attached to the

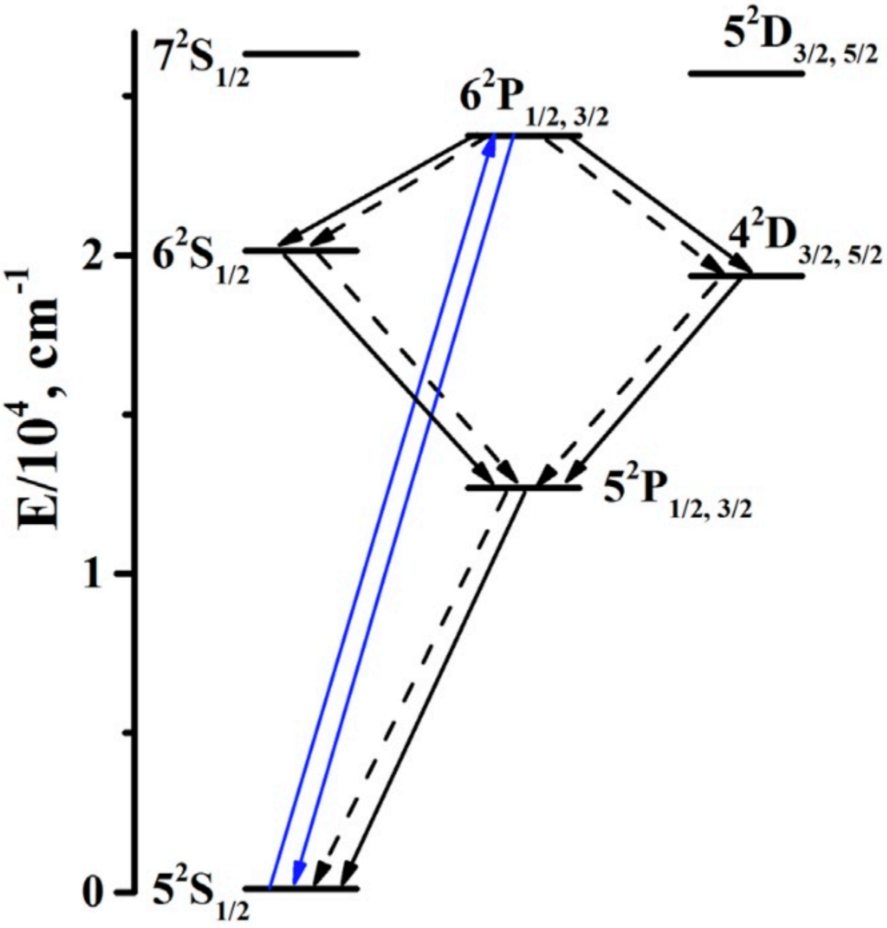

Figure 1.1: An energy level diagram for Rb. The transitions of importance are excitation (upward solid arrows), radiative relaxation (downward solid arrows), and collision induced energy transfer (dashed arrows)

ends of these arms. Fluorescence from the center of the cell was collected by a 5 cm focal length lens, and focused on the entrance slit of a 1/8 m monochromator (Oriel Corp. Model 1402). The dispersed fluorescence was then detected by an RCA 1P28 photomultiplier tube (PMT). The PMT output was signal-averaged using a digital oscilloscope (Le Croy Scope Station 140). The time resolution of the detection system was about 10 ns.

Rubidium vapor was entrained by flowing the H_2, CH_4 or C_2H_6 carrier gas over a heated sample holder that contained approximately 0.1 g of Rb at the start of each series of measurements. The temperature of the sample holder was measured using a K-type thermocouple. Needle valves were used to control the gas flow rates. The sample gases H_2 (99.99% purity), CH_4 (99.99%), C_2H_6 (99.99%) and the Rb metal (99.99%, Aldrich) were used without further purification. The fluorescence cell was evacuated by a rotary pump (Welch Duo-seal Model 1402), and the pumping rate was adjusted using a ball valve. Pressure in the fluorescence cell was measured using a capacitance manometer (MKS Baratron model 122A, 0–10 Torr).

1.4 Results and discussion

The $6^2P_{3/2} \leftarrow 5^2S_{1/2}$ transition was chosen to produce electronically excited Rb atoms. For the conditions of these measurements, collisions with H_2, CH_4 or C_2H_6 resulted in rapid energy transfer between the $6^2P_{3/2}$ and $6^2P_{1/2}$ fine-structure components [11]. To simplify the kinetic analysis, the experiments were conducted using low Rb number densities in order to avoid radiation trapping [5]. However, this approach limited the fluorescence intensity and thereby the spectral resolution that could be achieved. The small monochromator used for these measurements could not resolve the fine structure of the $6^2P \rightarrow 5^2S$ transition at the slit width required for workable signal-to-noise ratios. Fortunately, an equilibrium population distribution between

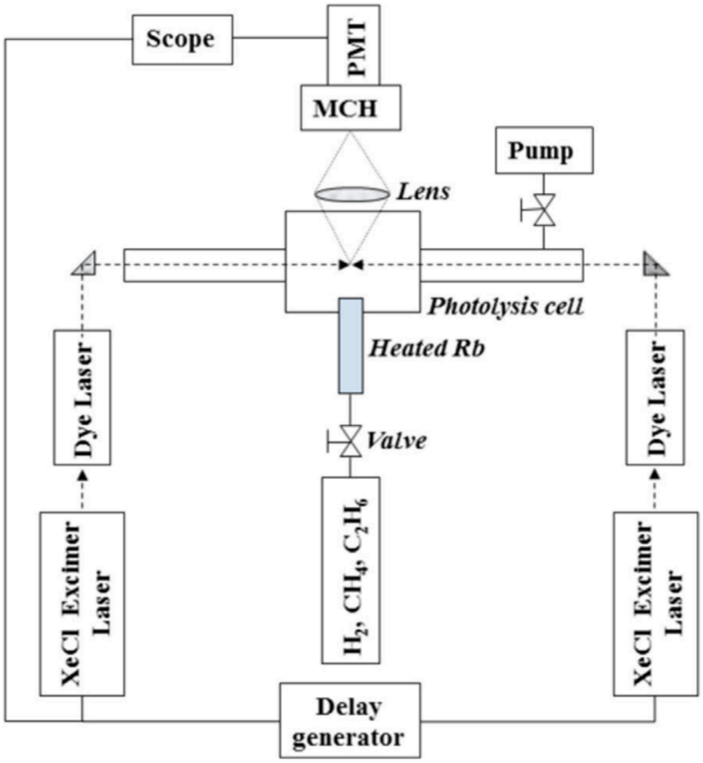

Figure 1.2: Apparatus used to study the removal rate of Rb(6^2P) by H_2, CH_4, and C_2H_6. MCH - monochromator (Oriel Corp. Model 1402), PMT - photomultiplier tube (RCA 1P28).

the $6^2P_{3/2}$ and $6^2P_{1/2}$ levels was achieved on a time scale that was short compared to all other kinetic processes. This was expected based on the large energy transfer rate constants reported by Siara and Krause [11] and supported by the observation of the same kinetic behavior (in the current experiments) regardless of whether the initially excited level was $6^2P_{3/2}$ or $6^2P_{1/2}$.

The interaction of Rb(6^2P) with hydrocarbons proceeds via two mechanisms, collisional relaxation (processes 4a, 5a and 6a) and chemical loss (processes 4b, 5b and 6b). As shown in Figure 1.1, the energy transfer processes result in population of the 5^2P state through the processes

$$\mathrm{Rb}(6^2\mathrm{P}) + \mathrm{M} \rightarrow \mathrm{Rb}(6^2\mathrm{S}\ \text{or}\ 4^2\mathrm{D}) + \mathrm{M} \rightarrow \mathrm{Rb}(5^2\mathrm{P}) + \mathrm{M}. \tag{1.7}$$

Here M is H_2, CH_4 or C_2H_6. The observed time-resolved fluorescence signals from the Rb $5^2\mathrm{P} \rightarrow 5^2\mathrm{S}$ transition are depicted in Figure 1.3 for two H_2 pressures. As can be seen from this figure, the rate of Rb(5^2P) formation increases with the H_2 pressure.

The differential rate equations for the populations of Rb atoms in the 6^2P and 5^2P states can be written as follows:

$$\frac{d\mathrm{N}_{6\mathrm{P}}}{dt} = -(\mathrm{A}_{rad} + \mathrm{k}_{\mathrm{M}}\mathrm{N}_{\mathrm{M}})\mathrm{N}_{6\mathrm{P}} \tag{1.8}$$

$$\frac{d\mathrm{N}_{5\mathrm{P}}}{dt} = (\mathrm{A}_{6\mathrm{P}-6\mathrm{S}\,4\mathrm{D}} + \mathrm{N}_{6\mathrm{P}} - (\mathrm{A}_{5\mathrm{P}-5\mathrm{S}} + \mathrm{k}_{\mathrm{M}}^{5\mathrm{P}}\mathrm{N}_{\mathrm{M}})\mathrm{N}_{5\mathrm{P}} \tag{1.9}$$

where $\mathrm{A}_{rad} = \mathrm{A}_{6\mathrm{P}-5\mathrm{S}} + \mathrm{A}_{6\mathrm{P}-6\mathrm{S},\,4\mathrm{D}}$, $\mathrm{A}_{6\mathrm{P}-5\mathrm{S}}$ is the Einstein coefficient for the $6^2\mathrm{P} \rightarrow 5^2\mathrm{S}$ transition, $\mathrm{A}_{6\mathrm{P}-6\mathrm{S},\,4\mathrm{D}}$ is the total Einstein coefficient for $6^2\mathrm{P} \rightarrow 6^2\mathrm{S}$, 4^2D transitions, $\mathrm{A}_{5\mathrm{P}-5\mathrm{S}}$ is the Einstein coefficient for the $5^2\mathrm{P} \rightarrow 5^2\mathrm{S}$ transition, $\mathrm{k}_{\mathrm{M}} = \mathrm{k}_{\mathrm{M}}^{rel} + \mathrm{k}_{\mathrm{M}}^{ch}$ is the total rate constant for the removal of Rb(62P) by M = H_2, CH_4 or C_2H_6, $\mathrm{k}_{\mathrm{M}}^{ch}$ is the rate constant for the chemical processes 4b, 5b and 6b, $\mathrm{k}_{\mathrm{M}}^{rel}$ is the rate constant for the processes 4a, 5a and 6a, N_{M} is the number density of the M-th species, N_{6P} and N_{5P} are the number densities of Rb(6^2P) and Rb(5^2P), respectively, k_M^{5P} is the rate constant for the collisional energy transfer process Rb(5^2P) + M → Rb(5^2S) + M. As the radiative transfer from 6^2S, 4^2D → 5^2P is much faster than the 6^2P → 6^2S, 4^2D processes, the rate of transfer to 5^2P is limited by the 6^2P → 6^2S, 4^2D processes. The validity of the approximation implicit in Equation (1.9) was confirmed by numerical simulations performed using the Einstein coefficients from reference [19]. The solution of Equation (1.8) is given by

$$N_{6P} = (N_{6P})_0 \exp[-(A_{rad} + k_M N_M)t] \tag{1.10}$$

where $(N_{6P})_0$ is the Rb(6^2P) number density at $t = 0$. Substituting Equation (1.10) in Equation (1.9) and taking into account that $k_{N_M}^{5P} \ll A_{5P-5S}$ [20], Equation (1.9) can be rewritten as follows:

$$\begin{aligned} \frac{dN_{5P}}{dt} =& (N_{6P})_0 (A_{6P-6S,\,4D} + k_M^{rel} N_M) \exp[-(A_{rad} + k_M N_M)t] \\ & - A_{5P-5S} N_{5P} \end{aligned} \tag{1.11}$$

From (10) we obtained the following temporal dependence for the population of rubidium atoms in the 5^2P state:

$$\begin{aligned} N_{5P}(t) = & -\frac{(N_{6P})_0 (A_{6P-6S,\,4D} + k_M^{rel} N_M)}{(A_{rad} + k_M N_M) + A_{5P-5S}} \\ & \times [\exp(-A_{5P-5S}t - \exp[-(A_{rad} + k_M N_M)t)]] \end{aligned} \tag{1.12}$$

Upon integrating (11) with respect to the time we obtain the expression for an area S under the curve $N_{5P}(t)$ as follows:

$$\mathrm{S} = \int_0^\infty \mathrm{N}_{5\mathrm{P}}(\mathrm{t})\,d\mathrm{t} = \frac{(\mathrm{N}_{6\mathrm{P}})_0(\mathrm{A}_{6\mathrm{P}-6\mathrm{S},\,4\mathrm{D}} + \gamma_{\mathrm{M}}^{rel}\mathrm{k}_{\mathrm{M}}\mathrm{N}_{\mathrm{M}})}{(\mathrm{A}_{rad} + \mathrm{k}_{\mathrm{M}}\mathrm{N}_{\mathrm{M}})\mathrm{A}_{5\mathrm{P}-5\mathrm{S}}} \tag{1.13}$$

where $\gamma_{\mathrm{M}}^{rel} = \mathrm{k}_{\mathrm{M}}^{rel}/\mathrm{k}_{\mathrm{M}}$.

Areas under curves (in arbitrary units) for the LIF signals for the $\mathrm{Rb}(5^2\mathrm{P} \rightarrow 5^2\mathrm{S})$ transition as functions of the number densities of H_2, C_2H_6 or CH_4 are depicted in Figures 1.4 to 1.6, respectively. For comparison, the calculated dependencies of $\mathrm{S}(\mathrm{N}_{\mathrm{H}_2})$ are presented in Fig. 1.4 for $\gamma_{\mathrm{H}_2}^{rel} = 1$ (dashed curve) and $\gamma_{\mathrm{H}_2}^{rel} = 0$ (dash-dot curve) for $\mathrm{A}_{rad} = 8.77 \times 10^6\ \mathrm{s}^{-1}$ [21], $\mathrm{A}_{5\mathrm{P}-5\mathrm{S}} = 37 \times 10^6\ \mathrm{s}^{-1}$ [22],$\mathrm{A}_{6\mathrm{P}-6\mathrm{S},\,4\mathrm{D}} = 6.4 \times 10^6\ \mathrm{s}^{-1}$ [19], and $\mathrm{k}_{\mathrm{H}_2} = 7 \times 10\ \mathrm{cm}^3\ \mathrm{s}^{-1}$ [7]. It is evident that Equation (1.13) is an appropriate choice for definition of the parameter $\gamma_{\mathrm{M}}^{rel}$, which is obtained by fitting to the experimental data presented in Figures 1.4 to 1.6.

Equation (1.13) was fit to the experimental data using $\mathrm{k}_{\mathrm{H}_2} = (7.0 \pm 0.2) \times 10^{10}\,\mathrm{cm}^3\mathrm{s}^{-1}$,$\mathrm{k}_{\mathrm{C}_2\mathrm{H}_6} = 8.1 \times 10^{10}\,\mathrm{cm}^3\mathrm{s}^{-1}$ and $\mathrm{k}_{\mathrm{CH}_4} = 6.2 \times 10^{10}\,\mathrm{cm}^3\mathrm{s}^{-1}$ [7]. The Origin software options "Fitting Function Builder" and "Nonlinear Curve Fit" were used for fitting the value of $\gamma_{\mathrm{M}}^{rel}$. The smooth curves in Figures 1.4 to 1.6 are the best-fit results with $\gamma_{\mathrm{H}_2}^{rel} = 0.79 \pm 0.05$, and $\gamma_{\mathrm{C}_2\mathrm{H}_6}^{rel} = 0.92 \pm 0.05$, and $\gamma_{\mathrm{CH}_4}^{rel} = 0.98 \pm 0.05$, respectively.

The branching fraction for the chemical loss channel was examined using a laser pump-probe technique. First, we recorded the LIF signal (I_0) from the $\mathrm{Rb}(6^2\mathrm{P}-5^2\mathrm{S})$ transition caused by the probe pulse alone. Then, we recorded the same signal (I) but after a pump pulse. The laser intensity of the pump was sufficient for saturation of the transition. The delay between the pump and probe pulses ($\sim 1\ \mu$s) was long enough to make sure that the Rb (6^2P) atoms were deactivated, while being short with respect to the diffusion of Rb atoms out of the probe laser excitation volume. The dependencies of the signal ratios I/I_0 on the H_2, C_2H_6, and CH_4 number densities are shown in Figures 1.7 to 1.9, respectively. A decrease in the signal ratio with increasing H_2 (Fig. 1.7) and C_2H_6 (Fig. 1.8) number densities indicated that some fraction of the Rb (6^2P) atoms was lost via chemical reactions.

A simplified kinetic model was used to extract the branching fraction for the chemical loss channel from the experimental data presented in Figures 1.7 to 1.9. The differential rate equation for the population of Rb atoms in the excited 62P state can be described by Equation (1.10). The pump laser in these experiments was used to saturate the $6^2\mathrm{P}_{3/2} \rightarrow 5^2\mathrm{S}_{1/2}$ transition. Hence the concentration of Rb(6P) immediately after the pump pulse (t = 0) was $(\mathrm{N}^6\mathrm{P})_0 = 2\mathrm{N}_{\mathrm{Rb}}/3$, where N_{Rb} was the total Rb number density prior to the pump pulse. Following laser excitation, the 6^2P population decays by reactive and physical channels. The rate at which the products of the chemical reactions are formed is given by

$$\frac{d\mathrm{N}_{Prod}}{d\mathrm{t}} = \mathrm{k}_{\mathrm{M}}^{ch}\mathrm{N}_{\mathrm{M}}\mathrm{N}_{6\mathrm{P}} = \frac{2\mathrm{N}_{\mathrm{Rb}}}{3}\mathrm{k}_{\mathrm{M}}^{ch}\mathrm{N}_{\mathrm{M}}\exp(-(\mathrm{A}_{rad} + \mathrm{k}_{\mathrm{M}}\mathrm{N}_{\mathrm{M}})\mathrm{t}) \tag{1.14}$$

integration of this expression out to t = ∞ yields the result

$$\mathrm{N}_{Prod} = \frac{2\mathrm{N}_{\mathrm{Rb}}}{3}\frac{\mathrm{k}_{\mathrm{M}}^{ch}\mathrm{N}_{\mathrm{M}}}{\mathrm{A}_{rad} + \mathrm{k}_{\mathrm{M}}\mathrm{N}_{\mathrm{M}}} \tag{1.15}$$

At this limit the remaining concentration of Rb is

$$\mathrm{N}_{Rb} - \mathrm{N}_{Prod} = \mathrm{N}_{\mathrm{Rb}}\left(1 = \frac{2}{3}\frac{\mathrm{k}^{ch}\mathrm{N}_{\mathrm{M}}}{\mathrm{A}_{rad} + \mathrm{k}_{\mathrm{M}}\mathrm{N}_{\mathrm{M}}}\right) \tag{1.16}$$

As the LIF intensities are directly proportional to the Rb(5^2S) concentration: $\mathrm{I} \sim \mathrm{N}_{\mathrm{Rb}} - \mathrm{N}_{Prod}$ and $\mathrm{I}_0 \sim \mathrm{N}_{\mathrm{Rb}}$, Equation (1.16) can be rewritten as

$$\frac{\mathrm{I}}{\mathrm{I}_0} = \left(1 - \frac{2}{3}\frac{\mathrm{k}_{\mathrm{M}}^{ch}\mathrm{N}_{\mathrm{M}}}{\mathrm{A}_{rad} + \mathrm{k}_{\mathrm{M}}\mathrm{N}_{\mathrm{M}}}\right) \tag{1.17}$$

Expression (16) was fitted to the experimental data presented in Figures 1.7 to 1.9, using $\mathrm{k}_{\mathrm{H}_2} = 7.0\times10^{10}\mathrm{cm}^3\mathrm{s}^{-1}$, $\mathrm{k}_{\mathrm{C}_2\mathrm{H}_6} = 8.1\times10^{10}\mathrm{cm}^3\mathrm{s}^{-1}$ and $\mathrm{k}_{\mathrm{CH4}} = 6.2\times10^{10}\mathrm{cm}^3\mathrm{s}^{-1}$

[7]. The Origin software options “Fitting Function Builder”and “Nonlinear Curve Fit” were used to fit the value of γ_{M}^{ch} to the experimental data for I/I_0. The smooth curves in Figures 1.7 to 1.9 are the best-fit results for $\gamma_{\mathrm{H_2}}^{ch} = 0.21 \pm 0.03$, $\gamma_{\mathrm{C_2H_6}}^{ch} = 0.10 \pm 0.03$, and $\gamma_{\mathrm{CH_4}}^{ch} = 0.04 \pm 0.03$, respectively.

For collisions between high-lying electronically excited Rb atoms and H_2 molecules, Fan et al. [2] observed the reactive process

$$\mathrm{Rb}(5^2\mathrm{D},\ 7^2\mathrm{S}) + \mathrm{H_2} \rightarrow \mathrm{RbH}\,(\mathrm{v} = 0,\ 1,\ \text{and}\ 2) + \mathrm{H} \tag{1.18}$$

using a laser pump-probe technique. RbH was detected using LIF of the $\mathrm{A} - \mathrm{X}$ transition in the $500 - 530$ nm spectral range. Using the same approach, we also detected $\mathrm{RbH}(\mathrm{v} = 0, 1 \text{ and } 2)$ produced from $\mathrm{Rb}(6^2\mathrm{P})$ in the presence of H_2, but not in the presence of CH_4 or C_2H_6. Note that there is only one possible chemical channel for reaction 4. Reactions 5 and 6 may form several products. Failure in the detection of an LIF signal from the $\mathrm{A} - \mathrm{X}$ transition could be attributed to rapid quenching of RbH(A) by methane and ethane. To test this hypothesis, we added either methane or ethane to the $\mathrm{Rb}/\mathrm{H_2}$ mixture. If CH_4 or C_2H_6 deactivate RbH(A), their presence should have caused a decrease in the LIF signal. However, adding CH_4 and C_2H_6 to the $\mathrm{Rb}/\mathrm{H_2}$ mixture up to 5×10^{16} cm^3 number densities caused no noticeable effect on the magnitude of the LIF signal. Our experimental data provided an upper bound for the branching fraction $< 0.02\, \gamma_{\mathrm{M}}^{ch}$ for the RbH product channel for the reactions 5 and 6.

We applied *ab initio* electronic structure calculations to investigate the possible products of the $\mathrm{Rb} + \mathrm{H_2}$, $\mathrm{Rb} + \mathrm{CH_4}$, and $\mathrm{Rb} + \mathrm{C_2H_6}$ reactions, and to find reaction paths that are energetically feasible for reactions 5 and 6. Geometries of intermediates, transition states, and possible products were optimized using the B3LYP variant of hybrid density functional theory (DFT) [23, 24] with the Def2-TZVP basis set and the MW46 pseudo potential for the Rb atom [25]. Vibrational frequencies were computed at the same level of theory and were used to obtain zero-point vibrational energy corrections (ZPE). Relative energies of various species were refined by means of single-point calculations using the coupled cluster method CCSD(T) [26–29] with the Def2-QZVPPD basis set [25] at the optimal geometries obtained from the DFT B3LYP method. All DFT B3LYP and CCSD(T) quantum chemical calculations were performed using the GAUSSIAN 09 [30] and MOLPRO 2010 [31] program packages, respectively.

If there is no orbital degeneracy in the ground electronic state of either reactant(s) or product(s), the potential energy surface (PES) of electronically excited reactant(s) adiabatically correlates with the PES of electronically excited products. For the reactions of the electronically excited rubidium atom Rb(6^2P) with M (H_2, CH_4, and/or C_2H_6), the path to electronically excited products is energetically unattainable. Reactive pathways require a non-adiabatic transfer from an excited PES to the ground surface as a result of internal conversion. In this view, possible products of the Rb(6^2P) + M reaction are to be found on the ground state PES, which relates to the Rb(5^2S) + M reaction.

The computed potential energy diagrams for the Rb(5^2S) + M reactions are illustrated in Fig. 1.10. There are two possible reactive pathways for the Rb + H_2 reaction, either through an insertion of Rb into the H − H bond or through a barrierless H abstraction that is endothermic by 65.2 kcal/mol. The first pathway occurs via a distinct transition state (63.5 kcal/mol above the reactants) and leads first to a HRbH intermediate. The intermediate can then dissociate to RbH+H without an exit barrier via a loose transition state in a slightly endothermic process (1.6 kcal/mol). The excitation energy of Rb(6^2P) (68.03 kcal/mol) exceeds the energy requirements for both reaction paths and the RbH product can be formed. The experimental data presented in this paper indicate that the collisional relaxation process (4a) is dominating. It was recently shown [7] that an avoided crossing between potentials that correlate with the 6^2S and 6^2P states is responsible for the fast removal of Rb(6^2P) in the process (4a). The chemical transformation pathway leading to RbH + H can be realized only when internal conversion steps continue all the way to the ground state PES.

Few possible reactive pathways exist for the Rb + CH_4 reaction. Insertion of Rb into a C – H bond occurs via a distinct transition state (63.6 kcal/mol) and leads to an intermediate $HRbCH_3$.This intermediate can dissociate by losing an H atom or the CH_3 group without exit barriers. The energy required for H elimination is 12.6 kcal/mol higher than that for CH_3 loss and therefore the latter process is should be preferable. Note that the $HRbCH_3$ intermediate is predicted to be bound only by 0.1 kcal/mol with respect to CH_3 loss, and therefore represents only a metastable species. The RbH + CH_3 products can be also formed by direct abstraction of H from CH_4 via a barrier of 65.6 kcal/mol. No paths to the $RbCH_2 + H_2$ products (endothermic by 69.6 kcal/mol) could be found.

We did not detect RbH molecules when Rb(6^2P) was generated in the presence of CH_4. The experimental data presented in Fig. 1.9 suggest that the chemical loss of Rb atoms is negligible. The estimated branching fraction for reaction 5b, $\gamma^{ch}_{CH_4} 0.04 \pm 0.03$, is close to zero within the experimental error. Electronic structure calculations of the long-range Rb + CH_4 interactions [7] suggest that physical Rb(6^2P) relaxation proceeds via an electronic to ro-vibrational (E−V, R) energy transfer process, i.e., the electronic excitation energy of Rb atoms is converted to the internal energy of CH_4. The chemical reaction to form RbH + CH_3 apparently does not occur either because the ground state PES is not accessed via internal conversion or it is accessed on the slope of a steep hill leading to the ground state Rb(5^2S) + CH_4 products. As can be seen from the potential energy diagram in Fig. 1.10, a stable $RbCH_3$ molecule could be formed in the process

$$\mathrm{Rb} + \mathrm{CH_4} \rightarrow \mathrm{RbCH_3} + \mathrm{H} \tag{1.19}$$

However, the gap between the reaction energy ($\Delta\mathrm{E} = 77.5$ kcal/mol) and the excitation energy of Rb(6^2P) is about 9.5 kcal/mol, which makes this pathway highly unlikely. This reaction path may noticeably contribute to the degradation of the DPAL active medium where electronic states of Rb higher then 6^2P are formed, as for example in processes involving multi-photon excitation and electron/ion recombination.

The analysis of the Rb + C_2H_6 system shows that the reaction paths leading to the formation of the RbH + C_2H_5 and $RbCH_3$ + CH_3 products are energetically feasible and deserve attention. The first product pair contains RbH but we have not detected this species in our pump-probe experiment. The reasons that RbH + C_2H_5 are minor products are be similar to those discussed above for the Rb + CH_4 reaction not producing observable yields of RbH + CH_3. However, the data presented in Fig. 1.8 are indicative of a reactive loss of Rb atoms. Products $RbCH_3$ and CH_3 could be formed via insertion of the Rb atom into the C – C bond. This pathway is energetically accessible and could be responsible for the loss of Rb atoms in the pump-probe experiments with C_2H_6.

1.5 Conclusions

Our measurements indicate that collisional removal of Rb(6^2P) by H_2, CH_4 and C_2H_6 predominantly occurs due to energy transfer processes with branching fractions $\gamma^{rel}_{H_2} = 0.79 \pm 0.05$, $\gamma^{rel}_{C_2H_6} = 0.92 \pm 0.05$, and $\gamma^{rel}_{CH_4} = 0.98 \pm 0.05$, respectively. About every fifth collision with H_2, and every tenth with C_2H_6 leads to a chemical reaction. Given that the total rate constant for the removal of Rb(6^2P) by C_2H_6 is close to the gas-kinetic limit [7], this indicates that energy pooling followed by the reaction could be a significant part of the observed performance degradation in static gas Rb/ethane DPAL systems. The measurements for $Rb(6^2P) + CH_4$ do not provide conclusive evidence for a reactive loss channel. The slight loss of Rb observed is at the margins of the experimental error. This result suggests that methane may be a somewhat more stable energy transfer agent for Rb DPAL systems. In this context it is noteworthy that Bogachev et al. [8] reported a cesium vapor laser with closed-cycle circulation of the laser-active medium. The power of the laser radiation amounted to ∼ 1 kW with a 'light-to-light' conversion efficiency of ∼ 48%. Methane was used as the energy transfer agent in this device. In future studies it will be of interest to measure the reactive branching ratio for $Rb(*) + M$ with greater accuracy and to explore the excited and ground potential energy surfaces and their conical intersections to determine the dynamically accessible reaction channels.

Laser induced chemical reactions of alkali metals with hydrogen molecules can be used for isotope separation with a 'photon-to-hydride' conversion efficiency of ∼ 20%. The laser pump-probe method used here represents a promising approach to measure branching fractions $\gamma_{H_2}^{ch}$ for reactions of a variety of isotopes in 2 distinct electronically excited states.

1.6 Acknowledgements

This work was supported at Emory University by the Joint Technology Office through the Air Force Office of Scientific Research (AFOSR) under contract FA9550-13-1-0002. Work at the Samara National Research University was supported by the Government of the Russian Federation (Grant No. 14.Y26.31.0020).

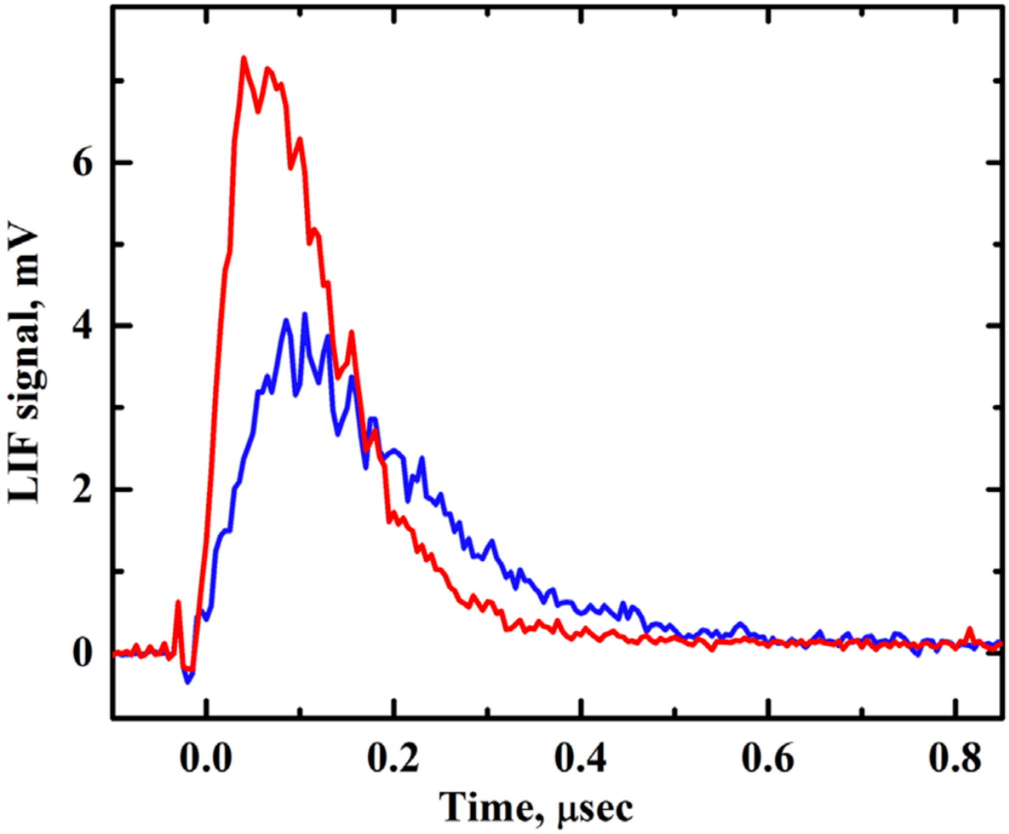

Figure 1.3: Typical LIF signals for the Rb(5^2P → 5^2S) transition for two H_2 pressures (0.08 Torr - blue, 0.756 Torr - red) at T = 120°C and a fixed Rb atom number density.

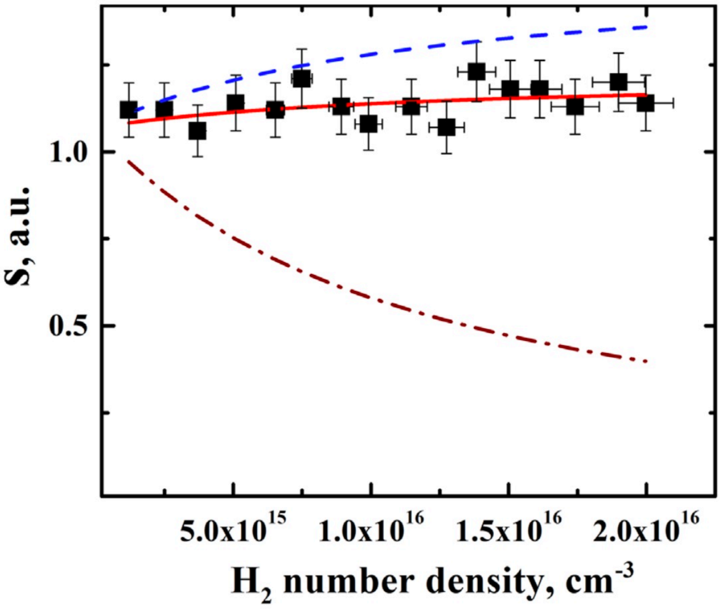

Figure 1.4: Areas under LIF curves (Equation (1.13)) versus H_2 number density. The symbols show experimental data. The solid red curve is the best fit of Equation (1.13) to the experimental data. The dashed and dash-dot curves are the predictions of Equation (1.13) for $\gamma_{H_2}^{rel} = 1$, $\gamma_{H_2}^{rel} = 0$ respectively.

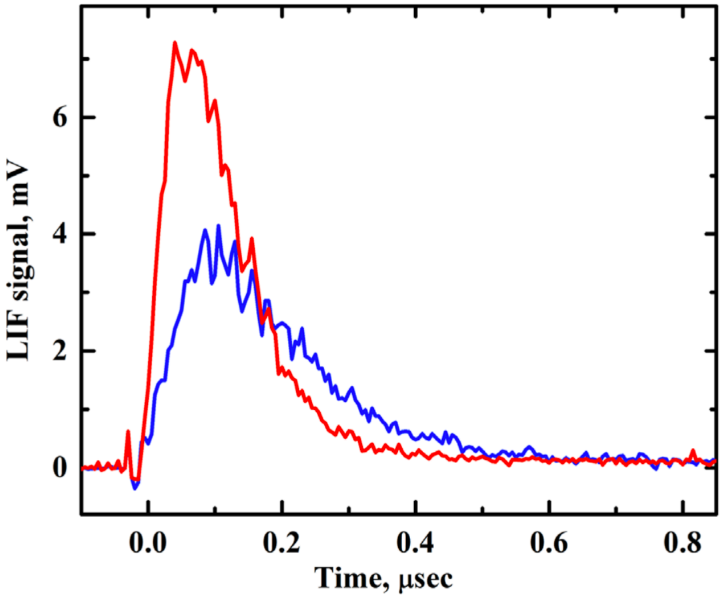

Figure 1.5: Areas under curves (Equation (1.13)) versus C_2H_6 number density. Symbols show experimental data. The solid red curve is the best fit of Equation (1.13) to the experimental data. (For interpretation of the references to color in this figure legend, the reader is referred to the web version of this article.)

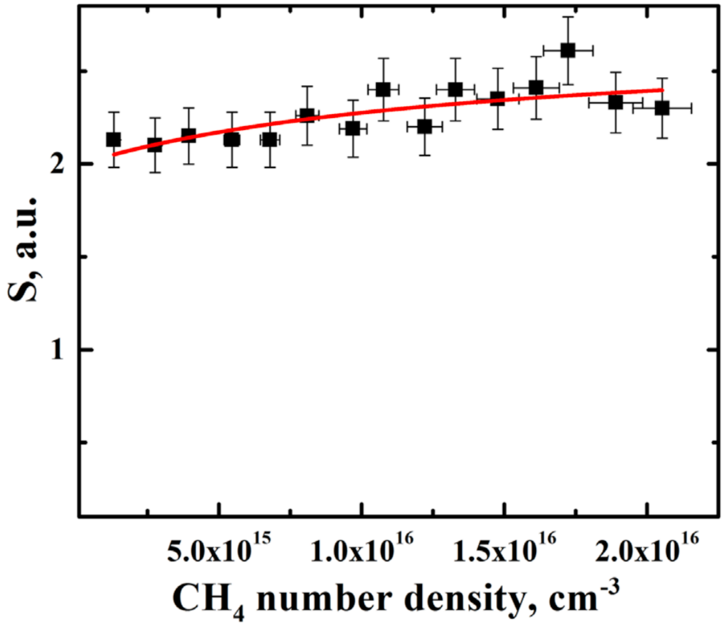

Figure 1.6: Areas under curves (Equation (1.13)) versus CH_4 number density. Symbols show experimental data. The solid red curve is the best fit of Equation (1.13) to the experimental data. (For interpretation of the references to color in this figure legend, the reader is referred to the web version of this article.)

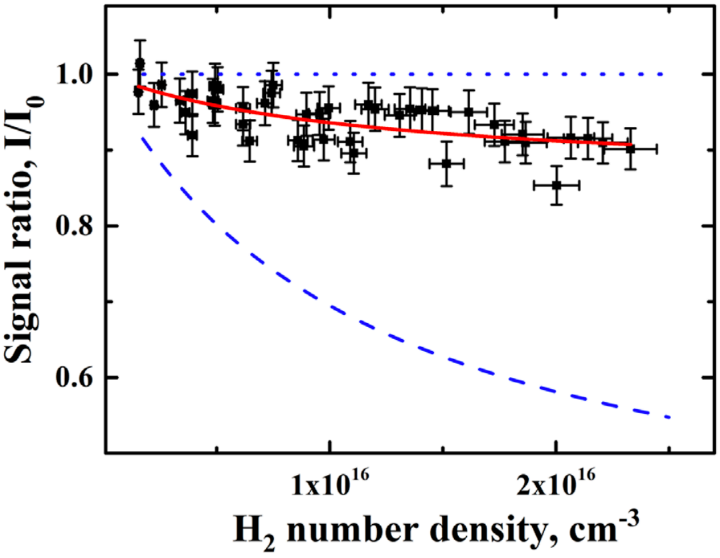

Figure 1.7: The signal ratio I/I_0 as a function of the H_2 number density. The curve is the best fit of Equation (1.17) to the experimental data (symbols). The dashed and dotted curves are the solutions of Equation (1.17) for $\gamma_{H_2}^{ch} = 1$ and $\gamma_{H_2}^{ch} = 0$
, respectively.

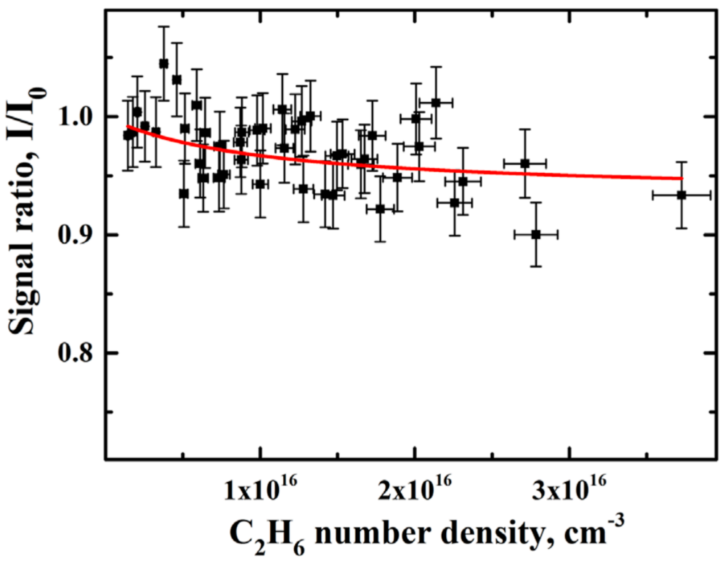

Figure 1.8: The signal ratio I/I$_0$ as a function of the C_2H_6 number density. The curve is the best fit of Equation (1.17) to the experimental data (symbols).

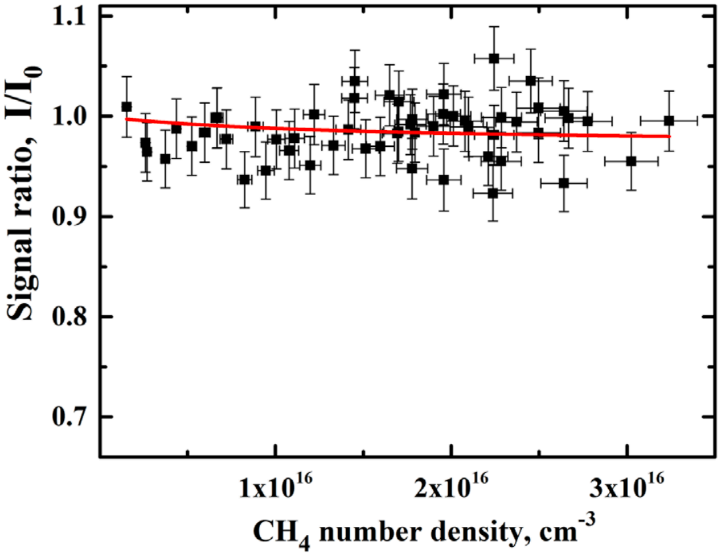

Figure 1.9: The signal ratio I/I$_0$ as a function of the CH_4 number density. The curve is the best fit of Equation (1.17) to the experimental data (symbols).

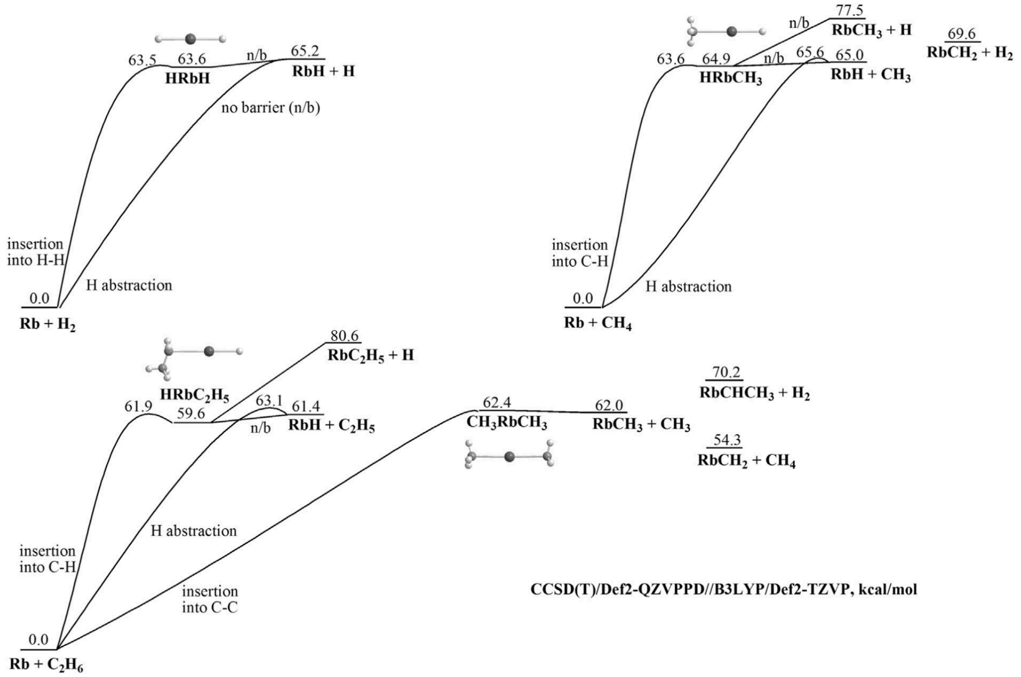

Figure 1.10: Potential energy diagrams of various channels for the reactions of atomic rubidium with H_2, CH_4, and C_2H_6 calculated at the CCSD(T)/Def2-QZVPPD//B3LYP/Def2-TZVP level of theory. The numbers show relative energies of products, transition and intermediate states in kcal/mol with respect to reactants.

Chapter 2

Rb Removal By hydrocarbons

2.1 Removal of Rubidium

2.1.1 Summary

The saturated hydrocarbons methane and ethane are often used as collisional energy transfer agents in diode-pumped alkali vapor lasers (DPALs). Problems are encountered because the hydrocarbons eventually react with the optically pumped alkali atoms, resulting in the contamination of the gas lasing medium and damage of the gas cell windows. The reactions require excitation of the more highly excited states of the alkali atoms, which can be generated in DPAL systems by energy pooling processes. Knowledge of the production and loss rates for the higher excited states is needed for a quantitative understanding of the photochemistry. In the present study, we have used experimental and theoretical techniques to characterize the removal of Rb(6^2P) by hydrogen, methane, and ethane.

2.1.2 Background

Diode pumped alkali vapor lasers (DPALs) have been actively developed over the past 12 years [14, 15, 32]. These systems are driven by the optical excitation of the $n^2\mathrm{P}_{3/2} \leftarrow n^2\mathrm{S}_{1/2}$ transition (D2 line) and laser on the $n^2\mathrm{P}_{1/2} \rightarrow n^2\mathrm{S}_{1/2}$ transition (D1 line). The principal quantum number, n, is 3, 4, 5, and 6 for Na, K, Rb, and Cs, respectively. Rapid energy transfer between the $n^2\mathrm{P}_{3/2}$ and $n^2\mathrm{P}_{1/2}$ levels is essential for efficient operation of these lasers. It has been shown that the saturated hydrocarbon molecules CH_4 and $\mathrm{C}_2\mathrm{H}_6$ are excellent energy transfer agents that do not cause significant $n^2\mathrm{P} \rightarrow n^2\mathrm{S}$ quenching [6, 15]. However, there are chemical problems associated with the use of hydrocarbons. In static gas fill systems they slowly react with the optically pumped alkali atoms. The products include alkali hydrides and carbon. Both generate particles that cause light scattering and window contamination [17]. As the C-H bond energies of CH4 and $\mathrm{C}_2\mathrm{H}_6$ are high, reactions with $n^2\mathrm{S}$ and $n^2\mathrm{P}$ alkali atoms are markedly endothermic. Exothermic reactions are possible for alkali atoms that have been promoted to higher energy states. For example, Rb in the $6^2\mathrm{P}$, $6^2\mathrm{S}$, or $4^2\mathrm{D}$ states can react exothermically with H_2 [1, 33], which has a greater bond energy than that of either $\mathrm{H}-\mathrm{CH}_3$ or $\mathrm{H}-\mathrm{C}_2\mathrm{H}_5$. The higher excited levels are populated in DPAL systems via energy pooling processes [17, 34–37]. For Rb, which is the focus of this study, the pooling processes are of the form

$$\mathrm{Rb}(5^2\mathrm{P}) + \mathrm{Rb}(5^2\mathrm{P}) \rightarrow \mathrm{Rb}^* + \mathrm{Rb}(5^2\mathrm{S}) \tag{2.1}$$

where Rb is $6^2\mathrm{P}$, $6^2\mathrm{S}$, or $4^2\mathrm{D}$. All of these states have sufficient energy for the reactions $\mathrm{Rb}^* + \mathrm{HR} \rightarrow \mathrm{RbH} + \mathrm{R}$ ($\mathrm{R} = \mathrm{CH}_3$ or $\mathrm{C}_2\mathrm{H}_5$) to be exothermic. Hence, energy pooling followed by a chemical reaction could be a significant degradation process for hydrocarbon-containing DPAL systems.

We are currently investigating the Rb-hydrocarbon photochemical decomposition processes using pulsed laser excitation techniques. Figure 2.1 shows the relevant excitation and relaxation pathways. The first step in this effort is to determine the rate constants for collisional removal of population from the higher excited states. For Rb, the population transfer out of the 6^2P state induced by collisions with H_2, HD, D_2, N_2, CH_4, and CD_4 was examined previously by Siara and Krause [11]. Their rate constants were deduced from measurements of fluorescence intensity verses collision partner pressure. In the present study, we employ time-resolved fluorescence decay rate measurements as the means to determine the rate constants. The collision partners H_2 and CH_4 were examined to check for consistency with the earlier study, while the kinetics for C_2H_6 were characterized for the first time, to the best of our knowledge. Electronic structure calculations for $Rb^* + H_2$ and $Rb^* + CH_4$ have been carried out to determine the nature of the dominant physical deactivation channels.

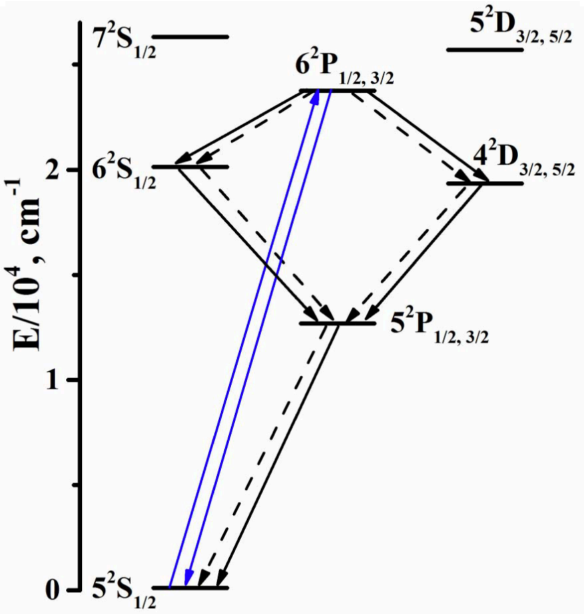

Figure 2.1: Partial energy level diagram for Rb. Transitions of importance for this study are indicated by solid lines (radiative) and broken lines (collisional). The upward arrow indicates the initial pulsed laser excitation.

2.1.3 Experimental

A schematic view of the apparatus used for studies of Rb(6^2P) removal in the presence of H_2, CH_4, and C_2H_6 is shown in Figure 2.2. The fluorescence cell was constructed from a six-way cross for the flow of gases, the passage of the excitation laser beam, and observation of laser induced fluorescence (LIF).

The Rb $6^2P_{3/2} \leftarrow 5^2S_{1/2}$ transition was excited by 10 ns light pulses ($\lambda = 420.29$ nm) generated by an excimer pumped dye laser (Lambda Physik Compex Pro 201/FL3002 combination). The laser intensity was sufficient for saturation of the transition. On the fluorescence cell, the laser entrance and exit windows were mounted on baffle arms (35 cm long) to reduce interference from scattered laser light. Resonance radiation was viewed along a direction that was perpendicular to the laser beam. The light was collected by a 5 cm focal length lens, and focused on the entrance slit of a 0.125 m monochromator (Oriel Corp. Model 1402). The dispersed fluorescence was then detected by an RCA 1P28 photomultiplier tube (PMT). The PMT output was signal averaged using a digital oscilloscope (Le Croy Scope Station 140). The time resolution of the detection system was about 10 ns.

Rubidium vapor was entrained by flowing H_2, CH_4, or C_2H_6 carrier gas over a heated sample holder that contained approximately 0.1 g of Rb at the start of each series of measurements. The temperature of the sample holder was measured using a K-type thermocouple. Needle valves were used to control the gas flow rates. The sample gases H_2 (99.99% purity), CH_4 (99.99%), C_2H_6 (99.99%), and the Rb metal (99.99%, Aldrich) were used without further purification. The fluorescence cell was evacuated by a rotary pump (Welch Duo-seal Model 1402), and the pumping rate was adjusted using a ball valve. Pressure in the fluorescence cell was measured using a capacitance manometer (MKS Baratron model 122 A, 0-10 Torr).

To avoid complications due to radiation trapping [38], the experiments were conducted using low Rb number densities. Measurements of the fluorescence decay made

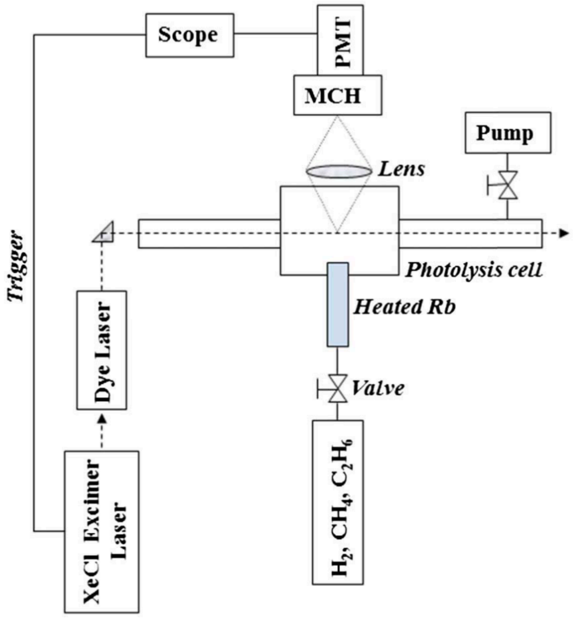

Figure 2.2: Apparatus used to study the removal rate of Rb(6^2P) by H_2, CH_4, and C_2H_6. PMT, photomultiplier tube, MCH; monochromator.

under low-pressure conditions were used to ensure that the observed decay rate was not significantly lower than the previously reported radiative decay rates (indicative of trapping). As the low Rb concentration limited the intensity of the fluorescence signal, relatively wide monochromator slit settings were used to obtain good signal-to-noise ratios. The disadvantage of this approach was that the $6^2P_{3/2} \rightarrow 5^2S_{1/2}$ and $6^2P_{1/2} \rightarrow 5^2S_{3/2}$ emissions could not be resolved. However, this limitation proved to be unimportant for the collision partners and pressure ranges investigated. Evidence that a rapid $6^2P_{1/2} \leftrightarrow 6^2P_{3/2}$ transfer was occurring was provided by the observation of the same decay rates (within experimental error) for initial excitation of the $6^2P_{1/2}$ or $6^2P_{3/2}$ levels. As the excitation of the latter is favored by the upper state degeneracy, this was used for the majority of the measurements.

Figure 2.3 shows typical Rb(6^2P) fluorescence decay curves recorded at T = 380 K for three H_2 pressures. The fast removal of Rb(6^2P) within the first 10 ns was caused by a stimulated emission due to a population inversion of the Rb($6^2P_{1/2}$) $\rightarrow$ $6^2S_{1/2}$

transition. This part of the signal was excluded in fitting the curves to obtain the first order decay rates. The exponential component of each decay curve was analyzed using the nonlinear fitting capabilities of the program Origin (OriginLab, Northampton, Massachusetts).

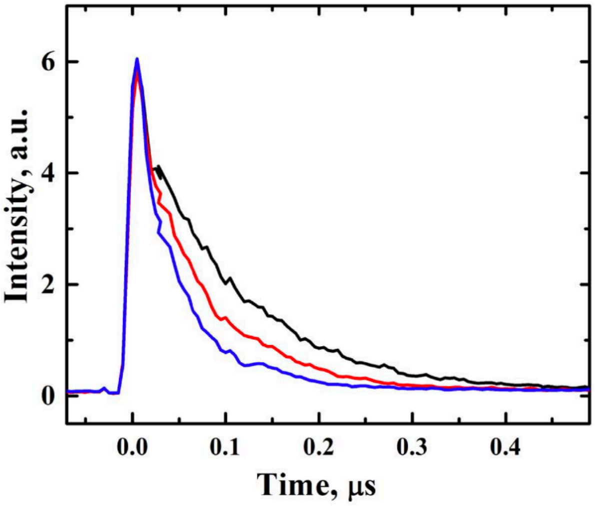

Figure 2.3: Typical Rb(6^2P) fluorescence decay curves at $T = 380$ K and H_2 pressures 0.1 Torr (black curve), 0.35 Torr (red curve), and 0.76 Torr (blue curve)

Figure 2.4 shows a Stern–Volmer plot for the removal of Rb(6^2P) by H_2 at a temperature of T = 380 K. The slope defined a rate constant for removal of Rb(6^2P) by H_2 of $k_{H_2} = 7.0 \pm 0.2 \times 10^{-10}$ cm^3 s^{-1}. The specified error is the $1-\sigma$ value for the data set. Uncertainty in the measurements of the gas temperature introduces a 5% error in the number density of the collision partner. Extrapolation of the fitted line to a zero H_2 number density gave a radiative decay rate for Rb(6^2P) of 7.9×10^6 s^{-1}, which is close to the recommended value [19].

The dependence of the Rb(6^2P) removal rate on the CH_4 and C_2H_6 number densities is shown in Figure 2.5. Linear fits to the data yield rate constants of $k_{CH_4} = (6.2 \pm 0.2) \times 10^{-10}$ cm^3 s^{-1} and $k_{C_2H_6} = (8.1 \pm 0.3) \times 10^{-10}$ cm^3 s^{-1}.

Table 2.1: Cross Sections for Deactivation of *Rb*(6^2P) and *Cs*(7^2P)

Collision Partner	Rb(6^2P)[a] σ/2	Rb(6^2P)[b] σ/2	
H_2	34 ± 2	36 ± 9	60[c]
CH_4	84 ± 2	129 ± 41	30 ± 2[d]
C_2H_6	140 ± 10	-	80 ± 2[d]

[a] This work. Error Includes the effects of temperature

[b] Reference [11]

[c] Reference [39]

[d] Reference [38]. These are the values for $7^2P_{3/2}$

2.1.4 Discussion

The total Rb(6^2P) removal rate constants for H_2, CH_4, and C_2H_6 are close to the gas kinetic values (i.e., transfer or reaction on every collision). In Table 2.1, we compare the collision cross sections derived from the present measurements with those reported by Siara and Krause [11]. To extend the comparison we include the corresponding results for the collisional removal of Cs(7^2P) [38, 39]. Our cross sections for Rb(6^2P) with H2 and CH4 are in good agreement with the results of Siara and Krause [11]. It is also apparent that the cross sections for Cs(7^2P) are of comparable magnitude.

For Rb(6^2P) our measurements indicate that the loss is primarily due to collisional energy transfer. This conclusion is based on the fact that we readily observed emission from Rb(5^2P) following excitation of the 6^2P state. There were both radiative and collisional processes involved in this population transfer. Time-resolved fluorescence from Rb(5^2P) exhibited a strong collisional transfer contribution for all three collision partners. It is established that Rb(6^2P) + H_2 has a reactive removal path, but our measurements show that this is a minor channel compared to a physical energy transfer. Note also that the robust signals from Rb(5^2P) suggests that the collisional processes favored transfer events that had the smallest energy gaps. This could be confirmed by observing emissions from the 6^2S and/or 4^2D states, but the wavelengths of these emissions were outside of the range detected by the photomultiplier used in this study.

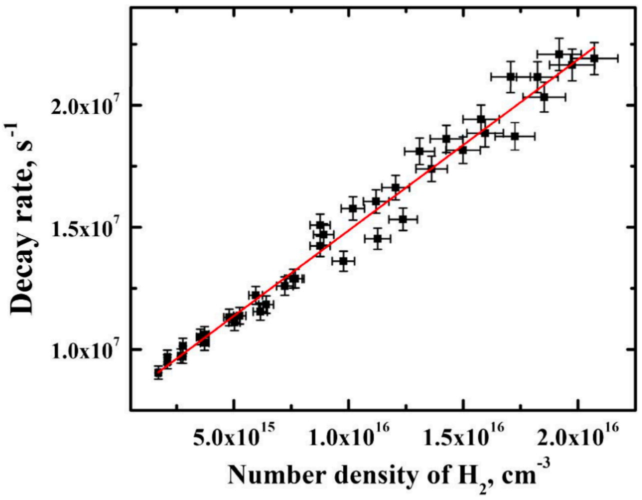

Figure 2.4: Stern-Volnmer plot for the removal of Rb(6^2P) by H_2 at $T = 380$ K. The line is a linear fit to the experimental data (symbols)

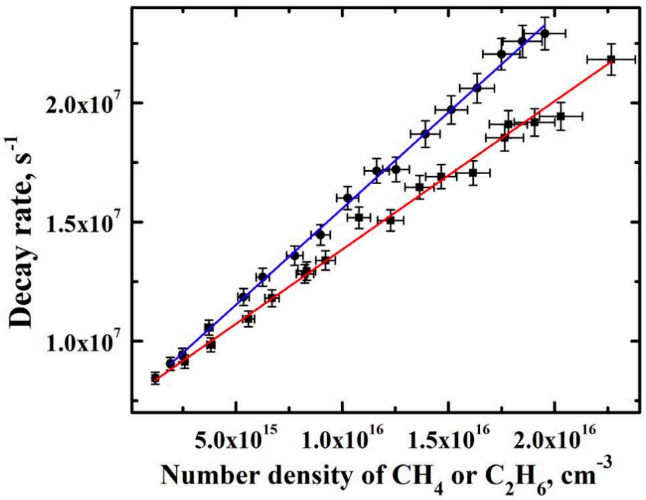

Figure 2.5: Rb(6^2P) decay rates as a function of the CH_4 (■, red) and C_2H_6 (●, blue) number density for $T = 350$ K. The lines are least-squares fits of the experimental data.

To probe the reasons for the large energy transfer cross sections, we have characterized the $Rb+H_2$ and $Rb+CH_4$ interactions using electronic structure calculations. The multi-reference configuration interaction (MRCI) method [40], as implemented in the Molpro 2012 suite of programs [41], was applied. Calculations were carried out using the Cs point group and the properties of the first nine states of A' symmetry were predicted. This set encompassed all of the relevant states arising from the Rb 5*s*; 5*p*; 4*d*; 6*s*, and 6*p* orbitals. The electrons in the 4*s* and 4*p* orbitals were correlated, but the orbitals were constrained to be fully occupied. Hence, for both H_2-Rb and CH_4-Rb the active space consisted of one electron in fourteen orbitals. The internal coordinates of H_2 and CH_4 were held fixed at their equilibrium values. The basis sets were the ECP28MDF relativistic core potential plus valence orbitals for Rb, combined with the Roos ANO basis sets for H and C. Single point energies were calculated for a range of $Rb-H_2$ and $Rb-CH_4$ distances. For $Rb-H_2$ we considered both linear and T- shaped approach geometries. For $RbCH_4$ we used the approach along a $H-CH_3$ bond axis (end-on) and the approach to the center of a tetrahedral face (both C_{3v} symmetry).

Figure 2.6 presents the relevant potential energy curves for T-shaped $Rb–H_2$. The abscissa for this plot (R) is the distance from Rb to the mid-point of the H_2 bond. The unsigned projection of the electronic angular momentum along R ($|L_R|$) was found to be a good quantum number. Figure 2.6 shows an avoided crossing between the 6*p* and 6*s*; ($|L_R|$) = 0 potential energy curves at $R = 4.15$ Å. It is likely that this is an important channel for the removal of $Rb(6^2P)$ by H_2 in which the relaxation proceeds via an electronic to translational (E – T) energy transfer process.

Potential energy curves for the end-on $Rb + CH_4$ approach are shown in Figure 2.7. In this case the abscissa is the Rb – C distance. Similar results (but shifted to a smaller R) were obtained for the face-on approach. For this pair there is no evidence to support a curve crossing mechanism for the $Rb(6^2P)$ energy transfer.

Hence, it seems likely that the relaxation proceeds via an electronic to ro-vibrational (E – V, R) energy transfer process. The Rb energy gaps from 6^2P_J to $6^2S_{1/2}$ are 3582.6 and 3660.1 cm^{-1}, for J = 1/2 and 3/2. This energy can be transferred to the triply degenerate C – H stretching mode (3156.8 cm^{-1}) or the symmetric stretch (3025.5 cm^{-1}). As the energy released by the $6^2P_J - 4^2D_J$ transfer will be slightly greater, the same accepting modes will be accessible. Siara and Krause [11] previously suggested an E – V, R transfer mechanism when they found a smaller transfer cross section for collisions with CD_4. Given the large number of vibrational modes for C_2H_6, it seems reasonable that Rb(6^2P) removal by this collision partner will also be dominated by (E – V, R) transfer.

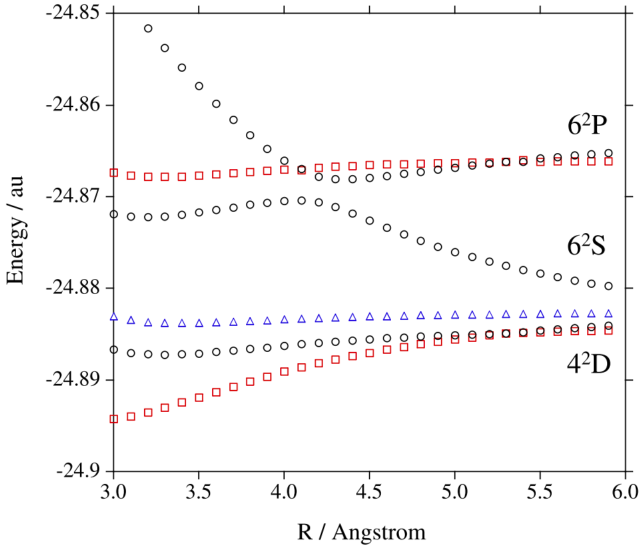

Figure 2.6: Potential energy curves for the side-on (C_{2v}) approach of Rb to H_2. The term symbols on the right hand side indicate the asymptotic atomic state of Rb. The circles, squares, and triangles correspond to states with ($|L_R|$) = 0, 1, and 2. An avoided crossing between the ($|L_R|$) = 0 components of 6^2S and 6^2P states is apparent at 4.15 Å.

In this context, it is also of interest to note that the large vibrational spacing of H_2 (4161 cm^{-1}) renders the Rb $6^2P \rightarrow 6^2S$, 4^2D E – V transfer energetically unfavorable. Transfer would therefore be expected to proceed via the curve crossing. Siara and Krause' s [11] data for H_2, HD, and D_2, which yields cross sections with nearly

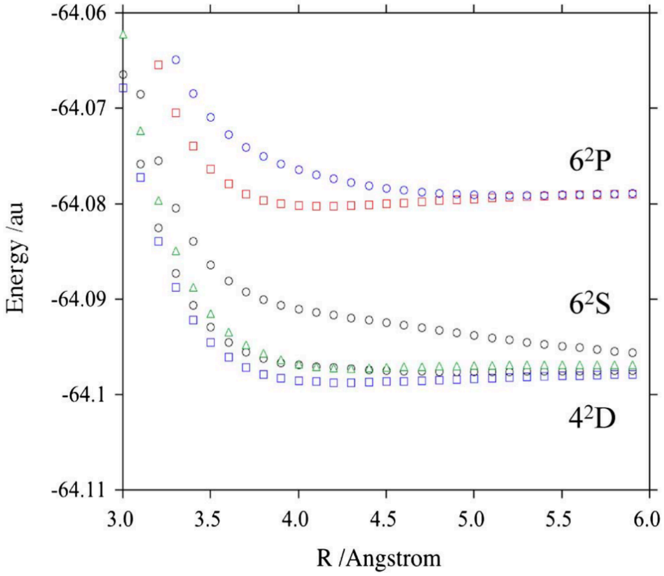

Figure 2.7: Potential energy curves for the end-on (C_{3v}) approach of Rb to CH_4. The term symbols on the right hand side indicate the asymptotic atomic state of Rb. The circles, squares, and triangles correspond to states with ($|L_R|$) = 0, 1, and 2.

overlapping error ranges, supports this view. Their cross sections for D_2, the isotopic variant for which the E – V transfer is clearly exothermic, are the smallest for this group.

Lastly, the rapid deactivation of Rb(6^2P) by CH_4 and C_2H_6 has implications for ionization processes in hydrocarbon-containing DPAL systems. Knize et al. [37] discussed photoionization processes that involved alkali atoms in states that were populated by energy pooling or two-photon excitation. In their kinetic model, these highly excited atoms were subsequently photoionized by either the pump laser or the D_1 laser light. Collisional deactivation of the higher energy states was not considered, but it is evident that such processes are rapid for hydrocarbons, and will markedly reduce the photoionization rate.

2.1.5 Funding

Emory University by the Joint Technology Office; Air Force Office of Scientific Research (AFOSR) (FA9550-13-1-0002); Samara State Aerospace University by the Ministry of Education and Science of Russia (1358, 3.161.2014/K).

Chapter 3

Energy Pooling in Cs

3.1 Background and Motivation

The previous chapters on Rb mention energy pooling processes as being one of the potential causes for the deleterious effects noted in DPAL operation with hydrocarbon buffer gasses. The experiments in Chapter 2 were attempted with cesium many times to find either evidence of Cs(7^2P) loss or CsH production while under the presence of hydrocarbons, with the conclusion being reached that no CsH production was occurring. It is notable to mention that in the Rb paper, there was no reporting of confirmation of the null hypothesis that while using a noble gas, no Rb(6^2P) loss should be observed. Using similar parameters in that experiment, but instead probing the Cs(7^2P$_{3/2}$) → Cs(6^2S$_{1/2}$) emission with He as a buffer gas, significant loss was found in both a flow and static cell while introducing only alkali vapor and noble gasses. This introduced the obvious idea that while the series of experiments did in fact measure loss of Rb(6^2P) population, this need not be attributed to any chemical reaction, and could be attributed to some combination of energy pooling, Penning ionization, and resonantly-enhanced multi-photon ionization. This chapter essentially involves numerous descriptions and arguments as to why the loss in the DPALs is exacerbated by extremely long-lived excited-state and ionized alkali population. In cases where large quantities of hydrocarbon gas are added for spin orbit exchange, the quenching of these higher states by the hydrocarbon increases the temperature of the cell rapidly, and these high temperatures are what cause the catastrophic failure of DPALs. This theory sufficiently describes the reasons for our and others' inability to detect any alkali hydride products; the probability of a an excited cesium atom colliding with a hydrocarbon and resulting in a chemical reaction is extremely small, but if the excited state atoms are in a continuously high powered, excited environment, as they are in an operating DPAL, that low probability is extended over a large number of collisions so that the total number of collision events causes catastrophic laser failure in an extremely short amount of time. Pan et al investigated some of the potential influences of operating parameters on these deleterious processes in side pumped cesium vapor DPALs with flowing gain media [42].

3.1.1 Processes leading to higher excited states and ions of alkali vapor

The possible processes for excitation to higher states of alkali vapors include energy pooling, Penning ionization, Hornbeck-Molnar ionization, and multi-photon ionization. Energy pooling is a phenomenon that involves two excited atoms or molecules colliding and exchanging their electronic energy in the following scheme:

$$\mathrm{M}^* + \mathrm{M}^* \rightarrow \mathrm{M}^{**} + \mathrm{M} \tag{3.1}$$

Where $\mathrm{E}_{\mathrm{M}^{**}} > \mathrm{E}_{\mathrm{M}^*} > \mathrm{E}_{\mathrm{M}}$. It is notable that a number of other potential outcomes for this collision exist, including no electronic energy exchange, and in the case of two highly excited atoms, both atoms could end up in completely different excited states. Rate coefficients have been measured for the processes $\mathrm{Cs}(6^2\mathrm{P}_{3/2}) + \mathrm{Cs}(6^2\mathrm{P}_{3/2}) \rightarrow$

$Cs(nl_{J'})+Cs(6S_{1/2})$ and $Cs(6^2P_{1/2})+Cs(6^2P_{3/2}) \rightarrow Cs(nl_{J'})+Cs(6S_{1/2})$. For both of these processes, the summed total rate coefficients for all observed $Cs(nl_{J'})$ products, including $Cs(7P_{1/2})$, $(7P_{3/2})$, $(6D_{3/2})$, $(6D_{5/2})$, $(4F_{7/2})$, $(4F_{5/2})$, and $(8S_{1/2})$ were found to be $k_{pool} \approx 4 \times 10^{-10}\,cm^3\,s^{-1}$ ($\sigma \approx 1 \times 10^{-14}\,cm^2$) for $Cs(6P_{3/2})$ and $k_{pool} \approx 9 \times 10^{-10}\,cm^3\,s^{-1}$ ($\sigma \approx 3 \times 10^{-14}\,cm^2$) for $Cs(6P_{1/2})$, with temperatures ranging from 337−365 K [43]. The majority of the contributions to the total reported cross sections involved pooling to the (6D) levels, which are approximately double the energy of the (6P) states.

As pooling collisions occur *en masse* throughout the cell, ions are inevitably produced when higher electronic states of alkali vapor collide with each other. This is called Penning ionization, and is defined by the following process:

$$Cs^* + Cs^* \rightarrow Cs^+ + Cs \tag{3.2}$$

The ions produced are singly charged because of the high energy required to produce doubly-ionized alkali ions. Huennekens et. al. estimate the process to have a rate on the order of 10^{-9} $cm^3\,s^{-1}$ [44] for alkali metals. After creating these ions though pooling processes, the pathway back to ground state has a specific favored mechanism. Although a sophomore chemist might expect the most obvious radiative recombination process

$$Cs^+ + e^- \rightarrow Cs + h\nu \tag{3.3}$$

to be dominant because of the coulombic attraction between the oppositely charged species, this has been measured to be slow with $k_{RR} < 10^{-13}$ $cm^3\,s^{-1}$ for potassium [45], so it is likely this component can be ignored in the case of cesium. The electron binding energy must be accounted for. Recombination rates are greatly enhanced if some third body collides concurrently with the charged species and electron in order to absorb the electron-ion binding energy:

$$\mathrm{Cs^{+} + e^{-} + M \rightarrow Cs^{*} + M} \tag{3.4}$$

Where M is some third body and '$*$' is some state $|*\rangle$ of cesium. For a number density of $\mathrm{M = He} = 1.58 \times 10^{19}\ \mathrm{cm^{-3}}$, 760 Torr, at $\mathrm{T} = 460\,\mathrm{K}$, the effective bi-molecular rate coefficient for this process is $\mathrm{k_{3B}^{M}} = 5.9 \times 10^{-10}\ \mathrm{cm^{3}\ s^{-1}}$ [46]. This proposed mechanism still does not completely describe the observed pathway, since observations by Arimondo et all [47], and our own observations, show no dependence on ion lifetime with regards to initial ion concentration. The following conversion process accounts for these observations and is the primary mechanism which is thought to control the kinetics of neutral cesium recovery:

$$\mathrm{Cs^{+} + Cs + M \rightarrow Cs_2^{+} + M} \tag{3.5}$$

$$\mathrm{Cs_2^{+} + e^{-} \rightarrow Cs + Cs^{*}} \tag{3.6}$$

Where $\mathrm{Cs^{*}}$ is a Rydberg state of cesium. Experimental data has shown that the rate of the first equation is very fast. In argon, $\mathrm{k_a} = 2.4 \times 10^{-23}\ \mathrm{cm^{6}s^{-1}}$ [48]. The constant for the dissociative recombination step (Equation 3.6) has been calculated to be $\mathrm{k_{DR}} = 5.26 \times 10^{-7}\ \mathrm{cm^{3}s^{-1}}$ for $\mathrm{T} < 1650$ K, which is much larger than $\mathrm{k_a}$, so that the rate controlling step is the dimer ion formation [49]. The dominant final states of the dissociated atoms are thought to be Rydberg states, which are states that are extremely close to the ionization limit. Radiative lifetimes of ultra-cold magneto-optically trapped Cs have been investigated, and it was found that natural lifetimes for Cs(nl) from $\mathrm{n} = 30 - 60$ ranged from $15 - 40$ µs [50]. Given our observations suggesting rapid quenching of higher excited states of cesium, these Rydberg states would be predominantly non-radiatvely relaxed by hydrocarbons in

DPALs, increasing the heat load.

Wallerstein, Perram, and Rice used a collection of previously reported parameters for all of the previously described processes to create a model for the population of higher lying states in a potassium and rubidium pumped DPAL [46, 51]. Using the models described in those publications, the authors claimed upper bound of 10% potassium loss by transfer to upper states for all reasonable laser conditions. For rubidium the results were less clear. Lineshape data for higher excited one and two-photon transitions are necessary to refine and validate the model. Nevertheless, potential loss was found to be insignificant, and the authors recommend a flowing gain media to remedy the population loss issues. Use of flowing gain media should remove excited cesium from the path of the pump diodes, replacing it with ground state alkali metal and allowing for some cooling to take place. The authors maintain that at low alkali density, photo-excitation processes dominate, while at higher number densities ($> 10^{16}$ cm^{-3}), collisional processes begin to dominate, so tuning the alkali vapor density and pump intensity may yield more optimal parameters that avoid catastrophic failure.

Hornbeck-Molnar ionization is described by the following process [52]:

$$\mathrm{A}^{**} + \mathrm{B} \rightarrow \mathrm{AB}^{+} + \mathrm{e}^{-} + \Delta \mathrm{E}_{\mathrm{HM1}} \tag{3.7}$$

Where A^{**} is a Rydberg atom, B is a ground state atom, and $\Delta \mathrm{E}_{\mathrm{HM1}}$ is the energy defect or excess of the reaction. The current models discount this process as being important for DPAL systems, so this process is excluded. [46, 51].

The effects of energy pooling and ionization have been noted in sodium [53] potassium [54], and rubidium [55]. This process has also previously been investigated extensively in cesium [56–58]. The cross section of the energy pooling processes which lead to ionization are many orders of magnitude larger than the cross sections for multi-photon ionization in nearly all cases. For example, in [55], the authors report a cross section $\sigma = 3 \pm 1.5 \times 10^{-14}\,\mathrm{cm}^2$ for the process $\mathrm{Rb}(5^2\mathrm{P}_{3/2}) + \mathrm{Rb}(5^2\mathrm{P}_{3/2}) \rightarrow \mathrm{Rb}(5\mathrm{D}) + \mathrm{Rb}(5\mathrm{S})$.

3.1.2 Hydrocarbon breakdown mechanisms

Chapter 1 describes theoretical predictions that if a reactive channel exists during an excited $\mathrm{Rb} + \mathrm{CH}_4$ or $\mathrm{C}_2\mathrm{H}_6$ collision exists, that the most likely product is RbH.The predictions suggest that while Rb 5^2S, 5^2P, 6^2S and 4^2D have an endothermic pathway to RbH when colliding with methane or ethane, the states above these have an exothermic path. Beyond direct collisions between electronically excited alkali vapor, alternative pathways for hydrocarbon breakdown exist. Electron collisions with methane have the potential to create the following hydrocarbon breakdown reaction:

$$\mathrm{CH}_4 + \mathrm{e}^- \rightarrow \mathrm{CH}_3^+ + \mathrm{H}^- \tag{3.8}$$

Vibrational excitation of the methane by the impacting electron is also possible. Cross sections for processes involving electron methane collisions are compiled and compared in Reference [59]. The hydrocarbons could be impacted by many electrons, progressively exciting vibrational modes of the gasses and eventually breaking the C−H bonds. Cambier and Madden argue that the conditions in an operating DPAL lead to a non-Maxwell-Boltzmann distribution for free electrons [60]. The free electrons' velocity distributions would then favor electron impact ionization for cesium neutrals, and this has an overall effect of increasing the heat load in the DPAL, as well as creating a new channel for hydrocarbon breakdown through electron impact excitation and eventual breakage of the $\mathrm{C}-\mathrm{H}$ bonds. Such a process would explain our lack of direct evidence of RbH and CsH formation in the presence of ethane and methane, since this process would require continuous, high powered pumping of alkali vapor to generate a sufficient density of hot electrons. If this process were found to be occurring at significant levels, soot and CsH formation would be obvious byproducts of the process.

3.1.3 Optical Trapping

After moving from a flow cell to a static cell due to inability to reliably control various parameters of the flow cell, a phenomenon called optical trapping became relevant due to the potential for increased number density of cesium. Optical trapping becomes obvious in alkali metals at moderate number densities ($\sim 10^{17}$ cm^{-3}). In conditions favorable to optical trapping, radiated photons emitted from excited cesium are re-absorbed by other cesium atoms in the mixture. This has the effect of lengthening observed emissions, and at its most basic level can be though of as being extended by a multiple n of the natural lifetime τ of the molecule, where n is the number of times a single photon produced by a source is absorbed by a trapping substance. Given this rudimentary explanation, it seems that trapping could be easily dealt with with some simple calibration and extrapolation based on temperature. Unfortunately, the practical outcome is that there are a huge number of variables that effect the exact trapping mechanisms including: velocity distributions of offending particles, their spectral emission profiles which depend highly on experimental conditions, and even the geometry of the apparatus and the detector's orientation with regards to that unique geometry. In most kinetic experiments involving atomic vapors, the current strategy to dealing with optical trapping is to avoid it entirely by limiting atomic number density [61].

Optical trapping is important to the overall picture of DPALs because it increases the total energy of the system. When the total energy of the system increases, the lasing cell becomes hotter and the atoms become more excited, causing them to move faster, collide more frequently, and eventually produce the plethora of excited states of cesium that are extremely undesirable in a laser, since the DPAL systems optically perform with all alkali population in the nP and nS states, where n is the principal quantum number of the single valence electron of any alkali metal in its lowest energy configuration.

3.2 Experimental details

3.2.1 Experimental Configuration

The flow cell design is described in Chapters 1 and 2. An overview of the experimental configuration used for the static cell is shown in Figure 3.1. A quartz cell containing a cold finger was filled with 1 gram of cesium in a glovebox. After evacuation overnight to a pressure no more than 10^{-4} Torr, the cell was charged with variable amounts of gasses including He (99.999%, Nexair), Ar (99.999%, Nexair), Kr (99.997%, Spectra Gasses), CH_4 (99.997%, Praxis) , and C_2H_6 (99%, Matheson). The pressures of added gasses were measured with capacitance manometers at room temperature (0−10 Torr, 0 – 100 Torr, MKS Inc.). The charged cell was sealed and taken to an aluminum heating block. The block was heated and maintained at some temperature with a PID controller (Omega, CN7833), and the cold finger, or melt pool was held at a lower temperature, and the temperature defined the alkali vapor number density. An Nd:YAG (Quanta-Ray, DCR-2A) pumped dye laser (Quanta-Ray, PDL-2) was used for pumping the $Cs(6^2S_{1/2}) \rightarrow Cs(7^2P_{3/2})$ transition at $\lambda = 455.5$ nm. A XeCl ($\lambda = 308$ nm) excimer (Lambda-Physik, COMPex Pro 201) pumped dye laser (Lambda-Physik FL3002) produced laser light for product probing. A digital delay generator(Quantum Composers, 9614+) controlled the timing of those lasers' firing, and triggered the oscilloscope as well (Tektronix, 2024). A fast Si photodiode placed close to the vapor cell was used to determine the relative arrival time of the two lasers (Thorlabs, DET10A).

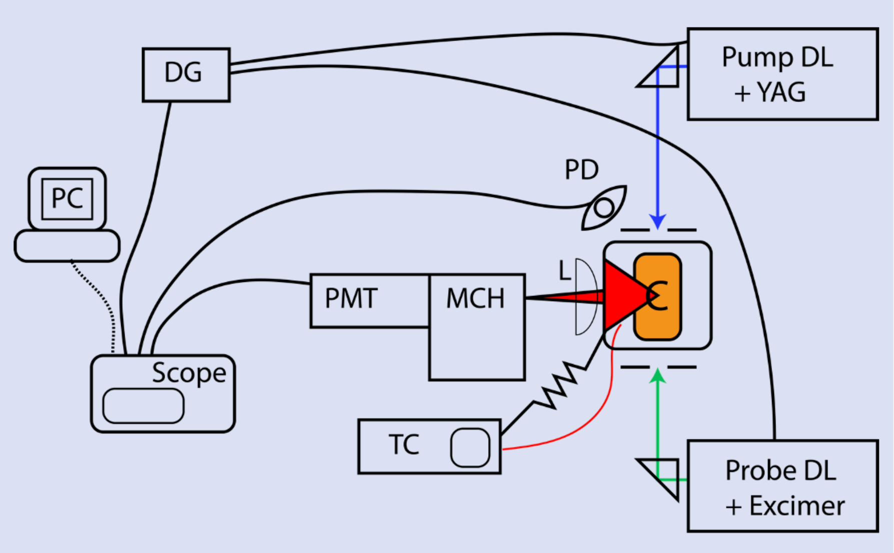

Figure 3.1: Overview of LIF experiments using the Cs Vapor Cell. DG = delay generator, Scope = oscilloscope, PC = personal computer, PMT = photomultiplier tube, MCH = monochromator, PD = photodiode, C = vapor cell, DL = dye laser, TC = temperature controller, L = lens. The red line is a K-type thewrmocouple.

3.2.2 LIF of CsH

The LIF spectrum of CsH in the presence of H_2 is shown in Figure 3.3. The (12,0) band of the $A^1\Sigma^+ \leftarrow X^1\Sigma^+$ transition was selected for its high transition strength and ease of both excitation wavelength production and emission detection. Using PGOPHER [62], fits to the spectrum yielded rotational constants $B'' = 2.676$ cm^{-1} and $B' = 1.146$ cm^{-1}, which is consistent with previously reported values [63]. It is notable that while this spectrum was taken with a cell temperature of 393 K, the simulated spectrum showed a rotational temperature $T_{rot} = 300$ K, which is only slightly above room temperature. The attempted LIF spectra were particularly troublesome upon introduction of hydrocarbons CH_4 and C_2H_6, since it at first appeared that these hydrocarbons were producing CsH in the presence of Cs(7^2P). The CsH LIF signal degraded over the course of about an hour, and it became apparent that some trace gas, likely either water vapor, gas impurities, or H_2 contaminant from previous runs, was responsible for CsH production.

If only trace amounts of CsH are being produced by collisions between hydrocarbons and Cs(7^2P), the amounts are not detectable by the capabilities of the setup used for these experiments. Notably, a long pass filter was used for emission detection with no monochromator, so there were no simple ways to improve sensitivity with the available equipment. One finding that should be mentioned is that collisions between cyclopentadiene and Cs(7^2P) certainly do produce CsH. Pearl Jean is owed acknowledgement for helping synthesize the compound on-demand, and the Blakey lab, a synthetic organic chemistry group at Emory University, for allowing her to use their equipment for synthesis.

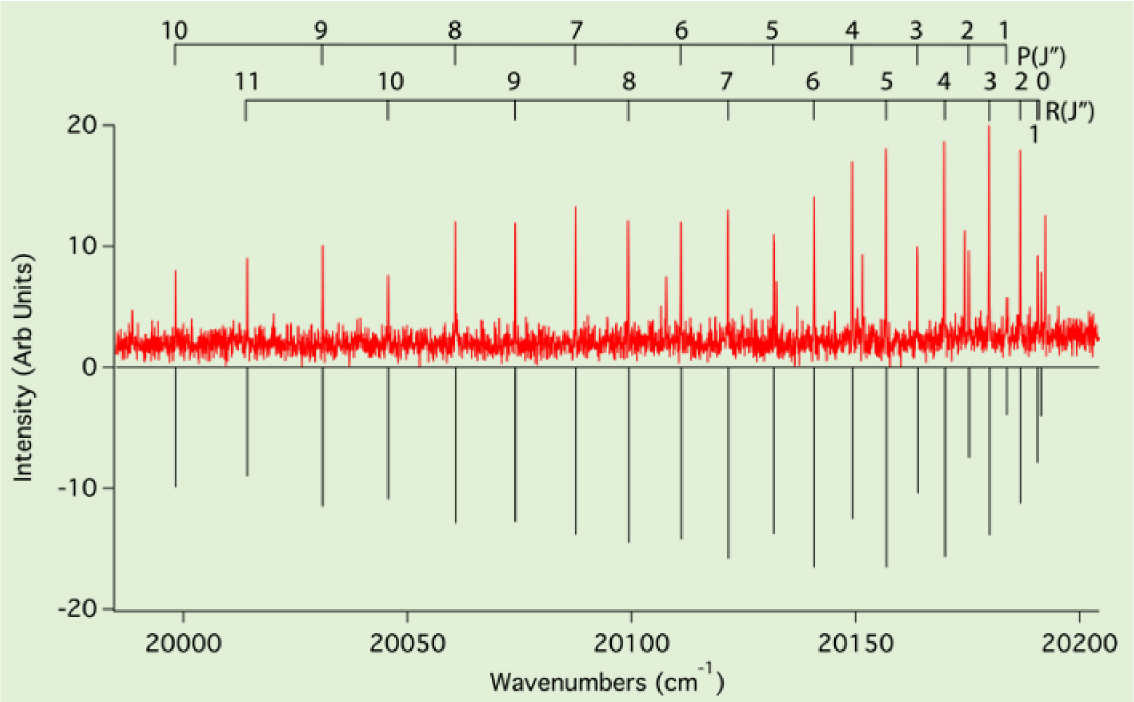

Figure 3.2: Laser Induced Fluorescence spectrum of the (12,0) band of the $A^1\Sigma^+ \rightarrow X^1\Sigma^+$ transition in the presence of H_2, with the Cs vapor being pumped to its 7^2P state shortly beforehand. While similar spectra were found in the presence of CH_4 and C_2H_6, the spectra were not able to be attributed to the addition of those gasses. The top trace is experimental data (black), and the bottom trace is a simulated spectrum (red) using PGOPHER, with $T_{sim} = 300$ K, $B'' = 2.676$ cm^{-1}, and $B' = 1.146$ cm^{-1}.

3.2.3 Cesium number density determination

The number density of alkali metal is determined by the vapor pressure of the surface of the melt pool of alkali metal. The following formulas were used to determine vapor pressure of the cesium vapor cell in Torr at a given temperature for solid and liquid phases respectively, where $\mathrm{T_{melt}} = 301.7$ K [64]:

$$\log_{10}(\mathrm{P_v}) = 2.881 + 4.711 - \frac{3999}{\mathrm{T}} \tag{3.9}$$

$$\log_{10}(\mathrm{P_v}) = 2.881 + 4.165 - \frac{3830}{\mathrm{T}} \tag{3.10}$$

The physicists' ideal gas law then determines the number density of cesium in the cell:

$$\frac{\mathrm{n}}{\mathrm{V}} = \frac{\mathrm{P_v}}{\mathrm{k_B T}} \tag{3.11}$$

Where T is the temperature of the region of interest, in this case, the higher temperature zone of the cell.

3.2.4 DLIF of Excited Cesium

The first evidence that ionization was occurring in the cesium sample is shown in Figure 3.3. While pumping the $\mathrm{Cs}(6^2\mathrm{S}_{1/2}) \rightarrow (7^2\mathrm{P}_{3/2})$ transitions at increasingly high temperatures, routine DLIF spectra revealed transitions that were not possible without some type of energy pooling or ionization process, since emissions appeared from states above the pumped level. Figure 3.3 shows a typical remission profile in the visible range of a subset of the emissions that were detected, with $\mathrm{T} = 423\,\mathrm{K}$ and $[\mathrm{Cs}] = 2.2 \times 10^{14}\ \mathrm{cm}^{-3}$. An analogous result was also observed by former graduate student Daniel Semiaticki with rubidium vapor [65]. At the time, photo-ionization was assumed to be the dominant process due to the presumed limited number density of Rb generated by the flow cell. The redesigned system for the present data allows for constant control of the number density of cesium.

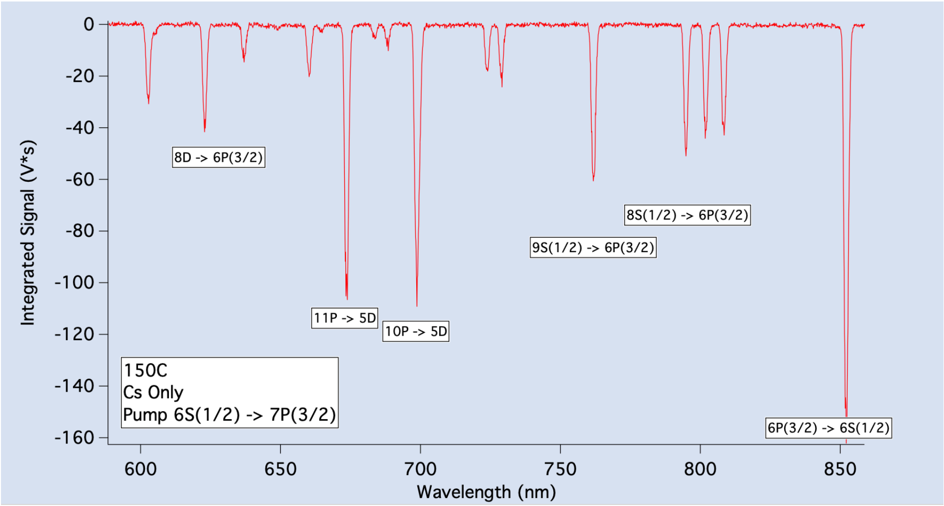

Figure 3.3: DLIF of Cs emissions when pumping the $7^2P_{3/2} \leftarrow 6^2P_{1/2}$ transition at a temperature of 423 K.

3.2.5 Pump-pump-probe cesium depletion experiment

The design of the experiment in Chapter 1 was replicated in the controlled conditions of the static cell setup, with numerous improvements to the experimental design including automation of the experiment so that thousands of traces could be recorded for a given condition.

3.2.6 Ion Collection Experiment

To prove that ions were being generated under our experimental conditions, the flow cell was fitted with a set of parallel plates with a potential difference supplied by a DC voltage unit. A schematic is shown in Figure 3.4. The plates were switched on with a high voltage switching unit (DEI, PVX-4140) modulating a high voltage power supply (Stanford Research Systems, PS350 5000V/25W) at some time after the exciting optical pulse was delivered, with the cut-on time of the pulse being delivered by a DDG (Quantum Composers, 9614+). The DDG also controlled the timing of optical the pump pulse. A LabVIEW program was developed to automatically sweep through ion collection delay times and collect the traces associated with each delay from the oscilloscope (Tektronix, TDS 2014) which was connected to the pulsed plate in parallel with a 1kΩ resistor to ground. The integrated voltage signals from the oscilloscope for each charged-plate time delay after excitation with 1.6 Torr of flowing background He buffer gas are shown in Figure 3.5, and an exponential fit yielded a lifetime $\tau_{\mathrm{Cs}^+} = 91.982 \pm 5.06\,\mu\mathrm{s}$. Comparing this to Reference [47], where a lifetime about 20 µs with no background gas which represents an upper limit given the proposed mechanism, the lifetime values found in this study were about a factor of 5 larger.

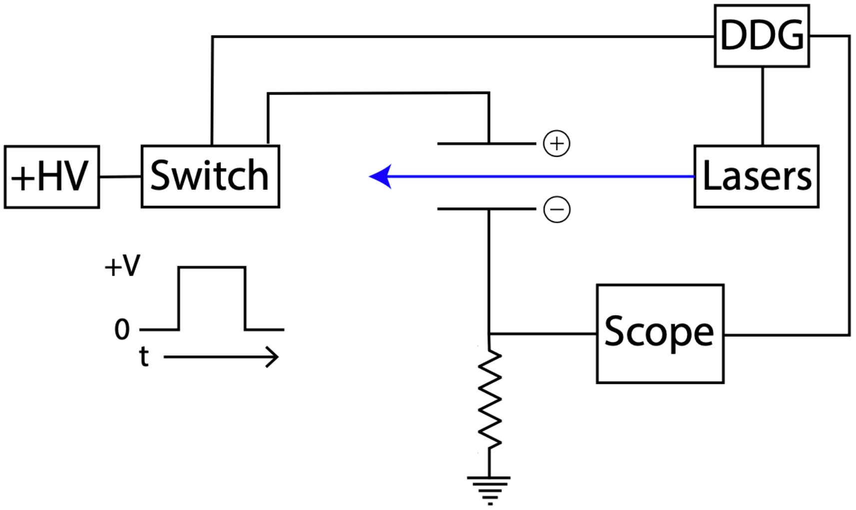

Figure 3.4: Schematic for ion detection as a function of current developed on parallel plates. The resistance value used was 1kΩ.

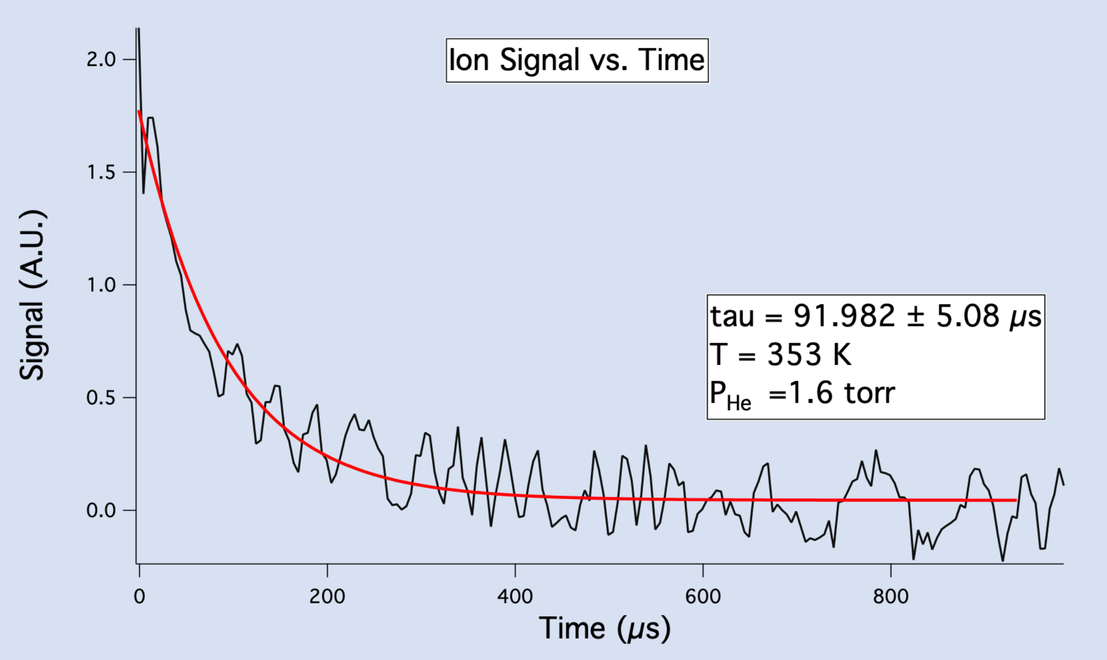

Figure 3.5: Plot of integrated fits of measured current hypothesized to have been produced by Cs^+ at time intervals from $0-1000\,\mu s$. The exponential decay fit yielded a lifetime of $\tau_{Cs^+} = 91.982 \pm 5.06\,\mu s$.

3.2.7 Pooling and recombination

The oscilloscope traces associated each of the peaks in Figure 3.3 yield a peculiar intensity pattern that reinforces the importance pooling and ionization in metal vapor cells. A view of the Cs $10^2P_{3/2,\,1/2} \rightarrow 5^2D_{5/2,\,3/2}$ emissions when exciting the $7^2P_{3/2} \leftarrow 6^2S_{1/2}$ transition in the presence of varying pressures of CH_4 with $T_{cell} = 413$ K. is shown in Figure 3.6. The first spike in voltage is attributed to energy pooling processes that do not result in ionization, and the longer growth and decay is attributed to ion recombination. Increasing the pressure of the colliding gas in the cell appeared to decrease the total number of ions produced, while increasing their rate of formation and decay. Another view of the same transitions are shown in Figure 3.7, this time with no backing gas added, and a temperature variation from 393 K to 433 K in 5 K increments. The pooling and recombination effects are clearly seen to increase in magnitude with [Cs]. Plotting lifetimes of the long tails of Figure 3.7 against the inverse number density of cesium results in the graph shown in Figure 3.8. A slope of $9.07 \times 10^{-8}\mathrm{cm}^3\,\mathrm{s}^{-1}$ was found, with $\mathrm{R}^2 = 0.95$, confirming that the dimer ion recombination pathway is the mechanism of neutral cesium recovery.

Here is a sample kinetics model attempting to quantify the pooling and recombination for cesium, including all of the steps considered to be dominating the kinetics:

$$\mathrm{Cs(7P) + Cs(7P)} \xrightarrow{\mathrm{f{*}k_p}} \mathrm{Cs(6S) + Cs^*} \tag{3.12}$$

$$\mathrm{Cs(7P) + Cs(7P)} \xrightarrow{\mathrm{(1{-}f)k_p}} \mathrm{Cs(6S) + Cs^+ + e^-} \tag{3.13}$$

$$\mathrm{Cs(7P)} \xrightarrow{\Gamma_{\mathrm{7P}}} \mathrm{Cs(6S)} + \mathrm{h}\nu \tag{3.14}$$

$$\mathrm{Cs^+ + Cs} \xrightarrow{\mathrm{k_a}} \mathrm{Cs_2^+} \tag{3.15}$$

$$\mathrm{Cs_2^+ + e^-} \xrightarrow{\mathrm{k_{DR}}} \mathrm{Cs^* + Cs(6S)} \tag{3.16}$$

$$\mathrm{Cs^*} \xrightarrow{\mathrm{k_{20}}} \mathrm{Cs(6S)} + \mathrm{h}\nu \tag{3.17}$$

$$\mathrm{Cs(7P) + Cs(7P)} \xrightarrow{\mathrm{f{*}k_p}} \mathrm{Cs(6S) + Cs^*} \tag{3.18}$$

Where is the fraction of the total pooling constant, $\mathrm{k_p}$, that leads to penning ionization, and $1-\mathrm{f}$ is the fraction of $\mathrm{k_p}$ that leads to energy pooling. The system of ODE's relating these rate coefficients is given by the following:

$$\frac{dn_0}{dt} = \Gamma_{7p} n_{h\nu} - k_1 n_0 n_1 + k_{20} n_2 + k_{DR} n_3 + k_p n_{h\nu}^2 \tag{3.19}$$

$$\frac{dn_1}{dt} = f k_p n_{h\nu}^2 - k_a n_0 n_1 \tag{3.20}$$

$$\frac{dn_2}{dt} = k_{DR} n_3 n_e - k_{20} n_2 + (1 - f) k_p n_{h\nu}^2 \tag{3.21}$$

$$\frac{dn_3}{dt} = k_a n_1 n_0 - k_{DR} n_e n_3 \tag{3.22}$$

$$\frac{dn_{h\nu}}{dt} = -\Gamma_{7P} n_{h\nu} - 2 f k_p n_{h\nu}^2 \tag{3.23}$$

$$\frac{dn_e}{dt} = -k_{DR} n_3 n_e + f k_p n_{h\nu}^2 \tag{3.24}$$

Where n_i are the number densities for Cs(6S) (i = 0), Cs^+ (i = 1), Cs^* (i = 2), and Cs_2^+ (i = 3). Cs^* represents all excited cesium neutral states. Fits for the data shown in Figures 3.6 and 3.7 were attempted. While parameter adjustments for the constants yielded a simulated trace that agrees with the time evolution of the experimental data, the solution space is vast, yielding many different combinations of variable kinetic rates, and only experimental data for $n_2(t)$ was available.

3.3 Recommendations for future work

An ideal alkali vapor source for pooling and recombination effects would include the following features:

- Dual heating zones for precise alkali vapor number density control and window condensation control.
- A system for arbitrarily modifying number densities of buffer gas.
- Metal construction, allowing for a wide dynamic of pressures from mtorr to $\sim$ 1000 Torr.

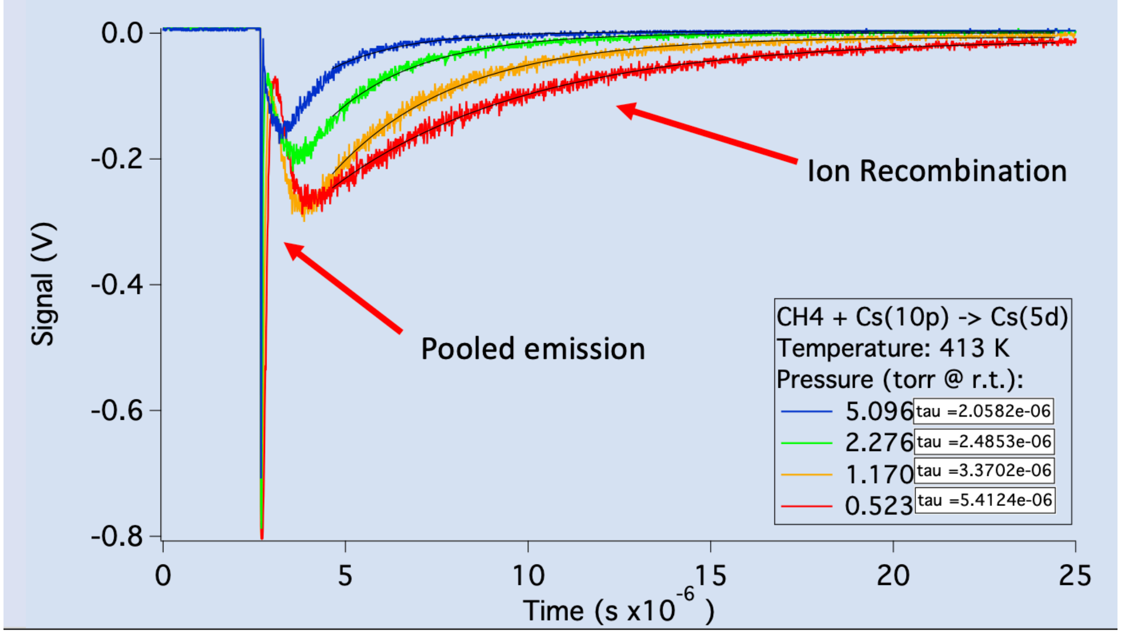

Figure 3.6: Time-resolved fluorescence traces of Cs $10^2P_{3/2,\,1/2} \rightarrow 5^2D_{5/2,\,3/2}$ emissions when targeting the $7^2P_{3/2} \leftarrow 6^2S_{1/2}$ transition in the presence of varying pressures of CH_4 with $T_{cell} = 413\,K$. The initial spike is attributed to pooling processes that do not result in ionization. The secondary growth is attributed to ion recombination.

- Electrical feedthroughs for charged-plate ion collection and analysis
- A variety of tunable CW and pulsed lasers.
- Notch filters centered at critical cesium transitions, with a monochromator for less critical transition monitoring. Notch filters will enhance S/N and will allow for lower number densities of cesium to be used, which mitigates optical trapping problems.
- calibrated capacitance manometers to monitor pressures at all relevant ranges in real-time.
- A variety of photosensors with ∼ 1 ns time response, covering the range of $0.3 - 2\,\mu m$
- Fully computerized data collection systems to eliminate subjectivity in data

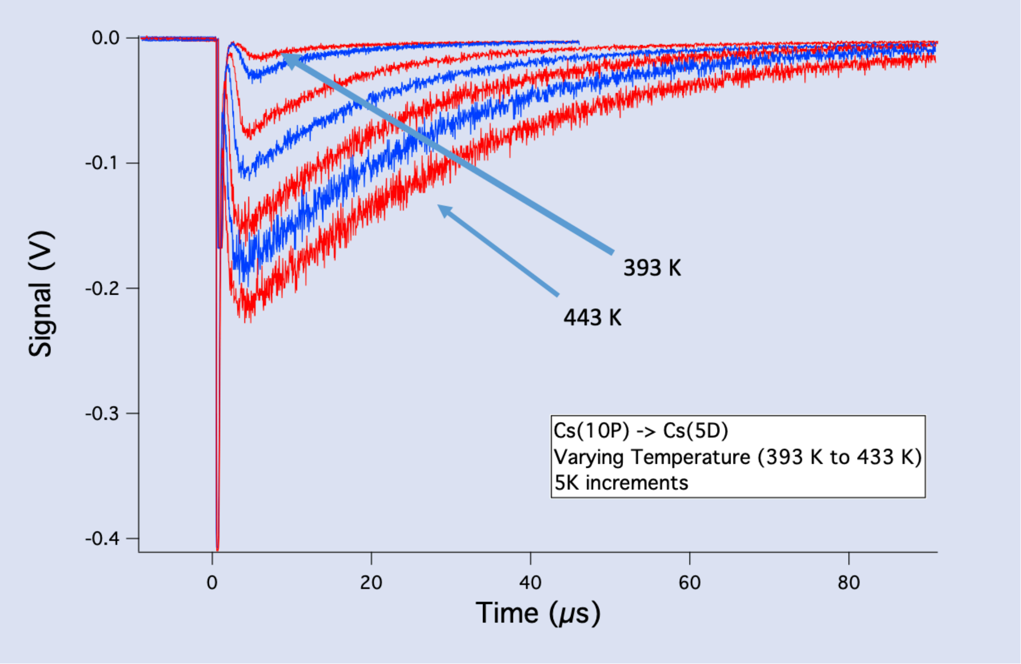

Figure 3.7: Time-resolved traces of $10^2P_{3/2,\,1/2} \rightarrow 5^2D_{5/2,\,3/2}$ emissions when targeting the $6^2S_{1/2} \rightarrow 7^2P_{3/2}$ transition in the presence of varying pressures of C_2H_6 with $T_{cell} = 413$ K. The initial spike is attributed to pooling processes that do not result in ionization. The secondary growth is attributed to ion recombination.

recording and reporting.

- Good sensitivity, but minimal amplification. I found that amplifying stages often influenced temporal characteristics of the signals produced by the photosensors.

Many of these improvements were implemented, and are described in Chapter 4. A static cell is recommended for analysis because of difficulties determining and stabilizing alkali vapor number densities when using a flow cell.

The experiment needs to be broken down into digestible measurements that can be more easily modeled. More data needs to be collected among highly excited states to resolve the complex kinetic situation that is brought about by a combination of trapping, pooling, and ionization processes. Data shown in this section provides a starting point for a large number of projects. The updated apparatus described

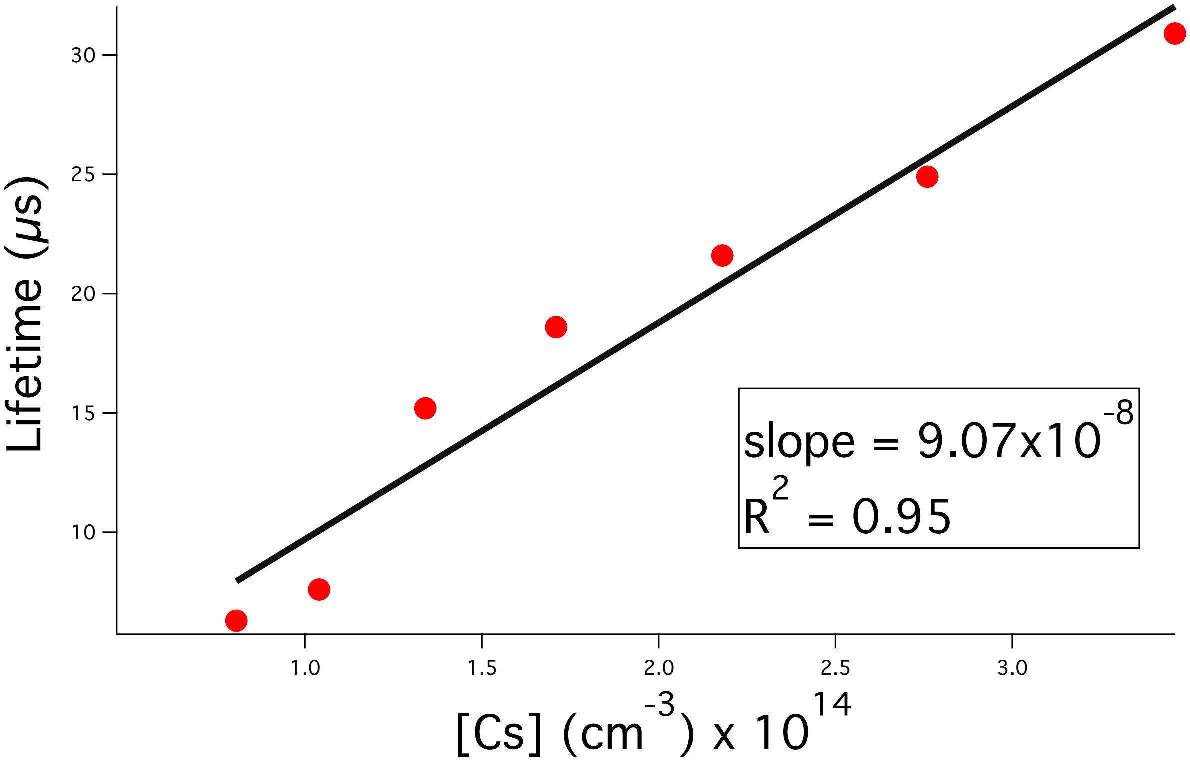

Figure 3.8: Lifetime fits of the tails of the slow decays from Figure 3.7 plotted against the inverse number density of Cs.

in Chapter 5 was not used for this experiment, and the apparatus used for this experiment had several major pitfalls. The first was that the system clearly had leaks in the filling station and cell; these have been fixed by installing Kalrez o-rings in the cell, and by rebuild. Combining the filling station with the rest of the experiment so that live modifications can be made during irradiation and heating of the cell eliminates many issues and hastens data collection. Future work should involve adding a laser that is capable of efficient Nd:YAG third harmonic or UV excimer production so that the Cs(7^2P) state can be accessed with a dye laser. While the information provided in this chapter is qualitatively true, reported rates have large experimental uncertainty due to various problems with the experimental design and execution. Methodically cycling through various excited states of Cs and probing for CsH production in the presence of various hydrocarbons in the new system might reveal that some higher excited state of Cs is reacting with those hydrocarbons to produce CsH.

Energy pooling results similar to those depicted in Figure 3.3 has recently been observed and reported when pumping the Cs($6^2P_{3/2}$) state [66]. In this experiment, the laser pulse used had a duration of 100 µs, which was short enough to avoid catastrophic effects associated with thermal runaway, but long enough to produce higher excited states of cesium through collisional processes. Experiments pumping the Cs($6^2P_{3/2}$) were attempted in our laboratory, but some combination of the pump power and laser duration were not sufficient to observe pooling effects when pumping that state.

Another direction for the experiment is to pump some excited state of cesium or rubidium with a cw-laser while heating the cell to a high temperature. Recreating the conditions where thermal breakdown occurs would allow for the opportunity to identify and possibly quantify the reactions that occur. At high alkali vapor density, constant irradiation of cesium vapor should rapidly increase the temperature of the vapor in the cell. Using the Andor iStar intensified charge-couple device (iCCD) in our lab to capture the dynamics of the thermal breakdown could provide interesting information. While high temperatures will reintroduce the optical trapping problems, purposefully creating the conditions that lead to soot production provides a clear starting point for future study. The highest temperature recorded in the cell was 470 K, so caution should be used when attempting to increase the temperature further.

High resolution capture of the excited state lineshapes is another direction for further experimentation, as noted in [46]. This type of experiment would require high resolution instrumentation such as a tunable continuous-wave laser. A Titanium-doped sapphire laser (Ti:Sapph) or two might work for this purpose, but the Heaven laboratory does not have the doubling crystal for this unit, so the D2 line $Cs(6^2S_{1/2} \rightarrow Cs(6^2P_{3/2})$ ($\lambda = 852.1$ nm) would be a good place to start, given that these values have already been reported [67]. Modifying pressures within the cell should modify the lineshapes of the transitions, and this data would be very useful to kinetic theoreticians ability to create accurate pooling models. True et all have used this scheme to find broadening parameters for the $Cs(6^2P_{3/2}) \rightarrow Cs(8^2S_{1/2})$ transitions in He, Ar, and Kr [68], as well as the lineshapes from $Rb(5^2P)$ to $Rb(4^2D)$ and $Rb(7^2S)$ [69]. If a frequency doubling unit were able to be acquired and made to work for a Ti:Sapph, the $Rb(6^2P)$ and $Cs(7^2P)$ levels would be an excellent target for pressure broadening analysis, and would only require a single laser. The experiment as it is currently designed should require little modification for such an experiment, and the Heaven lab has a chopper and lock-in amplifier, as well as photodiodes, to replicate the recent literature's experimental design.

The final recommendation for this experiment is to look at various 1-1.6 μm transitions for the alkali metals. Chapter 4 describes one experiment, but there are numerous other transitions that can be prepared through collisional transfer from some other state. Quantifying transfer cross-sections by exploiting these longer wavelength emissions will fill in important gaps in knowledge that are necessary to disentangle the complex energy transfer mechanisms that occur in atomic alkali vapor systems.

Overall, the original research from this section combined with evidence from other sources offers a cohesive argument that it is the higher excited states of cesium that are being generated though a variety of undesirable processes that are contributing to the heat load and subsequent failure of DPAL systems at high pump powers. Finding an alternative buffer gas that does not quench the highly excited states creates a problem where the lasing efficiency will decrease by cesium population to those upper sates. The best buffer gas would essentially have the same quenching properties as methane, but with the additional quality of having superior stability in the presence of alkali vapor neutrals and ions in a high temperature environment. If the light hydrocarbons are chosen as the buffer gas, the solution to this problem involves finding a way to offload the heat generated by quenching of the upper states. The current approach to this is to utilize flowing gain media in the DPAL cavity to constantly refresh the cesium and buffer gas [70].

Chapter 4

Spin Orbit Mixing in Cs

4.1 Introduction

Diode Pumped Alkali Lasers (DPALs) are three-level lasers proposed in 2003 that use stacks of diodes to pump an alkali metal vapor from the ground state to the D_2 line, which corresponds to the $\mathrm{n}^2\mathrm{P}_{3/2} \leftarrow \mathrm{n}^2\mathrm{S}_{1/2}$ transition, where n = 2, 3, 4, and 5 for Na, K, Rb, and Cs respectively [71]. Collisional relaxation with a buffer gas allows spin orbit-exchange $\mathrm{n}^2\mathrm{P}_{3/2} + \mathrm{M} \leftrightarrow \mathrm{n}^2\mathrm{P}_{1/2} + \mathrm{M}$, and if this rate is sufficiently fast relative to spontaneous emission to $\mathrm{n}^2\mathrm{S}_{1/2}$, a population inversion on the D_1 line results in lasing down to the ground state, $\mathrm{n}^2\mathrm{S}_{1/2}$. Unfortunately, proper buffer gas selection for the spin-orbit exchange step of the process is difficult for several reasons. A candidate gas must satisfy three constraints: the gas needs to have a large cross-section σ for collisional exchange, it must be chemically nonreactive with the alkali metal, and it must have a small σ for the quenching reaction $\mathrm{n}^2\mathrm{P}_{1/2,\,3/2} + \mathrm{M} \rightarrow \mathrm{n}^2\mathrm{S}_{1/2}$. For example, while lasing has been demonstrated with Rb and Cs DPALs using CH_4 and $\mathrm{C}_2\mathrm{H}_6$ as buffer gases, a reactive channel, likely involving some excited state of alkali metal, produces soot, destroying lasing media and dirtying the windows of the cell [72, 73]. Notably, the reaction need not involve $\mathrm{n}^2\mathrm{P}$, since Penning and multiphotonionization, as well as energy pooling processes, produce higher excited states of alkali metal and singly-charged ions, as observed in Chapter 3. While evidence for the reactions $\mathrm{Rb}(6^2\mathrm{P}) + \mathrm{H}_2 \rightarrow \mathrm{RbH} + \mathrm{H}$ and $\mathrm{Cs}(7^2\mathrm{P}) + \mathrm{H}_2 \rightarrow \mathrm{CsH} + \mathrm{H}$, in the form of RbH and CsH detection with pump-probe laser induced fluorescence (LIF) have been observed [74–76], no direct evidence for alkali-hydride formation has been observed in the presence of hydrocarbons, despite deliberate attempts and theoretical predictions that this could occur [77].

There is a controversy around the role of higher excited states in operational DPALs. Alkali metals are highly susceptible to energy pooling and penning ionization, and these effects scale with alkali vapor density. Furthermore, the relaxation paths to ground state for excited atoms and ions are complex. While the effects of this process seem to be mitigated by introducing flowing gain media, the underlying mechanisms which are thought to contribute to catastrophic failure of DPAL using hydrocarbons as a buffer gas have many gaps in knowledge. Kinetic models have been developed for potassium and rubidium DPALs that attempt to account for the effects of these processes [46, 51], but more data is required, especially for the higher excited states of the heavier alkali metals. For example, while the design of the DPAL exploits the D1 and D2 lines of cesium which have been shown to have extremely low quenching cross sections with hydrocarbons methane and ethane, higher excited states of cesium are strongly quenched by hydrocarbons. Accounting for this unexpected energy loss and heating is critical to designing an optimal DPAL.

Beyond applications toward DPAL development, alternative schemes to this laser have been demonstrated such as utilizing the two-photon transition $8^2\mathrm{S}_{1/2} \leftarrow 6^2\mathrm{S}_{1/2} + 2h\nu$ in Cesium vapor [78]. The two-photon excitation produces a blue laser light from the $7^2\mathrm{P}_{3/2,\,1/2} \rightarrow 6^2\mathrm{S}_{1/2}$ emissions. This two-photon pumping scheme allows for a starting point in investigation of higher excited cesium states and their interactions with gases. Beyond DPAL mechanism elucidation, studies of the kinetics of these higher-excited state alkali vapor lasers are useful for general laser development. Given that there is only one naturally occurring isotope of cesium, Cs-133, alkali vapor cells operating under lasing conditions can be used as frequency reference standards. Other similar schemes involving pumping two-photon transitions have been demonstrated in a variety of alkali metals [79].

4.2 Experimental

An overview of the experimental apparatus is shown in Figure 4.1. Cesium ingot (99.8% purity, Sigma-Aldirch) was placed in a 5 cm long cylindrical sample cell with a reservoir at the bottom. The sample cell was then placed in an aluminum heating block. The cell contained two temperature zones, one being the aluminum cell enclosure, and the other being a stirred oil bath containing the melt pool of cesium, each controlled by one of two proportional-integral-derivative (PID) temperature controllers (Omega, CN7833). The sample cell was connected to a gas line, which was then evacuated with a tubromolecular pump (Pfeiffer-Balzers, TPH240) backed by a rotary-vane pump (Edwards, E2M2) down to a pressure of at least 10^{-5} Torr, which was measured with an Beyart-Alpert type ion gauge (Ideal). After closing the line to evacuation, a separate input line allowed for an arbitrary amount of gas to be added to the sample cell. A solid state relay (SSR) (Crydom, 240D25) allowed for intermittent opening of the system to vacuum for automatic pressure adjustment. Pressure readings used for the measurements were produced by a pair of capacitance manometers at ambient temperature (0 – 10 Torr, 0 – 100 Torr, MKS Inc.), and a combination driver/readout device produced a voltage associated with the measured pressure. (MKS, PDR-C-2C)

The lower zone containing a melt pool of cesium of the sample block was heated to 343 K and the upper zone, where measurements were recorded, to 373 K, to prevent condensation on the windows. Additionally, the number density of cesium in the cell is defined by the vapor pressure of the melt pool so that the number density of cesium can be managed. A $\sim$ 10 ns pulsed frequency-doubled ($\lambda = 532$ nm) Nd:YAG (Big Sky) drove a dye laser (PDL-1 Quanta-Ray) to produce a tunable light source. After directing the beam through the sample cell, the wavelength of the dye laser was tuned to $\lambda = 822.46$ nm which corresponds to half of the energy of the $\mathrm{Cs}(6^2\mathrm{S}) \rightarrow \mathrm{Cs}(8^2\mathrm{S})$ transition, which is an allowed two-photon transition. Effects of radiation trapping were not observed at melt pool temperatures below 353 K.

An output window on the block perpendicular the optical axis allowed for observation of fluorescent emission from the cesium vapor. A condensing optic (f = 5 cm, Thorlabs) was placed between the viewing window and a 1/8 m monochromator (77250B, Oriel). The grating used was ruled at 600 lines/mm with a blaze wavelength of 1000 nm (77299, Oriel). The monochromator was retrofitted with a stepper motor and driver (1067_0B, Phidgets), and the assembly as a bandpass filter for the observations. The filtered light was directed onto a mid-IR photomultiplier tube (H10220A-75 Hamamatsu), and its time-dependent intensity measured with a digital oscilloscope (TDS 2014, Tektronix)

A program was written in LabVIEW 2020 to control, monitor, and record various aspects of the experiment, including pressure, temperature in both regions of the cell, monochromator position, and the oscilloscope readout. Analog measurements from the capacitance manometer and digital signals to control the SSR were accomplished with a data acquisition module (DAQ) (USB-6001, NI).

The measurement campaign consisted of time-resolved fluorescence intensity measurements of the $\mathrm{Cs}(4^2\mathrm{F}_{7/2,\,5/2}) \rightarrow \mathrm{Cs}(5^2\mathrm{D}_{5/2})$ transitions ($\lambda = 1012.34$, 1012.36 nm, respectively). The spin orbit structure was not able to be resolved, so all transitions measured involve both $4^2\mathrm{F}$ levels. The colliding partners investigated in the present study were He (99.999%, Nexair), Ar (99.999%, Nexair), Kr (99.997%, Spectra gases),

CH_4 (99.997%, Praxis) , and C_2H_6 (99%, Matheson). These transitions only appear when a colliding partner interacts with Cs(8^2S) to produce Cs(4^2F), offering an opportunity to directly study the collisional mixing between the Cs(8^2S) and Cs(4^2F) states.

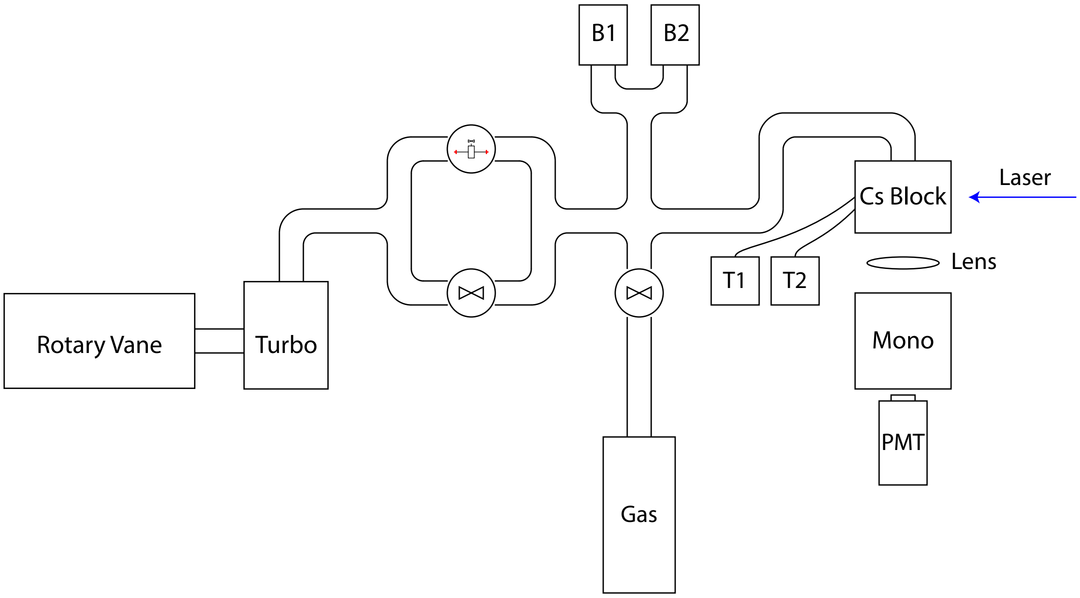

Figure 4.1: Experimental apparatus used for the study. B1, B2; capacitance manometer. T1, T2; PID temperature controller. PMT; photomultiplier tube. Mono; monochromator.

4.3 Results

4.3.1 Kinetic Interpretation

The populations of Cs(8^2S) and Cs(4^2F) are given by the following first-order ordinary differential equations (ODEs):

$$\frac{\mathrm{dn}_2}{\mathrm{dt}} = -\left(\Gamma_2 + Q_2 + R_{21}\right) n_2(t) + R_{12} n_1(t) \tag{4.1}$$

$$\frac{\mathrm{dn}_1}{\mathrm{dt}} = -\left(\Gamma_1 + Q_1 + R_{12}\right) n_1(t) + R_{21} n_2(t) \tag{4.2}$$

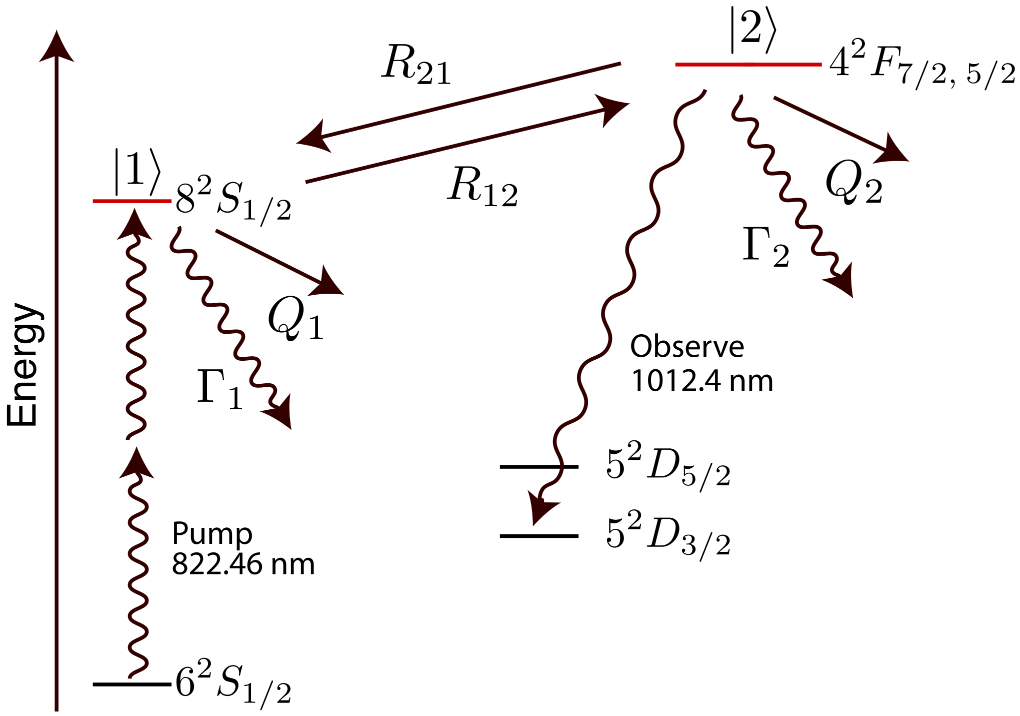

Figure 4.2: Subset of the energy levels of Cs of interest to this study, along with their associated transfer rates. Adding a perturber to excited Cs($8^2S_{1/2}$) Allows for collisional transfer to the 4^2F states. Relative energies are not to scale.

Where subscript '1' denotes $|1\rangle$, Cs($8^2S_{1/2}$), subscript '2' denotes $|2\rangle$, Cs(4^2F), n_i is the population of a cesium state, Γ_i is the rate of spontaneous emission of population in state $|i\rangle$ to all possible lower states, Q_i is the quenching rate, and R_{ij} is the collisional mixing rate for the process $|i\rangle \rightarrow |j\rangle$. For this study, Cs($4^2F_{7/2}$) and Cs($4^2F_{5/2}$) are treated as degenerate due to their negligible energy difference and inability to resolve distinct transitions from those states, giving an effective degeneracy $g_2 = 7$.

If excitation of the $8^2S_{1/2}$ state is treated as a delta function at $t = 0$, $n_1(0) > 0$ and $n_2(0) = 0$. Equations 4.1 and 4.2 can be solved, yielding the following equations [66, 80]:

$$n_2(t) = \frac{n_1(0)R_{12}}{(\lambda_+ - \lambda_-)}\left(e^{\lambda_- t} - e^{\lambda_+ t}\right) \tag{4.3}$$

$$n_1(t) = \frac{n_1(0)}{(\lambda_+ - \lambda_-)}((-\lambda_- + \alpha_1)e^{-\lambda_+ t} + (\lambda_+ - \alpha_2)e^{-\lambda_- t}) \tag{4.4}$$

where λ_+ and λ_- are given by:

$$\lambda_\pm = \frac{1}{2}\left[(\alpha_1 + \alpha_2) \pm \sqrt{(\alpha_1 - \alpha 2)^2 + 4R_{12}R_{21})}\right] \tag{4.5}$$

Where $\alpha_1 = \Gamma_1 + R_{12} + Q_1$ and $\alpha_2 = \Gamma_2 + R_{21} + Q_2$. Direct comparison of the populations of n_1 and n_2 is difficult, but lifetime comparison of the time evolution of the two populations is self-referenced, eliminating the need for both detector calibration given well understood time-response profiles for the photon detectors, and also avoiding having to make an absolute determination of the absolute number densities in $|1\rangle$ or $|2\rangle$. When pumping the $|1\rangle$ state, tracking the relative population of $|1\rangle$ by watching an emission from $|1\rangle$ will yield a double exponential in the form of Equation (4.4). Fitting this exponential will yield two coefficients, associated with each of the components of the exponential, and these two coefficients define Ω:

$$\Omega = \frac{(\alpha_1 - \lambda_-)}{(\lambda_+ - \alpha_1)} \tag{4.6}$$

When pumping state $|1\rangle$ and tracking the time evolution of $|2\rangle$ by watching an emission from $|2\rangle$, the temporal emission profile will resemble a growth characterized by λ_+ followed by a decay characterized by λ_-. As perturbing gas M is added to the system, both λ_+ and λ_- will increase, such that the growth and decay simultaneously increase, with the relationship $\lambda_+ > \lambda_-$ holding true throughout.

Collisional state-to-state mixing rates R_{21} and R_{12} are related by the principle of detailed balance:

$$R_{12}/R_{21} = \frac{g_2}{g_1} e^{-\Delta E/k_B T} \equiv \chi \tag{4.7}$$

where g_i is the degeneracy of the associated state given by $2L_i+1$, k_B is the Boltzmann constant, and $\Delta E = 155\,\mathrm{cm}^{-1}$ is the energy difference of the 2 states.

The principle of detailed balance connects R_{12} and R_{21}, so that given complete information about the time evolution of states $|1\rangle$ and $|2\rangle$ and information about the natural lifetimes of those states, all relevant rate constants $(Q_1, Q_2, R_{12}, R_{21})$ can be described by the following linear system of equations [81]:

$$Q_1 = \frac{1}{1+\Omega}\left(\left[\Omega - \left(\frac{\Omega}{\chi}\right)^{1/2}\right]\lambda_+ + \left[1 + \left(\frac{\Omega}{\chi}\right)^{1/2}\right]\lambda_-\right) \qquad -\Gamma_1 \tag{4.8}$$

$$Q_2 = \frac{1}{1+\Omega}\left(\left[1 - (\Omega\chi)^{1/2}\right]\lambda_+ + \left[R + (\Omega\chi)^{1/2}\right]\lambda_-\right) \qquad -\Gamma_2 \tag{4.9}$$

$$R_{21} = \frac{1}{1+\Omega}\left(\left(\frac{\Omega}{\chi}\right)^{1/2}\lambda_+ - \left(\frac{\Omega}{\chi}\right)^{1/2}\lambda_-\right) \tag{4.10}$$

Given the absence of time resolved data for the temporal evolution of state $|1\rangle$, some approximations can be made to gain insight into the system studied. For example, Equation (4.5) can be solved under the assumption that the quenching rates for $Cs(8^2S)$ and $Cs(4^2F)$ are approximately equal. If $\lambda_+ \gg \lambda_-$, the independent quantities are poorly determined, so this strategy can only be used in the case that λ_+ and λ_- are similar in magnitude.

In the case that $\lambda_+ \gg \lambda_-$, the model can be simplified to the following relations:

$$\lambda_+ = R_{12} + R_{21} + \frac{\chi\Gamma_1 + \Gamma_2}{(\chi + 1)} \tag{4.11}$$

$$\lambda_- = \frac{(\Gamma_1 + Q_1)\chi}{1 + \chi} + \frac{\Gamma_1 + Q_2}{1 + \chi} \tag{4.12}$$

$$\Omega = \chi^{-1} \tag{4.13}$$

The model leads to an exponentially rising and decaying population of $|2\rangle$ characterized by λ_+ and λ_- respectively. Plots of λ_+ and λ_- against [M] give slopes of $k_{21}(1+\chi)$ and $k_{10}\chi(1+\chi)^{-1}+k_{20}(1+\chi)^{-1}$ respectively. This means that the quenching rates Q_1 and Q_2 cannot be determined independently, but their linear combination, Q_{tot}, can be calculated. The rate coefficients k_{12} and k_{21} can then be converted to collisional cross sections, σ_{ij}, using the relation $k_{ij} = \langle v\rangle\sigma_{ij}$, where $\langle v\rangle$ is the average relative speed of the collision pair given by the following equation, assuming hard-sphere collisions in a Boltzmann distribution:

$$\langle v\rangle = \left(\frac{8k_BT}{\pi\mu}\right)^{1/2} \tag{4.14}$$

Here μ is the reduced mass of the collision pair, in this case, Cs and M:

$$\mu = \frac{m_{Cs}m_M}{m_{Cs} + m_M} \tag{4.15}$$

The y-intercepts of the λ_+ and λ_- values found in Stern-Volmer plots of λ_+ and λ_- also contain weighted averages of the lifetime values Γ_1 and $\Gamma 2$ according to the following system of equations [82]:

$$\lambda_+ = \frac{\chi\Gamma_1 + \Gamma_2}{(\chi + 1)} \tag{4.16}$$

$$\lambda_- = \frac{\Gamma_1 + \chi\Gamma_2}{\chi + 1} \tag{4.17}$$

Taking the sums and differences between the two eigenvalues leads to the following relationships:

$$\lambda_+ + \lambda_+ = \Gamma_1 + \Gamma_2 \tag{4.18}$$

$$\lambda_+ - \lambda_- = (\chi - 1)\frac{\Gamma_1 + \Gamma_2}{\chi + 1} \tag{4.19}$$

If data is recorded at very low number densities of perturbing gas, the values of λ_+ and λ_- deviate from linear pressure dependencies, and instead independently converge to Γ_2 and Γ_1 respectively.

4.3.2 Explanation of Stern-Volmer plots

The Stern-Volmer plots presented in Figures 4.4, 4.6, 4.7, 4.8, and 4.3.4 are the results of fitting each trace, which corresponds to the population of Cs(4^2F) in time, to Equation 4.5 with fitting software (Igor Pro 8.04, Wavemetrics) and finding a linear fit to those λ_+ and λ_- versus number density of non-alkali buffer gas added, also called the perturbing gas. The errors shown in the figures are statistical errors only.

4.3.3 Noble gases, He, Ar, Kr

For the noble gases, the data fitting procedure for the case that $\lambda_+ \gg \lambda_-$ was used, since the quenching in all cases was found to be very small. An example for the traces observed which correspond to Cs($4^2\mathrm{F}_{7/2,\,5/2}$) → ($5^2\mathrm{D}_{5/2}$) transitions under varying pressures of He is shown in Figure 4.3. A steady progression appears from what appears to be a simple single exponential at high pressures to the more complicated growth and decay exponential shown in Equation (4.5) is readily apparent. For helium, the fit parameters yielded $\sigma_{12}^{\mathrm{He}} = (4.4 \pm 0.8) \times 10^{-16}\ \mathrm{cm}^{-2}$ and $\sigma_{\mathrm{Q}}^{\mathrm{He}} = (1.7 \pm 0.3) \times 10^{-17}\ \mathrm{cm}^{-2}$ Addition of gasses Ar and Kr yielded results comparable to each other, with $\sigma_{12}^{\mathrm{Ar}} = (2.0 \pm 0.8) \times 10^{-15}\,\mathrm{cm}^2$ and $\sigma_{12}^{\mathrm{Kr}} = (2.2 \pm 0.4) \times 10^{-15}\,\mathrm{cm}^2$. The quenching cross section σ_{Q} information collected for Ar and Kr yielded no statistically meaningful results, but an upper limit of $\sigma_{\mathrm{Q}} < 1 \times 10^{-17}\ \mathrm{cm}^2$

4.3.4 Methane, Ethane Results

For the hydrocarbons, both σ_{12} and $\sigma_{\mathrm{Q}_{\mathrm{tot}}}$ were readily determined using fits to Equation (4.5), under the assumption that $\mathrm{Q}_1 = \mathrm{Q}_2$. The linear fits of the data shown in Figures 4.8 and 4.3.4 yielded formulas with y-intercepts within 50% of the weighted lifetimes noted in [83–85]. For CH_4, the quadratic equation solutions yielded cross sections $\sigma_{12}^{\mathrm{CH}_4} = 5.8 \times 10^{-15}\ \mathrm{cm}^2$ and $\sigma_{\mathrm{Q}}^{\mathrm{CH}_4} = (1.1 \pm 0.2) \times 10^{-14}\ \mathrm{cm}^2$. For C_2H_6, the determined parameters were $\sigma_{12}^{\mathrm{C_2H_6}} = (3.3 \pm 0.7) \times 10^{-14}\ \mathrm{cm}^2$ and $\sigma_{\mathrm{Q}}^{\mathrm{C_2H_6}} = (2.3 \pm 0.5) \times 10^{-14}\ \mathrm{cm}^2$.

The relationships in Equations 4.16 and 4.17 were tested for the methane data, with the two-run averaged fits yielding y-intercepts $2.2 \times 10^7\ \mathrm{s}^{-1}$ and $1.3 \times 10^7\ \mathrm{s}^{-1}$ for λ_+ and λ_- respectively. These values correspond to lifetimes $\tau_{8\mathrm{S}} = 100 \pm 30$ ns and $\tau_{4\mathrm{F}} = 39 \pm 12$ ns. Previously found experimental values for these lifetimes are $\tau_{8\mathrm{S}_{1/2}} = (87 \pm 9)$ ns and $\tau_{4\mathrm{F}} = (40 \pm 6)$ ns, with the spin-orbit components of the $4^2\mathrm{F}$ states having indistinguishable lifetimes. The other data sets yielded similar results.

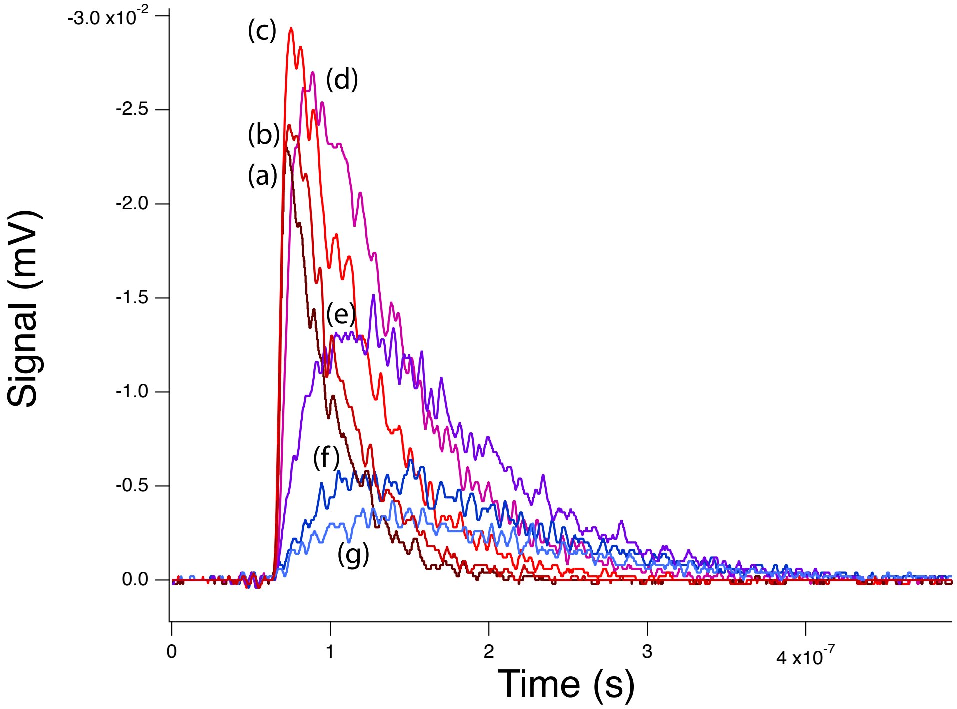

Figure 4.3: Example traces for the Cs($4^2F_{7/2,\,5/2}$) → ($5^2D_{5/2}$) transition in varying number densities of He. (a) 200 Torr, (b) 150 Torr, (c) 75 Torr, (d) 25 Torr, (e) 4 Torr, (f) 1.5 Torr, (g) 0.8 Torr.

Table 4.1: Derived parameters for Cs($8^2S_{1/2}$) → Cs($4^2F_{7/2,\,5/2}$) collisional transfer, units in 10^{-15} (cm^2)

Gas	σ_{12}	σ_Q
He^a	0.44 ± 0.08	0.017 ± 0.003
Ar^a	2.0 ± 0.4	< 0.001
Ar^b	0.12	–
Kr^a	2.2 ± 0.4	< 0.001
H_2 ^{b}	5.1	–
CH_4 ^{a}	5.8 ± 1	11 ± 2
C_2H_6 ^{a}	33 ± 7	23 ± 5

^{a} This work

^{b} Reference [86]

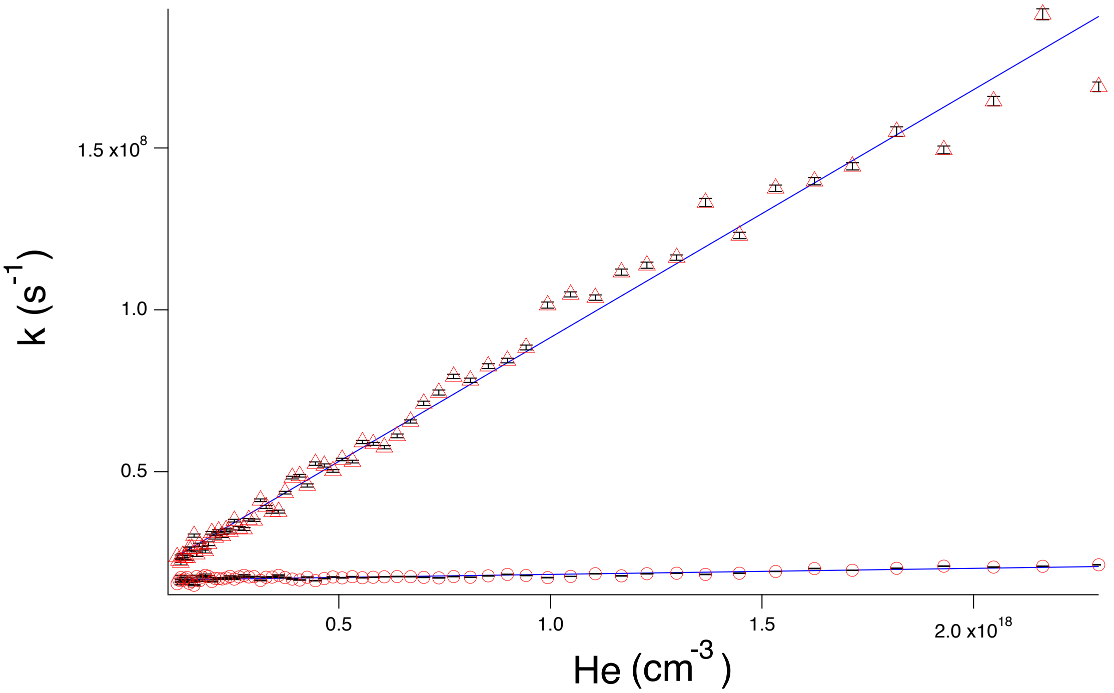

Figure 4.4: Example fit for λ_+ (Top, $\triangle$) and λ_- (Bottom, $\circ$) for the Cs($4^2F_{7/2,\,5/2}$) $\rightarrow$ ($5^2D_{5/2}$) transition in varying number densities of He. The error bars represent errors from the fits for each trace. The solid (blue) lines are least-squares linear fits yielding the fine structure mixing and quenching rates.

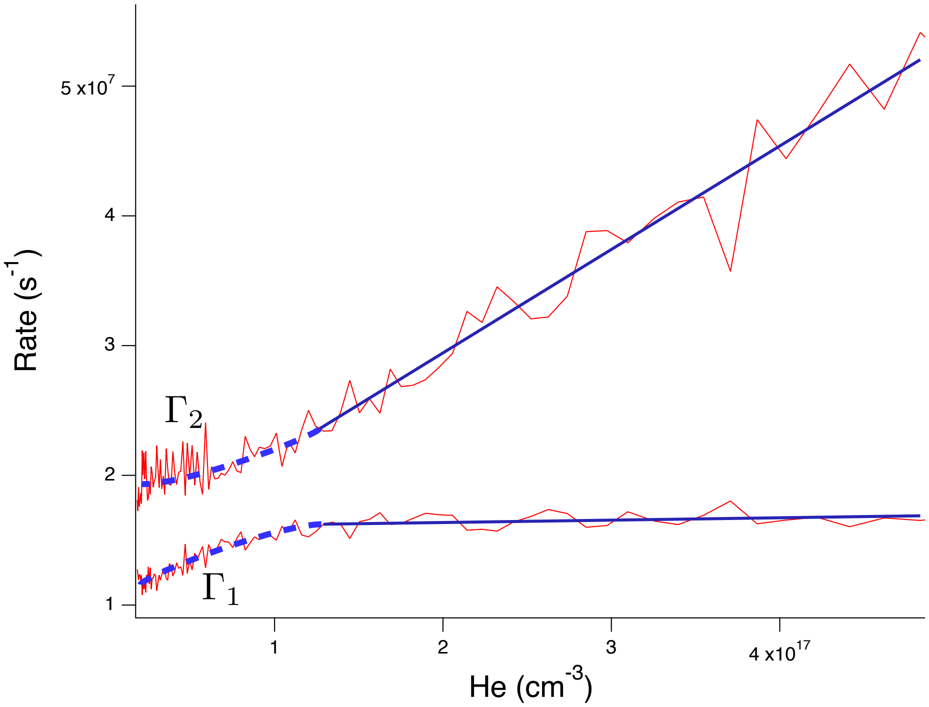

Figure 4.5: Low pressure data for λ_+ (Top, $\triangle$) and λ_- (Bottom, $\circ$) for the Cs($4^2F_{7/2,\,5/2}$) $\rightarrow$ ($5^2D_{5/2}$). The linear fits for λ_+ and λ_- deviate from linear pressure dependencies when measured at low pressures, approaching the rates Γ_1 and Γ_2 as the colliding gas number density goes toward 0.

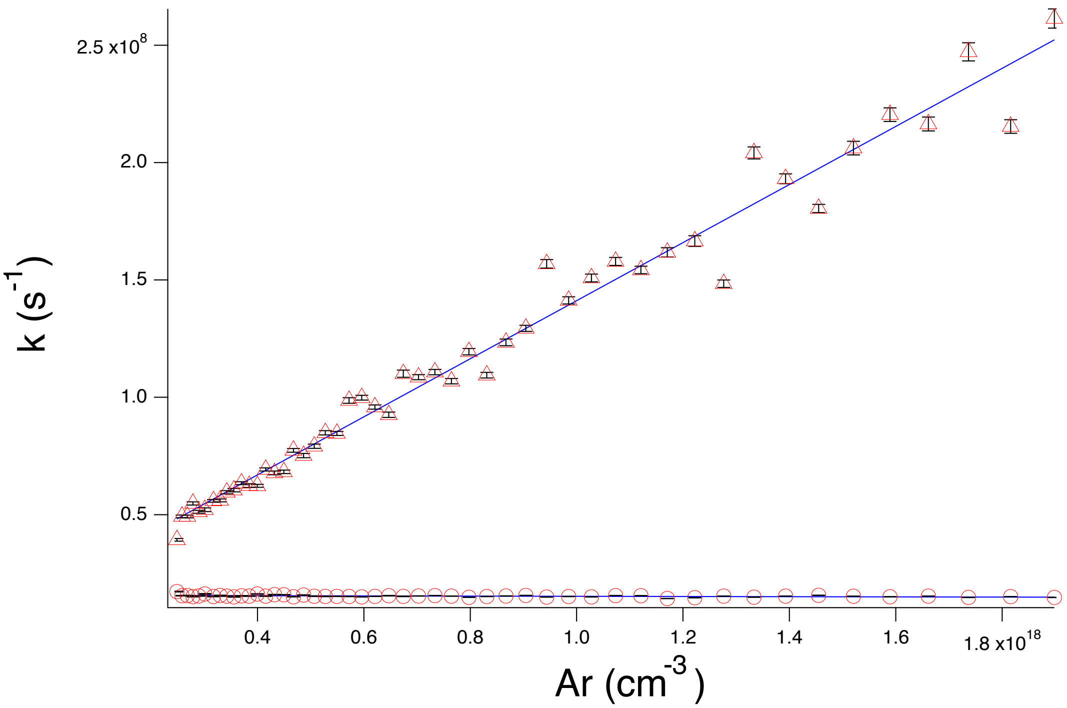

Figure 4.6: Example fit for λ_+ (Top, $\triangle$) and λ_- (Bottom, $\circ$) for the Cs($4^2F_{7/2,\,5/2}$) $\rightarrow$ ($5^2D_{5/2}$) transition in varying number densities of Ar. The error bars represent errors from the fits for each trace. The solid (blue) lines are least-squares linear fits yielding the fine structure mixing and quenching rates.

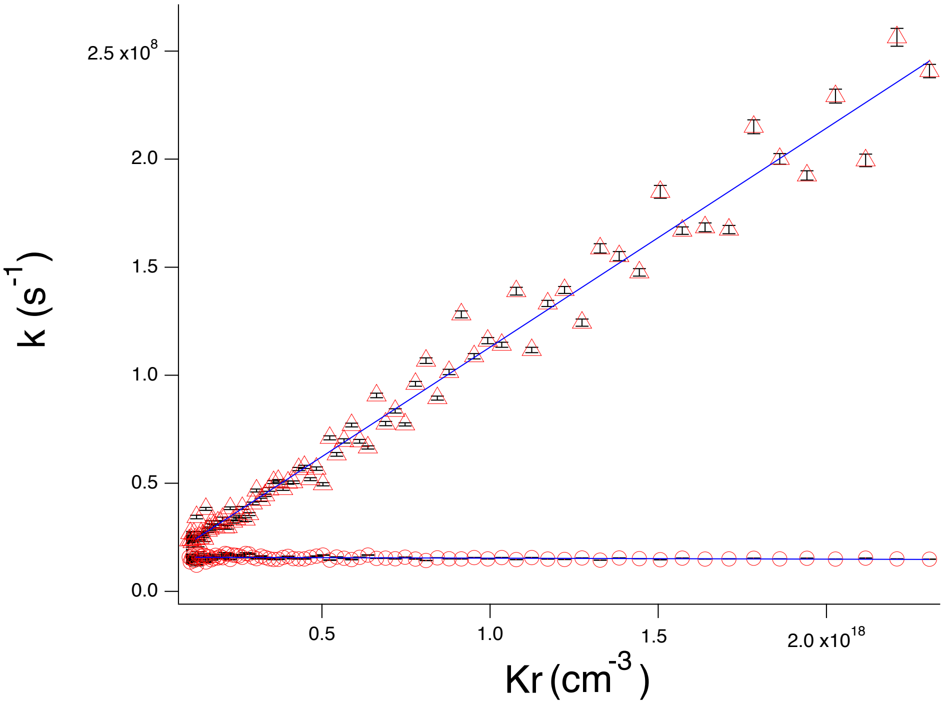

Figure 4.7: Example fit for λ_+ (Top, $\triangle$) and λ_- (Bottom, $\circ$) for the Cs($4^2F_{7/2,\,5/2}$) $\rightarrow$ ($5^2D_{5/2}$) transition in varying number densities of Kr. The error bars represent errors from the fits for each trace. The solid (blue) lines are least-squares linear fits yielding the fine structure mixing and quenching rates.

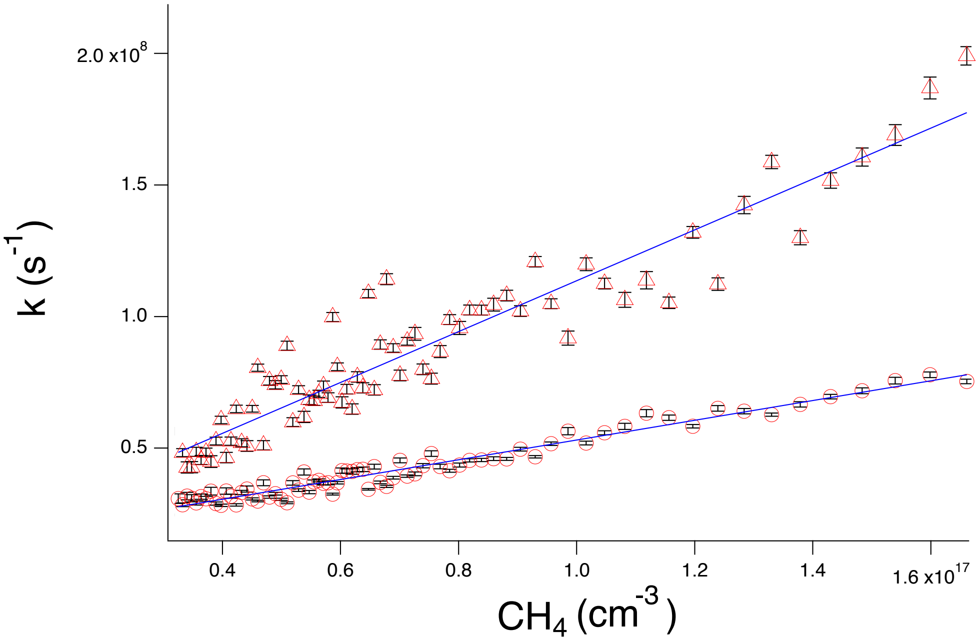

Figure 4.8: Example fit for λ_+ (Top, $\triangle$) and λ_- (Bottom, $\circ$) for the Cs($4^2F_{7/2,\,5/2}$) $\rightarrow$ ($5^2D_{5/2}$) transition in varying number densities of CH_4. The error bars represent errors from the fits for each trace. The solid (blue) lines are least-squares linear fits yielding the fine structure mixing and quenching rates.

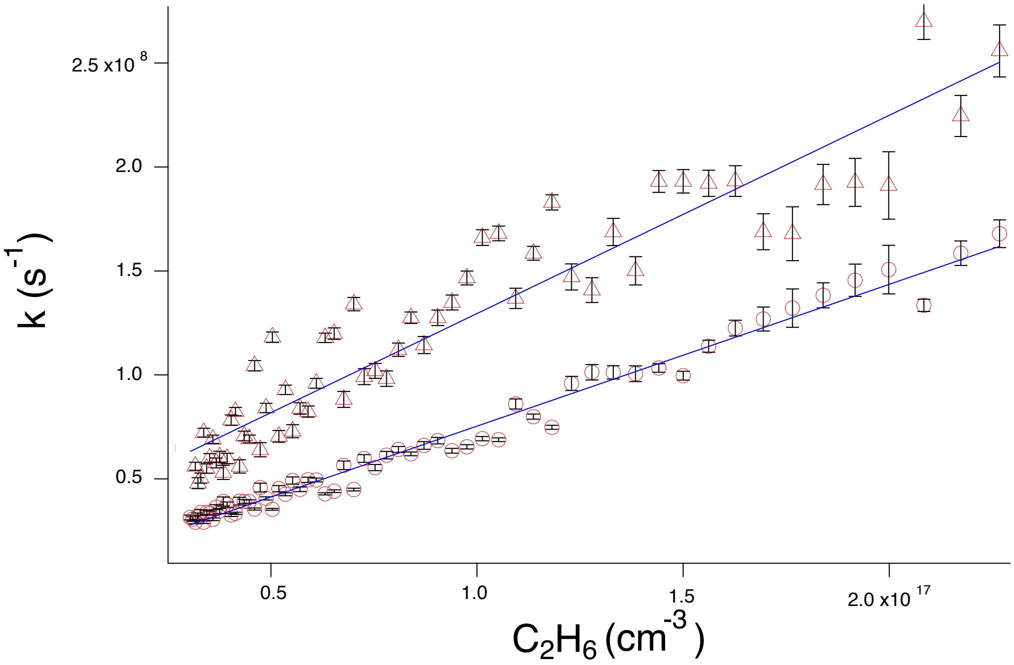

8F C_2H_6 Stern-Volmer plot]Example fit for λ_+ (Top, $\triangle$) and λ_- (Bottom, $\circ$) for the Cs($4^2F_{7/2,\,5/2}$) $\rightarrow$ ($5^2D_{5/2}$) transition transition in varying number densities of C_2H_6. The error bars represent errors from the fits for each trace. The solid (blue) lines are least-squares linear fits yielding the fine structure mixing and quenching rates.

4.4 Discussion

The Cs(8^2S) → (4^2F) state-to-state collisional mixing interaction has previously been studied with gases Ar and H_2 [87], and the results from that study are included in Table 4.1. While the present study uses lifetime analysis as a means of extracting kinetics parameters, previous studies used steady-state integrated intensities to derive their rates, which are susceptible error arising from varying conditions such as PMT gain, wavelength sensitivity, sensor linearity, and fluctuations in [Cs] over time, all of which are avoided by using lifetime-based analysis as long as radiation trapping conditions are avoided. This study also examines a larger array of gases, while excluding H_2 due to problems collecting reliable data due to cell window clouding by CsH formation and deposition on the cell windows, which decreases the laser intensity through the cell as well as decreasing the amount of transmitted fluorescence through the side window.

The discrepancy in argon's influence on state-to-state mixing requires attention. The present study finds a cross-section σ_{12} twenty times greater than in Reference [87]. The new values are recommended due to the lifetime-based methods used in this work. Notably, $\sigma 12$ was found to be greater for Ar and Kr than for He. Previous studies on spin-orbit exchange collisions inducing the processes Cs($n^2D_{5/2}$) → Cs($n^2D_{3/2}$) ($n = 6, 7, 8, 9$) have consistently found that $\sigma_{12}^{Ar} < \sigma_{12}^{He}$ [84, 88–90]. The hydrocarbons and H_2 results show a progression that implies that heavier hydrocarbons increase probability that $Cs8^2(S_{1/2})$ → Cs(4^2F) transfer will occur.

Contamination of the argon and krypton cylinders is a possible reason for the higher values found for k_{12}^{Ar} and k_{12}^{Kr}. However, the slopes associated with λ_{-} in Figure 4.4, helium, with those of Figures 4.6 and 4.7, argon and krypton indicate that less quenching occurred in the latter cases. In fact, the values for $\lambda-$ were found to be slightly negative for several runs, although taking the upper error bounds made them slightly positive. Furthermore, Figures 4.8 and 4.3.4 showing methane and ethane give positive evidence that the models used for these fits properly identify quenching behavior in gases. Furthermore, traces at high pressures, where λ_+ is much faster than the capabilities of our detectors, resembled a single exponential with a decay rate faster than the natural lifetime of the $Cs4^2F$ states.

4.5 Conclusions and Future Work

Experimental collisional quenching and state transfer values have been determined for the process $Cs(8^2S_{1/2}) + M \rightarrow Cs(4^2F_{7/2,\,5/2})$ for gases He, Ar, Kr, CH_4, and C_2H_6. The cross section for transfer between the 8S and 4F states was found to be smaller for helium than for argon and krypton. Hydrocarcarbons CH_4 and C_2H_6 were found to have both higher collisional mixing and quenching cross sections, which were measured for the first time, when compared to H_2 measurements from a previous study.

In regards to expansion of this technique to elucidate the rates of other energy transfer mechanism processes in excited alkali vapors, an analogous $Rb(5^2D) \rightarrow (7^2S)$ excitation transfer mechanism in He, Ar, and H_2 has been investigated [86]. Preparation of the $Rb(7^2S_{1/2})$ state through two photon excitation of ground state rubidium $(6^2S_{1/2})$ and investigation of the collisional transfer process $Rb(7^2S_{1/2}) \rightarrow Rb(4^2F_{7/2,\,5/2})$ through monitoring the $Rb(4^2F) \rightarrow Rb(4^2D)$ emission at 1.344 μm would add experimental values for theorists to include in their DPAL energy transfer models, as well as a direct comparison between S ↔ F cesium and rubidium collisional transfer conducted on the same experimental setup.

Chapter 5

Perturbations of Calcium Oxide

5.1 Preface

This section shows the primary outcome of the modifications I made to the LIF chamber. The publication of this paper shows the strength of the ablation and jet cooling methods our lab uses: this was actually the result of looking for hypermetallic CaOCa. In direct contrast to the alkali vapor experiments, jet-expansions allow you to produce a multitude of products to study. The potential directions of discovery are further augmented upon adding dispersive methods. I recommend to any aspiring scientist that they pursue experimental methods that are likely to produce a variety of positively identifiable results, especially as a beginner. This part of my career was very satisfying, and I enjoyed working with Bob Field, my advisor Michael Heaven, and co-worker Joel Schmitz on this topic!

5.2 Introduction

The electronic spectrum of the CaO molecule is complex due to the large number of low-energy electronic states and the many rovibronic interactions among them [91–103]. Field and co-workers have contributed many pioneering studies of CaO [95–103]. They developed an atomic-ions-in-molecule model and a configurational notation that greatly facilitates discussion of the electronic structure [95, 97]. The ground state of CaO is $X^1\Sigma^+$, which is formally attributed to $Ca^{+2}(^1S_0)O^{2-}(^1S_0)$, a configuration that gives rise exclusively to one electronic state of $^1\Sigma^+$ symmetry. All of the lower energy excited electronic states are attributed to configurations of the Ca^+ + O^- atomic-ion pair. These states can be mapped as combinations of molecular states from CaF [104] (which is a model for the electronic structure of the Ca^+ ion in the axial field of the O^- ion) and NaO [105] (which is a model for the electronic structure of the O^- ion in the axial field of the Ca^+ ion). The Ca^+, $X\sigma$, $A\pi$, and $B\sigma$ orbitals correspond to the $X^2\Sigma^+$, $A^2\Pi$, and $B^2\Sigma^+$ states of CaF. For O^-, the π^{-1} and σ^{-1} hole-orbitals correspond to the $X^2\Pi$ and $A^2\Sigma^+$ states of NaO. The various occupations of these atomic-ion orbitals combine to give the electronic configurations of the CaO molecule. For example, the $Ca^+(4s)O^-(2p\sigma^2 2p\pi^3)$ configuration is specified as $X\sigma\pi^{-1}$ and gives rise to the molecular states $A'^1\Pi$ and $a^3\Pi_i$. A convenient table showing the lower energy configurations and their associated electronic states is given in reference [97].

High-level theoretical studies of CaO have been reported, mostly focused on the ground state and the group of low energy states arising from $X\sigma\pi^{-1}$ ($A'^1\Pi$ and $a^3\Pi_i$) and $X\sigma\sigma^{-1}$($A^1\Sigma^+$ and $b^3\Sigma^+$) [94, 106–110] configurations. Khalil et al. [108, 109] used high-level multi-reference configuration interaction (MRCI) methods with basis sets of 5-zeta quality to predict the potential energy curves, dipole moments and electronic transition dipole moments for the X, A, A', a, and b states. The potential energy curves and wavefunctions from that work were used in subsequent calculations of the ro-vibronic eigenstates [109]. Spin-orbit and L-uncoupling perturbations were included, producing results that could be compared directly with measured term energies. In 2016, Yurchenko et al. [111] refined the potential energy curves and perturbation matrix elements of Khalil et al.[108, 109] by fitting to a very extensive set of experimentally determined term energies. Einstein A coefficients for spontaneous emission were also reported [111]. These data have been included in the ExoMol database [112], the use of which includes the identification of molecular species in the absorption and emission spectra of astrophysical objects. A pertinent example being the detection of CaO emission bands from the wake of a meteorite in 2018 [113]

A comprehensive summary of the experimental studies of the CaO spectrum was provided by Yurchenko et al. [111]. Here we mention selected studies that are of particular relevance to the present work. Data for the $A'^1\Pi(X\sigma\pi^{-1})$ state was obtained from emission spectra and deperturbation analyses. Field et al. [103] observed a vibrationally resolved $A'^1\Pi$ - $X^1\Sigma^+$ chemiluminescence spectrum, and reported band heads that included the $A'^1\Pi(X\sigma\pi^{-1})$ vibrational levels from v = 9 to 21. Rotationally resolved A'-X emission bands, originating from the $A'^1\Pi$ v = 0–3 vibrational levels, were reported by Focsa et al. [114] Perturbations of the A' v = 2 and 3 levels were analyzed and attributed to interactions with the $b^3\Sigma^+(X\sigma\sigma^{-1})$ state. The $a^3\Pi(X\sigma\pi^{-1})$ state was observed as part of the ”orange bands” of CaO. The $a^3\Pi(X\sigma\pi^{-1})$ v = 0 level was characterized through observations of the $c^3\Sigma^+(A\pi\pi^{-1})$ – $a^3\Pi$, $d^3\Delta(A\pi\pi^{-1})$ – $a^3\Pi$, and $e^3\Sigma^-(A\pi\pi^{-1})$ (0,0) bands [95, 97, 100, 101]. Data for the vibrationally excited levels was derived from the $d^3\Delta(A\pi\pi^{-1})$ - $a^3\Pi(X\sigma\pi^{-1}$ (1,1) and $B^1\Pi(A\pi\sigma^{-1})$–$a^3\Pi(0^+)(X\sigma\pi^{-1})$ (3,0) bands, while perturbations, mostly resulting from interactions with the $A^1\Sigma^+$ state, yielded information for the v = 6, 9, and 12 levels of the $a^3\Pi(0^+$ state. Perturbing interactions between $A'^1\Pi(X\sigma\pi^{-1})$ and $A'^1\Pi(X\sigma\pi^{-1})$ were also investigated by Field [103] and Focsa et al. [114] Spin-orbit perturbations between the $A'^1\Pi(X\sigma\pi^{-1})$ and $b^3\Sigma^+(X\sigma\sigma^{-1})$

states have been observed. The $A'^1\Pi$ state is a pure X = 1 state with *e*- and *f*-symmetry components for every value of J. The spin-orbit interaction is homogeneous and follows the $\Delta\Omega = 0$ selection rule. The $b^3\Sigma^+$ state has three spin-components, F_1 and F_3 are of *f*-symmetry and are approximately 50:50 mixtures of X = 0 and 1 whereas F_2 is of *e*-symmetry and of pure X = 1 character. Perturbations involving the F_1 and F_3 components of the b state will be observable in the Q branch of the A'-X transition and those involving the F_2 component will be observable in the R and P branches of the A'-X transition.

Higher energy states have been investigated [91, 92, 96, 97, 115, 116], including those that originate from the $A\pi\pi^{-1}$, $A\pi\sigma^{-1}$, $B\sigma\pi^{-1}$, and $A\sigma\sigma^{-1}$ configurations. Of significance for the present study, Stewart et al. [116] examined the laser induced fluorescence (LIF) spectrum of expansion-cooled CaO over the energy range 28,000 –33,150 cm^{-1}. They observed progressions of the $C^1\Sigma^+(B\sigma\sigma^{-1}) - X^1\Sigma^+$ and $F^1\Pi(B\sigma\pi^{-1}) - X^1\Sigma^+$ and $F^1\Pi(B\sigma\pi^{-1}) - X^1\Sigma^+$ transitions that provided data for the higher vibrational levels of the excited states. Three vibrational bands of an unidentified $\Omega = 0^+ - X^1\Sigma^+$ ($v'' = 0$) transition were also observed. One of these vibronic states was found to be a perturber of the $C^1\Sigma^+(B\sigma\sigma^{-1})$ v = 7 level, pushing this state up in energy by approximately 7 cm^{-1}. In the following we designate this new state as $\gamma 0^+$. Based on an extrapolation of the known vibrational levels of the $C'^1\Sigma^+(A\pi\pi^{-1})$ state, Stewart et al. [116] speculated that the $\gamma 0^+ - X^1\Sigma^+$ bands may be part of the $C'^1\Sigma^+ - X^1\Sigma^+$ system. However, based on spin-orbit selection rules for perturbations mediated by a one-electron operator (e.g., spin-orbit and L-uncoupling interactions), Field [117] argued that the matrix elements between the $C^1\Sigma^+(B\sigma\sigma^{-1})$ and $C'^1\Sigma^+(A\pi\pi^{-1})$ states would be small. He suggested that the $g^3\Pi(0^+)(B\sigma\pi^-)$ or $f^3\Pi(0^+)(A\pi\sigma^{-1})$ states were viable candidates for interactions with the $C^1\Sigma^+(B\sigma\sigma^{-1})$ state, and that the triplet character of the perturbing state could be established by observing the dispersed fluorescence spectrum.

There were two main motives for our reexamination of the spectrum of expansion-cooled CaO. The red spectral range (13,700–17,150 cm^{-1}) was covered as part of our search for bands of the hypermetallic oxide CaOCa [118, 119]. Bands of CaO were present under all of the conditions used for this survey, and rotationally resolved data were obtained for the $\mathrm{A}'^1\Pi(\mathrm{X}\sigma\pi^{-1})$–$\mathrm{X}^1\Sigma^+$ transition for upper state vibrational levels spanning the range v = 10–17. The second objective was to probe the identity of the state that perturbs the $\mathrm{C}^1\Sigma^+(\mathrm{B}\sigma\sigma^-)$ state near v = 7 by means of wavelength and time-resolved fluorescence measurements.

5.3 Experimental

Figure 5.1 shows the instruments used to record LIF and dispersed laser induced fluorescence (DLIF) spectra of CaO. To produce the oxide, 1064 nm light from a pulsed Nd/YAG laser (Quanta-Ray, DCR 1A) was focused onto a Ca rod target (ESPI Metals, 99.9% pure) using a 30 cm focal length lens. The plane polarized output from the Nd/YAG laser was attenuated to the 1–10 mJ/pulse range by means of a Glan-Taylor prism housed in a rotatable stage (Thorlabs CCM1-PBS25-1064-HP/M). The Ca rod was rotated and translated continuously to ensure a fresh metal surface for each ablation pulse. The calcium vapor was entrained in a gas mixture consisting of He and O_2 in a 9:1 volume ratio. The operating pressure behind the valve was 15 atm. Gas pulses were generated by a Parker-Hannifin General Valve (Series 9) with a pulse duration of 1 ms. The entrained metal vapor-gas mixture was supersonically expanded through a 2 mm diameter orifice into a vacuum chamber. The vacuum was maintained by a Roots blower (Leybold, RUVAC WSU 251) backed by a rotary vane pump (Leybold, TRIVAC D65B). The average background pressure in the chamber was typically less than 100 mtorr under gas loading, such that a Campargue expansion was formed.

Molecules present in the supersonic expansion were probed with a pulsed tunable dye laser (Lambda-Physik, FL3002e), pumped by a XeCl excimer (Lambda-Physik, Compex Pro 201), with a pulse repetition frequency of 10 Hz, nominal pulse duration of 10 ns and linewidth (FWHM) of 0.3 cm^{-1}. For the recording of rotationally resolved data, the linewidth was reduced to 0.06 cm^{-1} by adding an intracavity etalon. The absolute wavenumber calibration was established by directing a fraction of the dye laser light through a cell of iodine vapor for simultaneous recording of the I_2 B-X excitation spectrum (LIF detected by a Hamamatsu R955 photomultiplier). Resultant spectra were fitted to the I_2 spectral transition energies of Salami and Ross [120]. To access states of CaO in the near ultraviolet spectral range, the output from the dye laser was frequency doubled by an angle-tuned BBO crystal (Lambda Physik, FL30) while the wavenumber calibration was obtained by using the dye laser fundamental to record the I_2 spectrum.

The laser light was directed into the vacuum chamber, perpendicular to the supersonic expansion, 3 cm downstream from the pulsed expansion nozzle. A two-lens telescope consisting of a collimating lens (Thorlabs, focal length f = 6 cm, diameter D = 5.1 cm) and an achromatic focusing lens (Thorlabs, f = 25 cm D = 5.1 cm) collected light orthogonal to both the jet expansion axis and the probe laser beam axis. Two 4-channel digital delay generators (DDG) were used to control the timings between the ablation and probe lasers, as well as the data collecting equipment (Quantum Composers Model 9614 and Stanford Research Systems DG535).

For LIF measurements, a PMT (Hamamatsu R955) with a longpass filter, typically with a 50% transmission edge at a wavelength 50 nm longer than that of the laser, was placed near the imaging focal point of the lens system. The signal from the PMT was sent to both an oscilloscope (Tektronix TDS 2014) and a pair of time-gated boxcar integrators (Stanford Research Systems, SRS 250). The background signal was subtracted from the fluorescence signal and averaged using an analog signal processor

(Stanford Research Systems, SRS 235). A combination digital/analog input/output data acquisition device (DAQ) (National Instruments, USB-6210) was used to collect the 30-shot averaged data for each laser wavelength, and the laser wavelength was advanced in 0.003 nm increments using the same DAQ. A LabVIEW 2018 (National Instruments) routine managed the incoming and outgoing signals. The uncalibrated wavelength from the laser diffraction grating sine drive, CaO fluorescence signals and I_2 reference data were stored for later calibration and interpretation. Time-dependent fluorescence decay curves for selected rovibronic levels were collected by averaging the oscilloscope traces from 128 laser pulses.

For the DLIF experiments, the emitted light was directed into a monochromator (Instruments SA, 0.64 m, *f*/5.8, 1200 grooves/mm diffraction grating) and then to either an intensified charge-coupled device camera (iCCD) (Andor iStar USB) or the PMT. A custom C program was developed, housed on an embedded system (Arduino Mega 2650), to drive two stepper-motor controller units, one of which controls a stepper-motor connected to the sine drive of the monochromator diffraction grating, and the other was used to raise or lower a mirror that diverted the dispersed light to either the PMT or iCCD to obtain temporal or broadband spectroscopic information, respectively. The camera was controlled and data collected using the Solis (Andor) software.

5.4 Results

5.4.1 The $\mathrm{A'^1\Pi(X\sigma\pi^{-1}) - X^1\Sigma^+}$ bands

LIF spectra recorded in the $13,700$–$17,150\mathrm{cm^{-1}}$ range were dominated by the $\mathrm{A^1\Sigma^+(X\sigma\sigma^{-1})}$ - $\mathrm{X^1\Sigma^+}$ and $\mathrm{A'^1\Pi(X\sigma\pi^{-1})}$ - $\mathrm{X^1\Sigma^+}$ bands. The latter were easily distinguished from the A-X bands as they exhibited Q-branches in the rotationally resolved scans, and much longer fluorescence decay lifetimes. Figure 5.2 shows the rotational structure

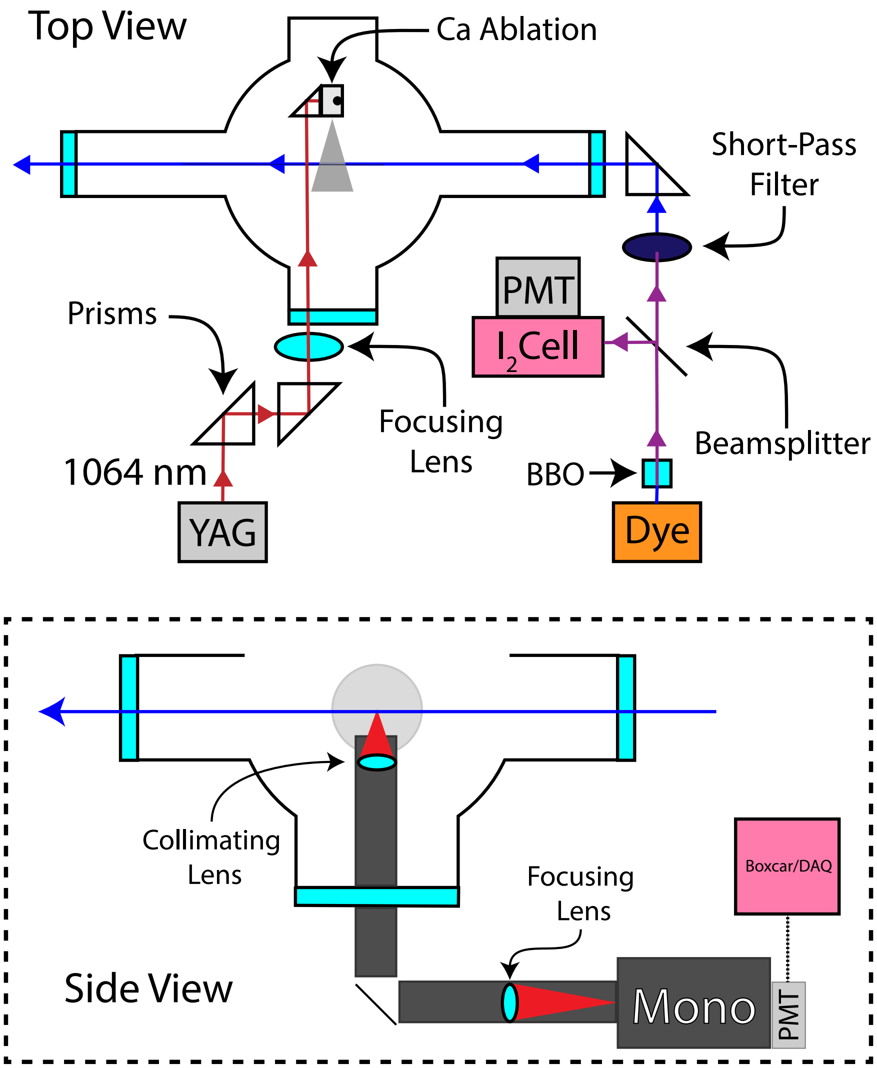

Figure 5.1: Apparatus used to record the laser induced fluorescence and dispersed LIF spectra of CaO. For excitation on the visible range, the BBO crystal and the short-pass filter were removed.

of the A'-X (10,0) band, along with a simulation generated by means of the PGOPHER software [62]. Fitting of the A' state band origins and rotational constants was carried out using PGOPHER. The A'-X bands have a combination difference-defect between the Q-lines and the P/R-lines because these transitions sample respectively *f*-symmetry and *e*-symmetry lambda-doublet components [114]. However, this combination defect was below the precision of the present measurements and the bands were fitted with the lambda-doubling parameters set to zero. The relatively cold rotational population distributions ($T_{Rot} < 100$ K) limited the range of rotational levels observed, such that the fitted centrifugal distortion constants were not statistically significant when treated as adjustable parameters. The theoretical calculations of Yurchenko et al. [111] provide some indication of the magnitudes of the neglected terms. Examination of the $A'^1\Pi(X\sigma\pi^{-1})$ energy levels from the ExoMol database indicates that the lambda doublet splitting for v = 10 increases from 5×10^{-4} cm^{-1} for rotational level J = 1 to 0.08 cm^{-1} at J = 25 (the range of J typically observed in the spectra). Fitting to the mean energies of the -*e* and -*f* parity levels yields a centrifugal distortion constant of 4.4×10^7cm^{-1}, in reasonable agreement with the prediction from the Kratzer relationship of $D_e = 5.5 \times 10^7$ cm^{-1}. As we did not have sufficient resolution to determine the lambda doublet splittings and distortion constants, and did not have a reliable way to predict these values due to the presence of perturbations, they were set to zero in the fits to the rotational line positions. Hence, only the band origins and upper state rotational constants were varied in the spectral fitting. The resulting effective molecular constants are listed in Table 5.1. The rotational line positions for all A'-X bands observed in the present study have been provided as Electronic Supplementary Information. Fluorescence decay lifetimes were recorded for all rotationally resolved A'-X bands. In a series of test experiments, we found that the lifetimes did not exhibit any significant variation with the rotational level. Consequently, the lifetime data reported here were obtained from measurements made using excitation of the most intense rotational line of a given band. Each fluorescence decay curve was well-represented by a single exponential function, and the fitted lifetimes are listed in Table 5.2. Non-linear least squares fitting was carried out using the program Origin Pro 8.5.1.

5.4.2 Wavelength- and time-resolved fluorescence measurements for the $C^1\Sigma^+(B\sigma\sigma^{-1})$ and $\gamma 0^+$ states

Stewart et al. [116] observed transitions to the gamma0^+ state at 32037.0, 32479.5 and 32955.2 cm^{-1}, and these upper states were labeled as the vibrational levels $n-1$, n and n + 1. The $\gamma 0^+$ n state interacts strongly with $C^1\Sigma^+(B\sigma\sigma^{-1})$ v = 7, while $\gamma 0^+$ $n-1$ and n + 1 lie above and below C v = 6 and v = 8, respectively. This smaller vibrational spacing of the $\gamma 0^+$ state relative to that of the $C^1\Sigma^+(B\sigma\sigma^{-1})$ state implies that the $\gamma 0^+$ state belongs to a π^{-1} configuration. To facilitate configurational assignment of the $\gamma 0^+$ state we recorded DLIF spectra for excitation to each of the $\gamma 0^+$ vibronic levels and to the $C^1\Sigma^+(B\sigma\sigma^{-1})$ v = 6, 7, and 8 levels. These data are presented in Figure 5.3, where the energy scale gives the energy of the lower vibronic state of the observed transition relative to $X^1\Sigma^+$ v = 0. The bands in these traces were readily assigned using term energies from the literature. All of the fluorescence transitions to states that lie below 12,000 cm^{-1} terminate on the vibrational levels of the $X^1\Sigma^+$ state. The bands observed in the 12,000–16,000 cm^{-1} range terminate on $X^1\Sigma^+(X\sigma\sigma^{-1})$ v = 1–5 and $a^3\Pi(0^+)$ v = 10–12. Fluorescence decay lifetimes were measured for the six upper states and these are collected in $A'^1\Pi(X\sigma\pi^{-1})$. Decay curves were obtained with the laser tuned to the band head for each vibronic transition, corresponding to an upper state rotational quantum number of approximately J = 4.

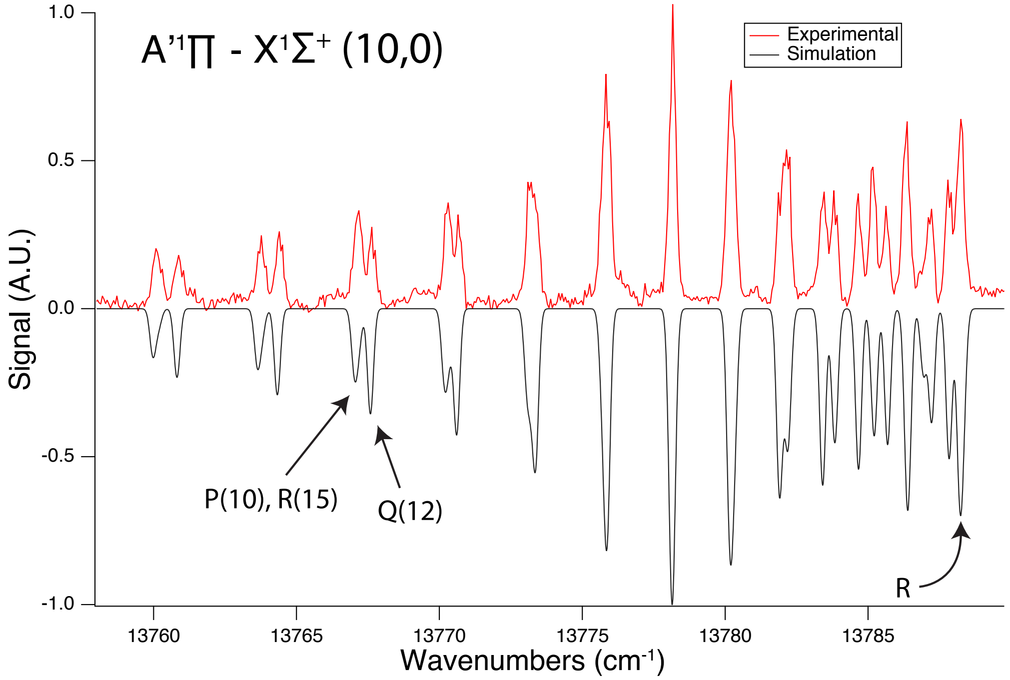

Figure 5.2: LIF spectrum of the CaO $A'^1\Pi(X\sigma\pi^{-1}) - X^1\Sigma^+(10,0)$ band. The downward going trace is a simulation generated using the program PGOPHER.

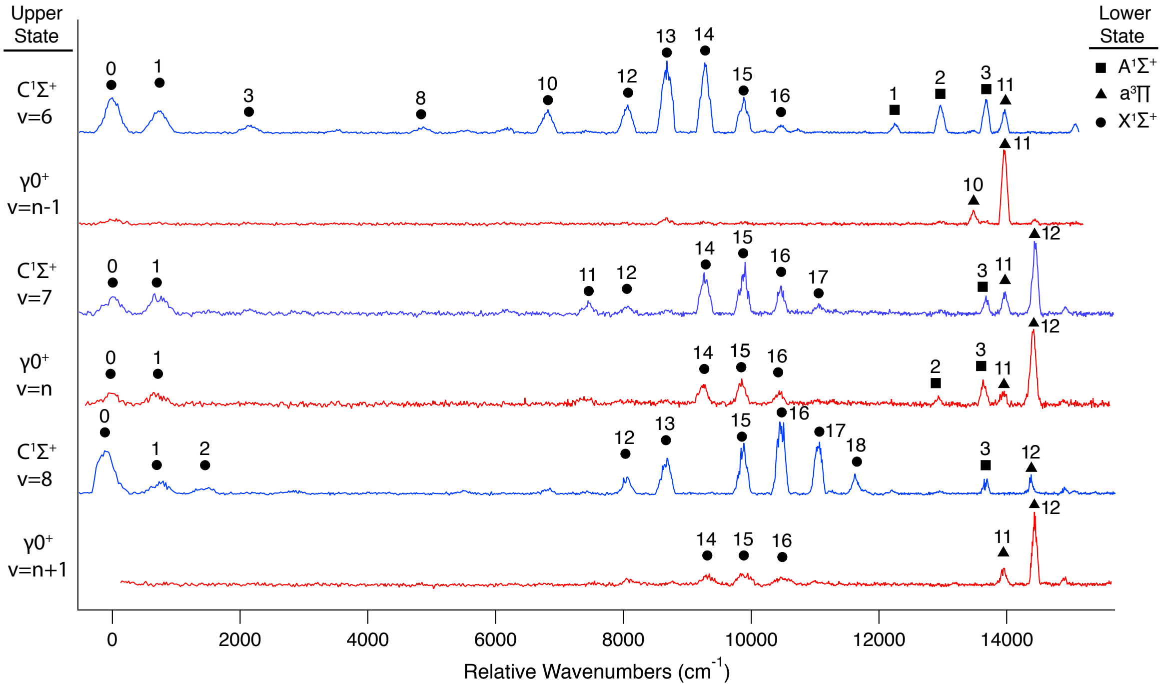

Figure 5.3: Dispersed LIF spectra for CaO using excitation of the states $C^1\Sigma^+(B\sigma\sigma^{-1})$ v = 6, 7, and 8, and $\gamma 0^+$ v = 0, n−1 and n+1. The filled symbols indicate the lower electronic state, with ● = $X^1\Sigma^+$, ■ = $A^1\Sigma^+(X\sigma\sigma^{-1})$, and ▲ = $a^3\Pi(0^+(X\sigma\pi^{-1}$

Table 5.1: Molecular constants for the $A'^1\Pi(X\sigma\pi^{-1})$ state.

v	B_v (cm^{-1})^a	$T_{v,0}$ (cm^{-1})^b	δE, [102]	δE, [111]	Number of lines in fit
10	0.3175	13787.23	2.8	–0.8	38
11	0.3148	14276.94	3.1	–1.1	63
12	0.3121	14761.41	1.6	–1.7	60
13	0.3101	15240.50	2.5	–2.1	52
14	0.3074	15714.72	0.3	–2.8	64
15	0.3079	16184.08	2.5	–3.5	26
16	0.3014	16648.80	5.2	–4.5	20
17	0.3016	17108.85	4.2	–10.7	24
T_{00}					8608.1(2)
ω_e					546.2(1)
$\omega_e x_e$					2.57(1)
B_e					0.3440(15)
α_e					0.00255(11)

$^a 1-\sigma$ error ±0.0005 cm^{-1}.

$^b 1-\sigma$ error ±0.05 cm^{-1}.

Table 5.2: Fluorescence decay lifetimes for the $A'^1\Pi(X\sigma\pi^{-1})$ state.

Vibrational level	$\tau/\mu s^a$
10	2.4
11	2.7
12	2.6
13	2.5
14	2.6
15	2.8
16	2.9
17	2.7

$^a \pm 0.2\ \mu s$ with the inclusion of experimental errors

5.5 Analysis and Discussion

The band origin data for the $A'^1\Pi(X\sigma\sigma^{-1})$ state are compared to the results from the experimental study of Field et al. [103] and the line list data of ExoMol [112] in Table 5.1, where we present the differences between the literature values and the present determinations. Field et al. [103] reported band head data for the red-shaded emission bands, so it was expected that the heads would lie approximately 2 cm^{-1} higher in energy than the origins. There is a significant deviation for the v =

Table 5.3: Fluorescence decay lifetimes for the $C^1\Sigma^+(B\sigma\sigma^{-1})$ state.

State	τ/ns[a]
$C^1\Sigma^+(B\sigma\sigma^{-1})$ v = 6	29
$C^1\Sigma^+(B\sigma\sigma^{-1})$ v = 7	32
$C^1\Sigma^+(B\sigma\sigma^{-1})$ v = 8	24
$\gamma 0^+ n-1$	46
$\gamma 0^+ n$	35
$\gamma 0^+ n+1$	42

[a] ± 5 ns, with the inclusion of experimental errors.

17 level, but it is apparent from both the rotational constant and the term energy that this level is perturbed in the ExoMol model [111]. The last column in Table 5.1 is the difference between the R(0) transition energies obtained from the ExoMol line list [111] and the measured values. The difference increases with increasing v, suggesting that the perturbation model requires further refinement. We also compared rotational constants derived from the ExoMol [111] data to the measured values. For this purpose, we generated rotational constants from ExoMol by fitting the rotational energies to the rigid rotor expression $E_v(J) = B_vJ(J+1)$ for the range of rotational levels sampled by the jet-cooled spectra (J = 1–25). With the exception of B_{16} and B_{17} (predicted values of 0.3026 and 0.3062 cm^{-1} and observed values of 0.3014 and 0.3016 cm^{-1}), the ExoMol rotational constants were within the experimental uncertainties of the constants given in Table 5.1. Rovibrational constants for the $A'^1\Pi(X\sigma\sigma^{-1})$ state were determined by fitting to the energy levels that appeared to be relatively unperturbed. We have used the v = 0 and 1 term energies provided by Focsa et al. [114] and the v = 10–15 data from the present measurements. The vibrational term energies were fit to the expression

$$T_{v,0} = T_{0,0} + \omega_e v - \omega_e x_e v(v+1) \tag{5.1}$$

The standard deviation of the fit was 0.23 cm^{-1}, and the constants are listed in Table 5.1. Trial fits that included the $x_e y_e$ anharmonicity constant did not yield statistically significant results for this parameter. Rotational constants for this same set of vibrational levels were fit by the expression

$$\mathrm{B_v = B_e - \alpha e(v + 1/2)} \tag{5.2}$$

and the resulting constants are given in Table 5.1. The standard deviation for this fit was 0.0007 cm^{-1} (this was the standard deviation of $\mathrm{B_{v_{obs}} - B_{v_{fit}}}$).

We examined the energy level predictions from the ExoMol [111] model to identify the state that would be the most probable cause of the perturbation of the $\mathrm{A'^1\Pi(X\sigma\sigma^{-1})}$ v = 17 state. It was immediately apparent that the calculated energies for the $\mathrm{A'^1\Pi(X\sigma\sigma^{-1})}$ v = 17 (17098.7 cm^{-1}) and $\mathrm{b^3\Sigma^+(X\sigma\sigma^{-1})}$ v = 14 (17109.9 cm^{-1}) states were close enough for a significant interaction. These states can be coupled by the one-electron spin-orbit operator to give 0 matrix elements of the form [103, 114] $\mathrm{H_{SO} = a_\pi \langle A', v'|b, v\rangle}$, where the term in bra-ket notation is the vibrational wavefunction overlap integral, and $\mathrm{a_\pi}$ is the spin-orbit coupling constant for $\mathrm{O^1}$ (approximately 121 cm^{-1}) [103]. A quantitative test of this model was made using Morse potential energy curves (MPEC) for the $\mathrm{A'^1\Pi(X\sigma\sigma^{-1})}$ and $\mathrm{b^3\Sigma^+(X\sigma\sigma^{-1})}$ states, in order to generate vibrational wavefunctions and overlap integrals. The MPEC for the $\mathrm{A'^1\Pi(X\sigma\sigma^{-1})}$ state was determined using the molecular constants given in Table 5.1. The MPEC for the $\mathrm{b^3\Sigma^+(X\sigma\sigma^{-1})}$ state was more difficult to assess due to the lack of spectroscopic data (only the v = 1 level has been observed [99]). As a starting point we used the theoretically predicted of constants [108] $\mathrm{T_0}$ = 9282, $\mathrm{x_e}$ = 585.7 and $\mathrm{x_e - x_e}$ = 3.16 cm^{-1}, with an equilibrium distance of $\mathrm{R_e}$ = 1.96Å. The energy levels generated from these parameters were compared to the experimentally determined term energy for $\mathrm{b^3\Sigma^+(X\sigma\sigma^{-1})}$ v = 1 of 10073.3 cm^{-1} [99], and the predictions from ExoMol. The above molecular constants underestimated the known energy of the $\mathrm{b^3\Sigma^+(X\sigma\sigma^{-1})}$ v = 1 level and the ExoMol prediction that the $\mathrm{b^3\Sigma^+(X\sigma\sigma^{-1})}$ v = 14 level is just above $A'^1\Pi(X\sigma\pi^{-1})$, v = 17. Consequently, we adjusted the T_0, x_e and x_ex_e values for $b^3\Sigma^+(X\sigma\sigma^{-1})$ to produce this latter condition, while also imposing the restriction that the fitted molecular constants recovered the experimentally determined term energy for $b^3\Sigma^+(X\sigma\sigma^{-1})$ v = 1. The constants $T_0 = 9489$, $x_e = 590.4$, $x_ex_e = 3$ cm^{-1} satisfied these conditions. The $A'^1\Pi(X\sigma\pi^{-1}) - b^3\Sigma^+(X\sigma\sigma^{-1})$ Franck-Condon factors were then calculated using the program LEVEL 8.0 [121], and the unsigned overlap integrals were obtained as the square roots of the Franck-Condon factors. This procedure yielded $|\langle v' = 17|v = 14\rangle| = 0.054$ and a spin-orbit matrix element of $H_{SO} = 4.6$ cm^{-1}. Unperturbed rotational constants were predicted to be $B_{17} = 0.300$ cm^{-1} for $A'^1\Pi(X\sigma\pi^{-1})$ and B14 = 0.344 cm^{-1} for $b^3\Sigma^+(X\sigma\sigma^{-1})$). With an energy gap of 12 cm^{-1} between the J = 0 levels of the unperturbed $A'^1\Pi(X\sigma\pi^{-1})$ v = 17 and $b^3\Sigma^+(X\sigma\sigma^{-1})$) v = 14 states, a two-state perturbation model recovered the experimental value for the effective rotational constant for low rotational levels of $A'^1\Pi(X\sigma\pi^{-1})$ v = 17. The model indicated that the band origin had been pushed down by 1.6 cm^{-1}. As part of this exercise, we also examined the $A'^1\Pi(X\sigma\pi^{-1})$ v = 16/ $b^3\Sigma^+(X\sigma\sigma^{-1})$ v = 13 pair to assess the degree to which they interact. In this case the $b^3\Sigma^+(X\sigma\sigma^{-1})$ v = 13 state is estimated to lie 30 cm^{-1} below $A'^1\Pi(X\sigma\sigma^{-1})$ v = 16. Due to this larger energy gap, and the small overlap integral 0 ($|\langle v' = 16|v = 13\rangle| = 0.0046$), we found this interaction to be unimportant for the resolution of the present experiments. Overall, this analysis supports the assignment of the $A'^1\Pi(X\sigma\pi^{-1})$ v = 17 state perturbation to the interaction with $b^3\Sigma^+(X\sigma\sigma^{-1})$ v = 14.

Fluorescence decay lifetimes for the $A'^1\Pi(X\sigma\pi^{-1})$ state were found to be almost independent of the vibrational level over the range v = 10–17. Field [103] had noted that the $A'^1\Pi(X\sigma\pi^{-1}) - X^1\Sigma^+$ transition dipole moment would be small, resulting in spontaneous decay lifetimes on the order of 10 μs. The observed values are somewhat shorter, but consistent with the argument presented in Ref. [103]. As the ExoMol database [112] also includes the Einstein A coefficients, it was possible to generate theoretical values for the lifetime of the $A'^1\Pi(X\sigma\pi^{-1})$ state by summing the A coefficients over all final states. This yielded lifetimes that decreased from 11.4 μs for v = 10 down to 8.5 μs for v = 15. The predicted lifetime for v = 17 was anomalous, being 15.4 μs. This suggests that the calculated Einstein A coefficients for A' v = 17 have been decreased by the effects of mixing with a long-lived state (a prediction that is not supported by the present lifetime measurements).

DLIF and lifetime measurements for the $C^1\Sigma^+(B\sigma\sigma^{-1})$ and $\gamma 0^+$ states provide useful insights for establishing the configurational parentage of the $\gamma 0^+$ state. We begin by considering the DLIF spectra for the $C^1\Sigma^+(B\sigma\sigma^{-1})$ v = 6 and $\gamma 0^+$ n – 1 levels. The energy separation between these levels is large enough (59.4 cm^{-1}) that mixing between them is expected to be weak. The relevant traces in Figure 5.3 show that $C^1\Sigma^+(B\sigma\sigma^{-1})$ v = 6 radiates back to both the $X^1\Sigma^+$ and $A^1\Sigma^+(X\sigma\sigma^{-1}$ states, as expected. A transition to $a^3\Pi(0^+)(X\sigma\sigma^{-1})$ v = 11 is also present. This is probably mediated by the mixing of this lower level with nearby levels of the $X^1\Sigma^+$ and $A^1\Sigma^+(X\sigma\sigma^{-1})$ states (see Fig. 7 of reference [109]). In contrast, the DLIF spectrum obtained using excitation of $\gamma 0^+$ n – 1 is dominated by transitions to the $a^3\Pi(0^+)(X\sigma\pi^{-1})$ state v = 10 and 11 level. The transitions to singlet lower states are barely discernible above the noise level. This clearly indicates that the $\gamma 0^+$ state is a triplet state. Furthermore, the short radiative lifetime of $\gamma 0^+$ n – 1 indicates that the $\gamma 0^+ - a^3\Pi(0^+)(X\sigma\pi^{-1})$ transition has a large transition dipole moment. Similar trends are evident for the $C^1\Sigma^+(B\sigma\sigma^{-1})$ v = 8/$\gamma 0^+$ v = n + 1 pair of states, which are separated by 52.3 cm^{-1}. The emission from $\gamma 0^+$ n + 1 is dominated by the triplet bands, but, as compared to the spectrum from the n−1 level, the singlet bands are somewhat stronger. This suggests that the n + 1 state has a small fractional singlet character. The emission from the $C^1\Sigma^+(B\sigma\sigma^{-1})$ v = 8 level was dominated by transitions to singlet final states.

Next, we consider the $C^1\Sigma^+(B\sigma\sigma^{-1})$ v=7 /$\gamma 0^+$ n pair of states. The perturbation analysis presented in Ref. [116] concluded that these states were separated by 9.4 cm^{-1} prior to their mutual repulsion. The eigenvectors from the deperturbation analysis indicated a nearly 50:50 mixing of the two states. This prediction was borne out by the DLIF spectra that show both singlet and triplet bands with comparable intensities. Note also that the lifetime behavior is consistent. The results for $C^1\Sigma^+(B\sigma\sigma^{-1})$ v = 6 and 8 give an average lifetime of 27 ns, and those for $\gamma 0^+$ n – 1 and n + 1 give a lifetime of 44 ns. Hence a 50:50 mixed state, in the absence of interference effects, should exhibit a lifetime of 33 ns (based on the weighted sum of decay rates). This is the average of the values observed for $C^1\Sigma^+(B\sigma\sigma^{-1})$ v = 7 and $\gamma 0^+$ n.

Having established that the $\gamma 0^+$ state derives from 3 triplet state, the next step was to determine the identity of the state. This process was guided by the observations that $\gamma 0^+$ perturbs $C^1\Sigma^+(B\sigma\sigma^{-1})$ and radiates to $a^3\Pi(0^+)(X\sigma\pi^{-1})$. Viable candidates for the perturbing state are $g^3\Pi(0^+)(B\sigma\pi^{-1})$ and $f^3\Pi(0^+)(A\pi\sigma^{-1})$. Of these two, $g^3\Pi(0^+)(B\sigma\pi^{-1})$ can radiate to $a^3\Pi(0^+)(X\sigma\pi^{-1})$ via a one-electron process while the transition from $f^3\Pi(0^+)(A\pi\sigma^{-1})$ would require a two-electron process. Based on these considerations, and the indication from the vibrational intervals that $\gamma 0^+$ is derived from a π^{-1} configuration, we recommend the assignment of the $\gamma 0^+$ state as $g^3\Pi(0^+)(B\sigma\pi^{-1})$. Finally, we speculate on the vibrational numbering for the observed levels of the $g^3\Pi(0^+)(B\sigma\pi^{-1})$ state. This state has not been characterized previously, but the term energy of the v = 0 level can be estimated by considering the singlet-triplet energy splittings associated with the π^{-1} states. The $B\sigma\pi^{-1}$ configuration also gives rise to the $F^1\Pi$ state, for which the term energy and vibrational constants have been determined (T_{00} = 26794.5, x_e = 521.3, $x_e x_e$ = 2.59 cm^{-1}) [116]. Representative isoconfigurational singlet-triplet energy splittings are provided by $\Delta E(A'^1\Pi - a^3\Pi(1), X\sigma\pi^{-1}) = 257\ cm^{-1}$, $\Delta E(D^1\Delta - d^3\Delta(2), A\pi\pi^{-1}) = –210\ cm^{-1}$, and $\Delta E(E^1\Sigma^- - e^3\Sigma^-, A\pi\pi^{-1}) = –53\ cm^{-1}$ [97]. If we assume that the vibrational constants are the same for the $g^3\Pi(0^+)(B\sigma\pi^{-1})$ and $F^1\Pi(B\sigma\pi^{-1})$ states, we can use the vibrational interval between the v = n + 1 and v = n – 1 states to obtain the energy of the n = 12 level. Extrapolation to v = 0 then yields a term energy for the $g^3\Pi(0^+), (B\sigma\pi^{-1})$ state of $T_{00} = 26,644$ cm^{-1}, and a singlet-triplet energy splitting of $\Delta E(F^1\Pi–g^3(0^+), B\sigma\pi^{-1}),$ = 151 cm^{-1}. The vibrational numbering n = 11 and n = 13 would yield unlikely values for $\Delta E(F^1\Pi$ - $g^3\Pi(0^+)(B\sigma\pi^{-1})$. Overall, this analysis shows that the assignment of $\gamma 0^+$ as the $(g^3\Pi(0^+)(B\sigma\pi^{-1})$ state is entirely consistent with the atomic-ions-in-molecule model for CaO.

5.6 Acknowledgement

This material is based upon work supported by the National Science Foundation under 1946950. RWF thanks the NSF (CHE-1800410) for support of his part of this collaboration.

5.7 Supporting Information

Supporting information for the data presented in this chapter can be found in Appendix A.

Appendix A

Appendix A: Linelists for CaO

This section contains all of the found lines for the $A'^1\Pi^+ - X^1\Sigma^+$ transitions. All of the lower terms of the transitions are V = 0, and upper states from V = 10 − 17 are provided. The tables in the section were all generated by PGOPHER [62]. Wavelength calibration was achieved through comparison to a coincident I_2 LIF spectrum, and matching those emissions to an I_2 *B*-*X* excitation spectrum atlas [120] .

Table A.1: Assignments for the $\mathrm{A}'^1\Pi(\mathrm{X}\sigma\pi^{-1})$ $(\mathrm{v}' = 10, \mathrm{v}'' = 0)$ band.

J’	S’	J”	S”	Obs	Calc	Obs-Calc	Assignment	v’	v”
4	e	3	e	13788.184	13788.2142	-0.0302	R(3)	10	0
3	e	2	e	13788.184	13788.3332	-0.1492	R(2)	10	0
2	e	1	e	13788.184	13788.2012	-0.0172	R(1)	10	0
5	e	4	e	13787.83	13787.8439	-0.0139	R(4)	10	0
1	e	0	e	13787.83	13787.8179	0.0121	R(0)	10	0
6	e	5	e	13787.178	13787.2225	-0.0445	R(5)	10	0
7	e	6	e	13786.322	13786.3499	-0.0279	R(6)	10	0
2	f	2	e	13786.322	13786.43	-0.108	Q(2)	10	0
3	f	3	e	13785.64	13785.6764	-0.0364	Q(3)	10	0
8	e	7	e	13785.172	13785.2261	-0.0541	R(7)	10	0
4	f	4	e	13784.649	13784.6718	-0.0228	Q(4)	10	0
9	e	8	e	13783.756	13783.8511	-0.0951	R(8)	10	0
2	e	3	e	13783.756	13783.7732	-0.0172	P(3)	10	0
5	f	5	e	13783.427	13783.4159	0.0111	Q(5)	10	0
6	f	6	e	13781.912	13781.9089	0.0031	Q(6)	10	0
10	e	9	e	13782.15	13782.225	-0.075	R(9)	10	0
3	e	4	e	13782.15	13782.134	0.016	P(4)	10	0
7	f	7	e	13780.204	13780.1507	0.0533	Q(7)	10	0
11	e	10	e	13780.204	13780.3477	-0.1437	R(10)	10	0
4	e	5	e	13780.204	13780.2438	-0.0398	P(5)	10	0
8	f	8	e	13778.169	13778.1413	0.0277	Q(8)	10	0
5	e	6	e	13778.169	13778.1023	0.0667	P(6)	10	0
12	e	11	e	13778.169	13778.2192	-0.0502	R(11)	10	0
9	f	9	e	13775.848	13775.8807	-0.0327	Q(9)	10	0
6	e	7	e	13775.848	13775.7097	0.1383	P(7)	10	0
13	e	12	e	13775.848	13775.8396	0.0084	R(12)	10	0
10	f	10	e	13773.24	13773.369	-0.129	Q(10)	10	0
7	e	8	e	13773.24	13773.0659	0.1741	P(8)	10	0
14	e	13	e	13773.24	13773.2088	0.0312	R(13)	10	0
11	f	11	e	13770.674	13770.6061	0.0679	Q(11)	10	0
15	e	14	e	13770.674	13770.3268	0.3472	R(14)	10	0
8	e	9	e	13770.297	13770.1709	0.1261	P(9)	10	0
12	f	12	e	13767.631	13767.592	0.039	Q(12)	10	0
9	e	10	e	13767.161	13767.0247	0.1363	P(10)	10	0
16	e	15	e	13767.161	13767.1937	-0.0327	R(15)	10	0
13	f	13	e	13764.41	13764.3268	0.0832	Q(13)	10	0
10	e	11	e	13763.744	13763.6274	0.1166	P(11)	10	0
17	e	16	e	13763.744	13763.8093	-0.0653	R(16)	10	0
14	f	14	e	13760.878	13760.8104	0.0676	Q(14)	10	0
11	e	12	e	13760.115	13759.9789	0.1361	P(12)	10	0
18	e	17	e	13760.115	13760.1738	-0.0588	R(17)	10	0
15	f	15	e	13757.087	13757.0428	0.0442	Q(15)	10	0
12	e	13	e	13756.153	13756.0792	0.0738	P(13)	10	0
19	e	18	e	13756.153	13756.2872	-0.1342	R(18)	10	0
16	f	16	e	13753.102	13753.0241	0.0779	Q(16)	10	0
13	e	14	e	13751.977	13751.9284	0.0486	P(14)	10	0
20	e	19	e	13751.977	13752.1493	-0.1723	R(19)	10	0
17	f	17	e	13748.776	13748.7541	0.0219	Q(17)	10	0
14	e	15	e	13747.601	13747.5264	0.0746	P(15)	10	0
18	f	18	e	13744.156	13744.233	-0.077	Q(18)	10	0
15	e	16	e	13742.874	13742.8732	0.0008	P(16)	10	0
19	f	19	e	13739.482	13739.4608	0.0212	Q(19)	10	0
16	e	17	e	13737.967	13737.9689	-0.0019	P(17)	10	0
20	f	20	e	13734.559	13734.4373	0.1217	Q(20)	10	0
17	e	18	e	13732.851	13732.8133	0.0377	P(18)	10	0
23	f	23	e	13717.846	13717.86	-0.014	Q(23)	10	0
20	e	21	e	13715.896	13715.8397	0.0563	P(21)	10	0
21	e	22	e	13709.726	13709.6795	0.0465	P(22)	10	0

Table A.2: Assignments for the $\mathrm{A}'^1\Pi(\mathrm{X}\sigma\pi^{-1})$ ($\mathrm{v}' = 11, \mathrm{v}'' = 0$) band.

J'	S'	J"	S"	Observed	Calculated	Obs-Calc	Assignment	v'	v"
4	e	3	e	14277.949	14277.9208	0.0282	R(3)	11	0
3	e	2	e	14277.945	14278.059	-0.114	R(2)	11	0
2	e	1	e	14277.945	14277.9412	0.0038	R(1)	11	0
5	e	4	e	14277.54	14277.5267	0.0133	R(4)	11	0
1	e	0	e	14277.521	14277.5674	-0.0464	R(0)	11	0
6	e	5	e	14276.849	14276.8766	-0.0276	R(5)	11	0
1	f	1	e	14276.828	14276.6818	0.1462	Q(1)	11	0
7	e	6	e	14276.013	14275.9705	0.0425	R(6)	11	0
2	f	2	e	14276.014	14276.17	-0.156	Q(2)	11	0
3	f	3	e	14275.391	14275.4022	-0.0112	Q(3)	11	0
8	e	7	e	14274.884	14274.8083	0.0757	R(7)	11	0
4	f	4	e	14274.456	14274.3784	0.0776	Q(4)	11	0
9	e	8	e	14273.458	14273.39	0.068	R(8)	11	0
2	e	3	e	14273.438	14273.5132	-0.0752	P(3)	11	0
5	f	5	e	14273.135	14273.0987	0.0363	Q(5)	11	0
6	f	6	e	14271.679	14271.563	0.116	Q(6)	11	0
10	e	9	e	14271.683	14271.7156	-0.0326	R(9)	11	0
7	f	7	e	14269.797	14269.7713	0.0257	Q(7)	11	0
11	e	10	e	14269.798	14269.7851	0.0129	R(10)	11	0
4	e	5	e	14269.798	14269.9504	-0.1524	P(5)	11	0
8	f	8	e	14267.77	14267.7235	0.0465	Q(8)	11	0
12	e	11	e	14267.767	14267.5983	0.1687	R(11)	11	0
5	e	6	e	14267.767	14267.7851	-0.0181	P(6)	11	0
9	f	9	e	14265.434	14265.4196	0.0144	Q(9)	11	0
6	e	7	e	14265.435	14265.3638	0.0712	P(7)	11	0
13	e	12	e	14265.182	14265.1553	0.0267	R(12)	11	0
10	f	10	e	14262.818	14262.8596	-0.0416	Q(10)	11	0
14	e	13	e	14262.461	14262.4559	0.0051	R(13)	11	0
11	f	11	e	14260.07	14260.0435	0.0265	Q(11)	11	0
8	e	9	e	14259.759	14259.7531	0.0059	P(9)	11	0
15	e	14	e	14259.495	14259.5002	-0.0052	R(14)	11	0
12	f	12	e	14256.975	14256.9711	0.0039	Q(12)	11	0
9	e	10	e	14256.531	14256.5636	-0.0326	P(10)	11	0
16	e	15	e	14256.29	14256.288	0.002	R(15)	11	0
13	f	13	e	14253.64	14253.6425	-0.0025	Q(13)	11	0
10	e	11	e	14253.098	14253.118	-0.02	P(11)	11	0
17	e	16	e	14252.741	14252.8193	-0.0783	R(16)	11	0
14	f	14	e	14249.999	14250.0575	-0.0585	Q(14)	11	0
11	e	12	e	14249.362	14249.4163	-0.0543	P(12)	11	0
18	e	17	e	14249.013	14249.094	-0.081	R(17)	11	0
15	f	15	e	14246.166	14246.2162	-0.0502	Q(15)	11	0
12	e	13	e	14245.395	14245.4583	-0.0633	P(13)	11	0
19	e	18	e	14245.005	14245.112	-0.107	R(18)	11	0
16	f	16	e	14242.089	14242.1184	-0.0294	Q(16)	11	0
13	e	14	e	14241.2	14241.2441	-0.0441	P(14)	11	0
20	e	19	e	14240.805	14240.8732	-0.0682	R(19)	11	0
17	f	17	e	14237.773	14237.7641	0.0089	Q(17)	11	0
14	e	15	e	14236.763	14236.7735	-0.0105	P(15)	11	0
21	e	20	e	14236.383	14236.3777	0.0053	R(20)	11	0
18	f	18	e	14233.17	14233.1532	0.0168	Q(18)	11	0
15	e	16	e	14232.082	14232.0466	0.0354	P(16)	11	0
22	e	21	e	14231.629	14231.6252	0.0038	R(21)	11	0
19	f	19	e	14228.359	14228.2856	0.0734	Q(19)	11	0
16	e	17	e	14227.086	14227.0632	0.0228	P(17)	11	0
23	e	22	e	14226.575	14226.6156	-0.0406	R(22)	11	0
20	f	20	e	14223.281	14223.1612	0.1198	Q(20)	11	0
17	e	18	e	14221.875	14221.8233	0.0517	P(18)	11	0
21	f	21	e	14217.848	14217.7801	0.0679	Q(21)	11	0
18	e	19	e	14216.346	14216.3268	0.0192	P(19)	11	0
25	e	24	e	14215.795	14215.825	-0.03	R(24)	11	0
22	f	22	e	14212.15	14212.142	0.008	Q(22)	11	0
20	e	21	e	14204.511	14204.5636	-0.0526	P(21)	11	0
23	f	23	e	14206.201	14206.2468	-0.0458	Q(23)	11	0
24	f	24	e	14200.112	14200.0945	0.0175	Q(24)	11	0
21	e	22	e	14198.271	14198.2969	-0.0259	P(22)	11	0
25	f	25	e	14193.723	14193.685	0.038	Q(25)	11	0
22	e	23	e	14191.842	14191.7732	0.0688	P(23)	11	0

Table A.3: Assignments for the $\mathrm{A'^1\Pi(X\sigma\pi^{-1})}$ ($\mathrm{v'} = 12, \mathrm{v''} = 0$) band.

J’	S’	J”	S”	Obs	Calc	Obs-Calc		v’	v”
4	e	3	e	14762.387	14762.3341	0.0529	R(3)	12	0
3	e	2	e	14762.387	14762.494	-0.107	R(2)	12	0
2	e	1	e	14762.387	14762.3926	-0.0056	R(1)	12	0
5	e	4	e	14761.955	14761.9128	0.0422	R(4)	12	0
1	e	0	e	14761.955	14762.0298	-0.0748	R(0)	12	0
6	e	5	e	14761.257	14761.2302	0.0268	R(5)	12	0
1	f	1	e	14761.257	14761.1442	0.1128	Q(1)	12	0
2	f	2	e	14760.677	14760.6214	0.0556	Q(2)	12	0
7	e	6	e	14760.346	14760.2864	0.0596	R(6)	12	0
3	f	3	e	14759.882	14759.8372	0.0448	Q(3)	12	0
8	e	7	e	14759.139	14759.0813	0.0577	R(7)	12	0
4	f	4	e	14758.842	14758.7917	0.0503	Q(4)	12	0
2	e	3	e	14758.033	14757.9646	0.0684	P(3)	12	0
5	f	5	e	14757.568	14757.4848	0.0832	Q(5)	12	0
3	e	4	e	14756.301	14756.2948	0.0062	P(4)	12	0
6	f	6	e	14755.907	14755.9166	-0.0096	Q(6)	12	0
10	e	9	e	14755.907	14755.8875	0.0195	R(9)	12	0
7	f	7	e	14754.027	14754.0872	-0.0602	Q(7)	12	0
11	e	10	e	14754.027	14753.8989	0.1281	R(10)	12	0
8	f	8	e	14752.016	14751.9965	0.0195	Q(8)	12	0
5	e	6	e	14752.016	14752.1712	-0.1552	P(6)	12	0
12	e	11	e	14751.646	14751.6494	-0.0034	R(11)	12	0
9	f	9	e	14749.619	14749.6446	-0.0256	Q(9)	12	0
6	e	7	e	14749.619	14749.7174	-0.0984	P(7)	12	0
13	e	12	e	14749.079	14749.1388	-0.0598	R(12)	12	0
10	f	10	e	14746.992	14747.0315	-0.0395	Q(10)	12	0
7	e	8	e	14746.992	14747.0024	-0.0104	P(8)	12	0
14	e	13	e	14746.316	14746.3674	-0.0514	R(13)	12	0
11	f	11	e	14744.048	14744.1573	-0.1093	Q(11)	12	0
8	e	9	e	14744.048	14744.0261	0.0219	P(9)	12	0
15	e	14	e	14743.248	14743.3351	-0.0871	R(14)	12	0
12	f	12	e	14740.96	14741.0222	-0.0622	Q(12)	12	0
9	e	10	e	14740.747	14740.7886	-0.0416	P(10)	12	0
16	e	15	e	14739.983	14740.0421	-0.0591	R(15)	12	0
13	f	13	e	14737.59	14737.626	-0.036	Q(13)	12	0
10	e	11	e	14737.219	14737.2899	-0.0709	P(11)	12	0
17	e	16	e	14736.414	14736.4885	-0.0745	R(16)	12	0
14	f	14	e	14733.958	14733.969	-0.011	Q(14)	12	0
11	e	12	e	14733.514	14733.5301	-0.0161	P(12)	12	0
18	e	17	e	14732.676	14732.6743	0.0017	R(17)	12	0
15	f	15	e	14730.075	14730.0511	0.0239	Q(15)	12	0
12	e	13	e	14729.495	14729.5094	-0.0144	P(13)	12	0
19	e	18	e	14728.604	14728.5997	0.0043	R(18)	12	0
16	f	16	e	14725.97	14725.8725	0.0975	Q(16)	12	0
13	e	14	e	14725.296	14725.2276	0.0684	P(14)	12	0
20	e	19	e	14724.315	14724.2647	0.0503	R(19)	12	0
17	f	17	e	14721.502	14721.4333	0.0687	Q(17)	12	0
14	e	15	e	14720.742	14720.685	0.057	P(15)	12	0
21	e	20	e	14719.712	14719.6694	0.0426	R(20)	12	0
18	f	18	e	14716.788	14716.7335	0.0545	Q(18)	12	0
15	e	16	e	14715.9	14715.8815	0.0185	P(16)	12	0
22	e	21	e	14714.82	14714.8141	0.0059	R(21)	12	0
19	f	19	e	14711.827	14711.7733	0.0537	Q(19)	12	0
16	e	17	e	14710.83	14710.8173	0.0127	P(17)	12	0
23	e	22	e	14709.66	14709.6987	-0.0387	R(22)	12	0
20	f	20	e	14706.539	14706.5527	-0.0137	Q(20)	12	0
17	e	18	e	14705.474	14705.4925	-0.0185	P(18)	12	0
24	e	23	e	14704.247	14704.3235	-0.0765	R(23)	12	0
21	f	21	e	14701.056	14701.0718	-0.0158	Q(21)	12	0
18	e	19	e	14699.842	14699.9071	-0.0651	P(19)	12	0
25	e	24	e	14698.627	14698.6885	-0.0615	R(24)	12	0
22	f	22	e	14695.304	14695.3309	-0.0269	Q(22)	12	0
19	e	20	e	14694.019	14694.0613	-0.0423	P(20)	12	0
26	e	25	e	14692.694	14692.794	-0.1	R(25)	12	0
23	f	23	e	14689.361	14689.3299	0.0311	Q(23)	12	0
20	e	21	e	14687.958	14687.9551	0.0029	P(21)	12	0
24	f	24	e	14683.136	14683.0691	0.0669	Q(24)	12	0
21	e	22	e	14681.64	14681.5886	0.0514	P(22)	12	0
25	f	25	e	14676.673	14676.5485	0.1245	Q(25)	12	0
22	e	23	e	14675.018	14674.9621	0.0559	P(23)	12	0

Table A.4: Assignments for the $A'^1\Pi(X\sigma\pi^{-1})$ ($v' = 13, v'' = 0$) band.

J’	S’	J”	S”	Obs	Calc	Obs-Calc	Assignment	v’	v”
4	e	3	e	15241.603	15241.4358	0.1672	R(3)	13	0
2	e	1	e	15241.603	15241.5215	0.0815	R(1)	13	0
5	e	4	e	15241.081	15240.995	0.086	R(4)	13	0
6	e	5	e	15240.327	15240.2889	0.0381	R(5)	13	0
1	f	1	e	15240.327	15240.2808	0.0462	Q(1)	13	0
2	f	2	e	15239.7	15239.7503	-0.0503	Q(2)	13	0
7	e	6	e	15239.325	15239.3173	0.0077	R(6)	13	0
3	f	3	e	15238.924	15238.9545	-0.0305	Q(3)	13	0
5	f	5	e	15236.576	15236.567	0.009	Q(5)	13	0
9	e	8	e	15236.576	15236.5775	-0.0015	R(8)	13	0
6	f	6	e	15234.915	15234.9753	-0.0603	Q(6)	13	0
10	e	9	e	15234.915	15234.8092	0.1058	R(9)	13	0
7	f	7	e	15233.081	15233.1181	-0.0371	Q(7)	13	0
4	e	5	e	15233.428	15233.4654	-0.0374	P(5)	13	0
11	e	10	e	15232.663	15232.7752	-0.1122	R(10)	13	0
8	f	8	e	15230.925	15230.9954	-0.0704	Q(8)	13	0
12	e	11	e	15230.397	15230.4754	-0.0784	R(11)	13	0
9	f	9	e	15228.642	15228.6071	0.0349	Q(9)	13	0
6	e	7	e	15228.642	15228.7761	-0.1341	P(7)	13	0
13	e	12	e	15227.867	15227.9096	-0.0426	R(12)	13	0
10	f	10	e	15225.875	15225.9532	-0.0782	Q(10)	13	0
7	e	8	e	15225.875	15226.0333	-0.1583	P(8)	13	0
14	e	13	e	15224.949	15225.0778	-0.1288	R(13)	13	0
11	f	11	e	15222.988	15223.0336	-0.0456	Q(11)	13	0
8	e	9	e	15222.988	15223.025	-0.037	P(9)	13	0
15	e	14	e	15221.925	15221.9799	-0.0549	R(14)	13	0
12	f	12	e	15219.817	15219.8482	-0.0312	Q(12)	13	0
9	e	10	e	15219.817	15219.7511	0.0659	P(10)	13	0
16	e	15	e	15218.588	15218.6157	-0.0277	R(15)	13	0
13	f	13	e	15216.317	15216.3968	-0.0798	Q(13)	13	0
10	e	11	e	15216.317	15216.2116	0.1054	P(11)	13	0
17	e	16	e	15214.976	15214.985	-0.009	R(16)	13	0
14	f	14	e	15212.734	15212.6794	0.0546	Q(14)	13	0
18	e	17	e	15211.105	15211.0878	0.0172	R(17)	13	0
15	f	15	e	15208.746	15208.6959	0.0501	Q(15)	13	0
12	e	13	e	15208.436	15208.3354	0.1006	P(13)	13	0
19	e	18	e	15206.993	15206.9238	0.0692	R(18)	13	0
16	f	16	e	15204.494	15204.4461	0.0479	Q(16)	13	0
13	e	14	e	15204.088	15203.9984	0.0896	P(14)	13	0
20	e	19	e	15202.518	15202.4929	0.0251	R(19)	13	0
17	f	17	e	15200	15199.9298	0.0702	Q(17)	13	0
14	e	15	e	15199.49	15199.3954	0.0946	P(15)	13	0
21	e	20	e	15197.84	15197.795	0.045	R(20)	13	0
18	f	18	e	15195.14	15195.147	-0.007	Q(18)	13	0
15	e	16	e	15194.532	15194.5263	0.0057	P(16)	13	0
22	e	21	e	15192.833	15192.8298	0.0032	R(21)	13	0
19	f	19	e	15190.091	15190.0974	-0.0064	Q(19)	13	0
16	e	17	e	15189.33	15189.3909	-0.0609	P(17)	13	0
23	e	22	e	15187.533	15187.5972	-0.0642	R(22)	13	0
20	f	20	e	15184.768	15184.7809	-0.0129	Q(20)	13	0
17	e	18	e	15183.997	15183.989	0.008	P(18)	13	0
24	e	23	e	15182.005	15182.0969	-0.0919	R(23)	13	0
21	f	21	e	15179.174	15179.1974	-0.0234	Q(21)	13	0
18	e	19	e	15178.301	15178.3206	-0.0196	P(19)	13	0
25	e	24	e	15176.275	15176.3288	-0.0538	R(24)	13	0
22	f	22	e	15173.376	15173.3466	0.0294	Q(22)	13	0
19	e	20	e	15172.406	15172.3854	0.0206	P(20)	13	0
26	e	25	e	15170.341	15170.2926	0.0484	R(25)	13	0
23	f	23	e	15167.308	15167.2284	0.0796	Q(23)	13	0
4	f	4	e	15238.006	15237.8934	0.1126	Q(4)	13	0
8	e	7	e	15238.006	15238.0802	-0.0742	R(7)	13	0

Table A.5: Assignments for the $\mathrm{A}'^{1}\Pi(\mathrm{X}\sigma\pi^{-1})$ $(\mathrm{v}' = 14, \mathrm{v}'' = 0)$ band.

J’	S’	J”	S”	Obs	Calc	Obs-Calc	Assignment	v’	v”
4	e	3	e	15715.752	15715.5568	0.1952	R(3)	14	0
3	e	2	e	15715.752	15715.7549	-0.0029	R(2)	14	0
2	e	1	e	15715.752	15715.6822	0.0698	R(1)	14	0
5	e	4	e	15715.201	15715.0876	0.1134	R(4)	14	0
1	e	0	e	15715.201	15715.3384	-0.1374	R(0)	14	0
6	e	5	e	15714.427	15714.3476	0.0794	R(5)	14	0
1	f	1	e	15714.427	15714.4528	-0.0258	Q(1)	14	0
2	f	2	e	15713.957	15713.911	0.046	Q(2)	14	0
7	e	6	e	15713.38	15713.3366	0.0434	R(6)	14	0
3	f	3	e	15713.24	15713.0981	0.1419	Q(3)	14	0
4	f	4	e	15712.106	15712.0144	0.0916	Q(4)	14	0
8	e	7	e	15712.106	15712.0547	0.0513	R(7)	14	0
2	e	3	e	15711.307	15711.2542	0.0528	P(3)	14	0
5	f	5	e	15710.612	15710.6596	-0.0476	Q(5)	14	0
9	e	8	e	15710.612	15710.5018	0.1102	R(8)	14	0
3	e	4	e	15709.53	15709.5557	-0.0257	P(4)	14	0
6	f	6	e	15709.049	15709.034	0.015	Q(6)	14	0
10	e	9	e	15708.654	15708.6779	-0.0239	R(9)	14	0
7	f	7	e	15707.105	15707.1374	-0.0324	Q(7)	14	0
11	e	10	e	15706.477	15706.5832	-0.1062	R(10)	14	0
8	f	8	e	15704.966	15704.9699	-0.0039	Q(8)	14	0
12	e	11	e	15704.117	15704.2175	-0.1005	R(11)	14	0
5	e	6	e	15705.24	15705.346	-0.106	P(6)	14	0
9	f	9	e	15702.479	15702.5314	-0.0524	Q(9)	14	0
13	e	12	e	15701.416	15701.5808	-0.1648	R(12)	14	0
10	f	10	e	15699.769	15699.8219	-0.0529	Q(10)	14	0
7	e	8	e	15699.769	15700.0526	-0.2836	P(8)	14	0
14	e	13	e	15698.501	15698.6732	-0.1722	R(13)	14	0
11	f	11	e	15696.822	15696.8416	-0.0196	Q(11)	14	0
8	e	9	e	15696.822	15696.9995	-0.1775	P(9)	14	0
15	e	14	e	15695.341	15695.4947	-0.1537	R(14)	14	0
12	f	12	e	15693.539	15693.5903	-0.0513	Q(12)	14	0
9	e	10	e	15693.539	15693.6754	-0.1364	P(10)	14	0
16	e	15	e	15691.889	15692.0452	-0.1562	R(15)	14	0
13	f	13	e	15690.046	15690.068	-0.022	Q(13)	14	0
10	e	11	e	15690.046	15690.0803	-0.0343	P(11)	14	0
17	e	16	e	15688.296	15688.3248	-0.0288	R(16)	14	0
14	f	14	e	15686.297	15686.2748	0.0222	Q(14)	14	0
11	e	12	e	15686.297	15686.2144	0.0826	P(12)	14	0
18	e	17	e	15684.309	15684.3334	-0.0244	R(17)	14	0
15	f	15	e	15682.256	15682.2107	0.0453	Q(15)	14	0
12	e	13	e	15682.256	15682.0775	0.1785	P(13)	14	0
19	e	18	e	15680.143	15680.0711	0.0719	R(18)	14	0
16	f	16	e	15677.987	15677.8756	0.1114	Q(16)	14	0
13	e	14	e	15677.716	15677.6696	0.0464	P(14)	14	0
20	e	19	e	15675.545	15675.5378	0.0072	R(19)	14	0
17	f	17	e	15673.465	15673.2696	0.1954	Q(17)	14	0
14	e	15	e	15673.149	15672.9908	0.1582	P(15)	14	0
21	e	20	e	15670.83	15670.7336	0.0964	R(20)	14	0
18	f	18	e	15668.518	15668.3926	0.1254	Q(18)	14	0
15	e	16	e	15668.175	15668.0411	0.1339	P(16)	14	0
22	e	21	e	15665.692	15665.6585	0.0335	R(21)	14	0
19	f	19	e	15663.344	15663.2447	0.0993	Q(19)	14	0
16	e	17	e	15662.879	15662.8204	0.0586	P(17)	14	0
23	e	22	e	15660.204	15660.3124	-0.1084	R(22)	14	0
20	f	20	e	15657.887	15657.8258	0.0612	Q(20)	14	0
17	e	18	e	15657.301	15657.3288	-0.0278	P(18)	14	0
21	f	21	e	15652.06	15652.136	-0.076	Q(21)	14	0
18	e	19	e	15651.446	15651.5662	-0.1202	P(19)	14	0
25	e	24	e	15648.718	15648.8074	-0.0894	R(24)	14	0
22	f	22	e	15646.139	15646.1753	-0.0363	Q(22)	14	0
19	e	20	e	15645.426	15645.5327	-0.1067	P(20)	14	0
23	f	23	e	15640.017	15639.9436	0.0734	Q(23)	14	0
20	e	21	e	15639.224	15639.2282	-0.0042	P(21)	14	0
27	e	26	e	15636.175	15636.2187	-0.0437	R(26)	14	0
24	f	24	e	15633.541	15633.441	0.1	Q(24)	14	0
21	e	22	e	15632.698	15632.6528	0.0452	P(22)	14	0
25	f	25	e	15626.829	15626.6674	0.1616	Q(25)	14	0
22	e	23	e	15625.84	15625.8065	0.0335	P(23)	14	0
26	f	26	e	15619.711	15619.6229	0.0881	Q(26)	14	0
23	e	24	e	15618.676	15618.6892	-0.0132	P(24)	14	0
27	f	27	e	15612.321	15612.3075	0.0135	Q(27)	14	0
24	e	25	e	15611.256	15611.301	-0.045	P(25)	14	0
28	f	28	e	15604.592	15604.7211	-0.1291	Q(28)	14	0
25	e	26	e	15603.531	15603.6418	-0.1108	P(26)	14	0

Table A.6: Assignments for the $\mathrm{A}'^1\Pi(\mathrm{X}\sigma\pi^{-1})$ $(\mathrm{v}' = 15, \mathrm{v}'' = 0)$ band.

J’	S’	J”	S”	Observed	Calculated	Obs-Calc	Assignment	v’	v”
4	e	3	e	16184.98	16184.8437	0.1363	R(3)	15	0
3	e	2	e	16184.98	16185.0686	-0.0886	R(2)	15	0
2	e	1	e	16184.98	16185.0159	-0.0359	R(1)	15	0
5	e	4	e	16184.344	16184.3412	0.0028	R(4)	15	0
6	e	5	e	16183.579	16183.5611	0.0179	R(5)	15	0
1	f	1	e	16183.579	16183.7999	-0.2209	Q(1)	15	0
2	f	2	e	16183.281	16183.2447	0.0363	Q(2)	15	0
7	e	6	e	16182.457	16182.5033	-0.0463	R(6)	15	0
1	e	2	e	16182.092	16182.0287	0.0633	P(2)	15	0
4	f	4	e	16181.213	16181.3013	-0.0883	Q(4)	15	0
8	e	7	e	16181.213	16181.1679	0.0451	R(7)	15	0
2	e	3	e	16180.593	16180.5879	0.0051	P(3)	15	0
5	f	5	e	16179.928	16179.9132	0.0148	Q(5)	15	0
9	e	8	e	16179.607	16179.5549	0.0521	R(8)	15	0
3	e	4	e	16178.963	16178.8694	0.0936	P(4)	15	0
6	f	6	e	16178.232	16178.2475	-0.0155	Q(6)	15	0
10	e	9	e	16177.657	16177.6643	-0.0073	R(9)	15	0
4	e	5	e	16176.88	16176.8733	0.0067	P(5)	15	0
7	f	7	e	16176.291	16176.3041	-0.0131	Q(7)	15	0
11	e	10	e	16175.461	16175.496	-0.035	R(10)	15	0
5	e	6	e	16174.537	16174.5996	-0.0626	P(6)	15	0
8	f	8	e	16174.128	16174.0831	0.0449	Q(8)	15	0
12	e	11	e	16172.977	16173.0501	-0.0731	R(11)	15	0
6	e	7	e	16172.055	16172.0483	0.0067	P(7)	15	0
9	f	9	e	16171.55	16171.5845	-0.0345	Q(9)	15	0
13	e	12	e	16170.21	16170.3266	-0.1166	R(12)	15	0
7	e	8	e	16169.254	16169.2193	0.0347	P(8)	15	0
10	f	10	e	16168.857	16168.8083	0.0487	Q(10)	15	0
8	e	9	e	16166.181	16166.1127	0.0683	P(9)	15	0
11	f	11	e	16165.915	16165.7544	0.1606	Q(11)	15	0

Table A.7: Assignments for the $\mathrm{A}'^{1}\Pi(\mathrm{X}\sigma\pi^{-1})$ $(\mathrm{v}' = 16, \mathrm{v}'' = 0)$ band.

J’	S’	J”	S”	Observed	Calculated	Obs-Calc	Assignment	v’	v”
4	e	3	e	16653.074	16653.0275	0.0465	R(3)	16	0
3	e	2	e	16653.074	16653.2649	-0.1909	R(2)	16	0
2	e	1	e	16653.074	16653.2215	-0.1475	R(1)	16	0
1	e	0	e	16653.074	16652.8973	0.1767	R(0)	16	0
5	e	4	e	16652.567	16652.5095	0.0575	R(4)	16	0
2	f	2	e	16651.689	16651.4503	0.2387	Q(2)	16	0
3	f	3	e	16650.631	16650.6081	0.0229	Q(3)	16	0
7	e	6	e	16650.631	16650.6311	-0.0001	R(6)	16	0
4	f	4	e	16649.467	16649.4851	-0.0181	Q(4)	16	0
8	e	7	e	16649.467	16649.2709	0.1961	R(7)	16	0
2	e	3	e	16648.78	16648.7935	-0.0135	P(3)	16	0
5	f	5	e	16648.076	16648.0815	-0.0055	Q(5)	16	0
3	e	4	e	16647.079	16647.0657	0.0133	P(4)	16	0
6	f	6	e	16646.414	16646.3971	0.0169	Q(6)	16	0
10	e	9	e	16645.618	16645.7081	-0.0901	R(9)	16	0
4	e	5	e	16644.727	16645.0571	-0.3301	P(5)	16	0
7	f	7	e	16644.252	16644.4319	-0.1799	Q(7)	16	0
11	e	10	e	16643.588	16643.5056	0.0824	R(10)	16	0
5	e	6	e	16642.744	16642.7679	-0.0239	P(6)	16	0
8	f	8	e	16642.319	16642.1861	0.1329	Q(8)	16	0
12	e	11	e	16640.929	16641.0224	-0.0934	R(11)	16	0
6	e	7	e	16640.153	16640.1979	-0.0449	P(7)	16	0
9	f	9	e	16639.689	16639.6595	0.0295	Q(9)	16	0
8	e	9	e	16634.41	16634.2157	0.1943	P(9)	16	0
11	f	11	e	16633.694	16633.764	-0.0700	Q(11)	16	0

Table A.8: Assignments for the $\mathrm{A}'^1\Pi(\mathrm{X}\sigma\pi^{-1})$ $(\mathrm{v}' = 17, \mathrm{v}'' = 0)$ band.

J’	S’	J”	S”	Obs	Calc	Obs-Calc	Assignment	v’	v”
3	e	2	e	17109.852	17109.8125	0.0395	R(2)	17	0
2	e	1	e	17109.852	17109.7741	0.0779	R(1)	17	0
4	e	3	e	17109.589	17109.5685	0.0205	R(3)	17	0
1	e	0	e	17109.589	17109.4533	0.1357	R(0)	17	0
5	e	4	e	17109.024	17109.0421	-0.0181	R(4)	17	0
1	f	1	e	17108.541	17108.5677	-0.0267	Q(1)	17	0
7	e	6	e	17107.097	17107.142	-0.045	R(6)	17	0
3	f	3	e	17107.097	17107.1557	-0.0587	Q(3)	17	0
1	e	2	e	17106.683	17106.7965	-0.1135	P(2)	17	0
4	f	4	e	17106.011	17106.0261	-0.0151	Q(4)	17	0
8	e	7	e	17105.75	17105.7684	-0.0184	R(7)	17	0
2	e	3	e	17105.358	17105.3461	0.0119	P(3)	17	0
5	f	5	e	17104.616	17104.6141	0.0019	Q(5)	17	0
9	e	8	e	17104.093	17104.1123	-0.0193	R(8)	17	0
3	e	4	e	17103.57	17103.6133	-0.0433	P(4)	17	0
6	f	6	e	17102.954	17102.9196	0.0344	Q(6)	17	0
10	e	9	e	17102.166	17102.1739	-0.0079	R(9)	17	0
4	e	5	e	17101.609	17101.5981	0.0109	P(5)	17	0
7	f	7	e	17100.954	17100.9428	0.0112	Q(7)	17	0
11	e	10	e	17099.876	17099.953	-0.077	R(10)	17	0
8	f	8	e	17098.7	17098.6836	0.0164	Q(8)	17	0
12	e	11	e	17097.47	17097.4498	0.0202	R(11)	17	0
6	e	7	e	17096.669	17096.7204	-0.0514	P(7)	17	0
9	f	9	e	17096.183	17096.1419	0.0411	Q(9)	17	0
13	e	12	e	17094.68	17094.6641	0.0159	R(12)	17	0
7	e	8	e	17093.86	17093.858	0.002	P(8)	17	0
10	f	10	e	17093.373	17093.3179	0.0551	Q(10)	17	0

Appendix B

Appendix B: LIF System

B.1 System Overview

B.1.1 Ablation Translation/Rotation Holder

The original ablation/rotation metal rod holder was designed by Dr. Jacob Stewart and Dr. Michael Sullivan to minimize the number of holes. This is a good idea, since holes create leaks, and those leaks decrease the total amount airflow across the metal rod and ultimately the jet output which is directed toward the instrument optics. The translation and rotation was accomplished by using a threaded screw attached to a stepper motor. The disadvantage to this design was that it was extremely difficult to align the ablation laser onto the metal rod since the laser input was the same as the jet expansion output, and the signal was overall very unreliable. One notable advantage of this approach is that fewer holes in the block design allow for better pressure transfer through the output port.

The second iteration was designed by Dr. Daniel Fhroman and modified by Joel Schmitz. This design used the more traditional approach for our lab, which involves using a separate hole perpendicular to the expansion axis for the ablation block. The translation and rotation used the same single-motor scheme as the previous design. This design allowed much more facile ablation alignment, but the entire system led to a high degree of rod-instability. Overall, the simpler ablating laser alignment made this system an adequate replacement for the previous iteration.

I imagined and assembled the current version of the rotation translation assembly. The assembly features multiple articulation points for adjusting the stepper motors and rod, as well as the pulsed jet output. The entire assembly can also be translated along the bottom of the chamber without changing the relative alignment of any of the other parts. The parts for the device are commercially available from ThorLabs, so that anyone can easily replicate the assembly. A diagram of the bare device is shown in Figure B.1. The support is extremely rugged and effectively has an unlimited support weight for any reasonable application. The design is straightforward with only few components, and allows for mounting of nearly anything to to the breadboard style stages, so that future additions to the ablation block such as a discharge source, which has been designed by Ariana Rodruiguez and Joel Schmitz, are easily added. The stepper motors used in the final version of this assembly was a custom combination unit from Hayden-Kerk (LR35SKH4AE-05-001), which Thomas Persinger and I collaborated on for shipment. I had discovered that the coatings in the motor were sublimating under the high vacuum of our chambers, causing the electromagnets to fail, and Thomas negotiated with the engineers at Hayden-Kerk to produce and deliver a custom version of the motor, which contained high-vacuum grease containing Teflon. These motors were installed in both the LIF chamber and the REMPI/ZEKE chamber, and although the motor has burnt out once in the latter chamber, likely due to an over-current event due to user error, the motor has been a workhorse in the LIF chamber to the best of my knowledge. It is notable that the motor controller programs were modified to include maximum current controls, and these should be included in any program that is designed in the future to control Phidgets stepper motor boards. Heat loading on the stepper motors becomes an issue in ablation systems that are completely inside the vacuum chamber, since there is no air for thermal transport. An alternative solution is to have the motors run outside the chamber, but this adds complexity to the system since some motion transfer solution needs to be added to get the rotational motion to the rod inside the experiment. The Hayden-Kerk motors cost about \$500 each; a two year replacement cycle is acceptable although no ideal. An alternative, implemented by group member Noah Jaffe, is to simply pack the windings of cheap stepper motors with high-vacuum grease. This solution requires that the experimentalist design and construct their own rotation-translation scheme, but has the advantage of lessened motor replacement cost.

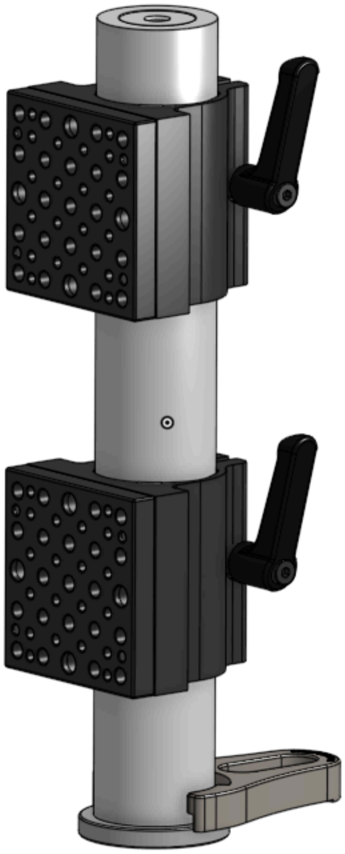

Figure B.1: CAD drawing of the Modern translation/rotation holder assembly.

B.1.2 Optical train

B.1.3 Monochromator

The monochromator addition was originally designed to more easily interface communicate with modern computer software, as well as to allow for 2D-LIF measurements. Unfortunately, the grating installed in the monochromator (1200 lines/mm) is unsuitable for the molecules that we study, given that the bandwidth of an image is about 15 nm under when this grating is installed. If a 300 lines/mm grating were to be installed on the device, the bandwidth would increase to 60 nm, giving usable images. The gratings must be custom ordered for the monochromator, since the unit is rather old and the . Additionally, the drivers for LabVIEW had not been updated in some time, so the control box for the monochromator was replaced with a more modern stepper motor driving unit, which interfaces more easily to our data collection system.

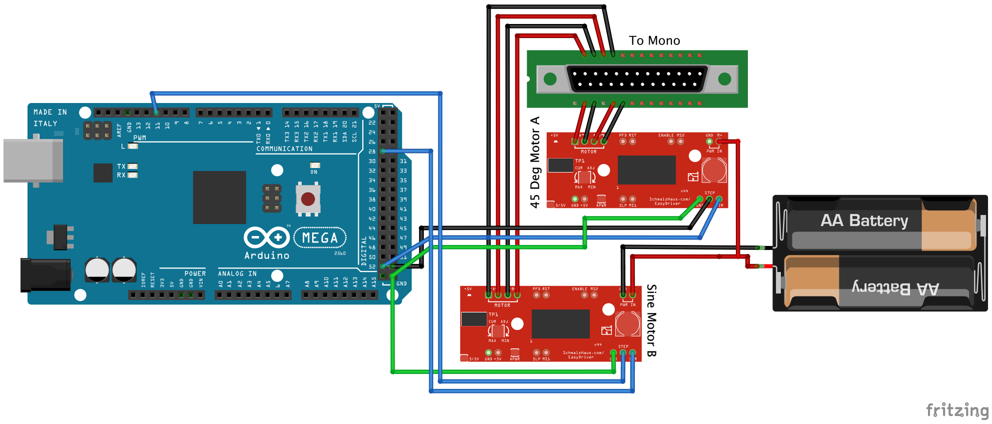

Figure B.2: Cartoon showing the main idea of the connections to the 25-pin serial port to the monochromator. The batteries are actually a 70W power supply unit, and the motor controllers are functionally similar.

B.2 Monochromator Source Code

Here is the source code for the monochromator. Copying and pasting this into the Arduino IDE, along with including the EEPROM.h and digitalWriteast.h libraries, will allow you to compile and run this an an Arduino MEGA. Reading the code essentially describes all of the pinouts and serial commands for the device, and these values can be modified if desired.

```
//******INCLUSIONS

#include <EEPROM.h>
#include <digitalWriteFast.h>
//changes write operation speed to ~125 ns
//instead of ~6000 ns



//******CONSTANTS

const int motorAPUL = 52;
// Pulsing pin for Up_Down motor
const int motorBPUL = 11;
const int motorADir = 53;
const int motorAEna = 24;
const int btnPinADir = 23;
// the pin that the motor A Dir pushbtn is attached to
const int btnPinAEna = 25;

//const int motorBPUL = 11;
const int motorBDir = 28;
```

```
const int testBtn = 30;

const int motorAStateAddress = 0;
const int motorSpeedDial = 0;
const int motorBPositionAddress = 0;



const int motorALowLimit= 46;
const int motorAHighLimit = 47;
const int motorBLowLimit = 48;
const int motorBHighLimit = 49;

const int btnMotorBDown = 50;
const int btnMotorBUp = 51;

const long interval = 500;
const long backlashInterval = 4000;
unsigned long previousMicros = 0;

const int backlash = 50; // adds backlash for N steps

//********VARIABLES

int motorAState = LOW;
// motorAState used to set Motor A ENA
int motorBState = LOW;
// motorBState used to set Motor B ENA
```

```
bool motorBDirVal = LOW;
//Variable to keep track of direction of motor

bool motorBPULVar = LOW;
bool motorAPULVar = LOW;

int btnInterval = 0;
int btnPushCounter = 0;
// counter for the number of btn presses
int btnState = 0;
// current state of the btn
int lastBtnState = 0;
// previous state of the btn
bool eventMotorAFlag = 0;
bool motorAPosition = 0;
// Position of motor A is either up or down.

long motorBPosition = 0; //Position of motor B is variable.

long steps = 0;
long desiredDialReading = 0;
long readingA = 0;
long motorBPositionNew = 0;

// Generally, you should use "unsigned long"
// for variables that hold time
// The value will quickly become too large for an
// int to store
unsigned long previousMicrosA = 0;
```

```
// store last time LED update
unsigned long previousMicrosB = 0;

// constants won't change :
long potRead = 0;
// interval at which to blink (milliseconds)

int frequencyA = 2000;
int frequencyB = 4000;
long pulseDelay = 0;
double rotations = 1;
const long product = 400000;

int backlashFlag = 0;

enum State
{
  idle,
  sendSerialStatus,
  //Send the current position of motor A and motor B
  moveMotorA,
  // Motor Attatched to up/down mirror
  moveMotorAUI,
  // Motor A control from buttons
  moveMotorB,
  // Motor attatched to diff grating (200 steps/rev)
  moveMotorBUI,
  //Motor B control with buttons
  backlashState,
```

```
  updateVals,
};
enum State state; //the actual instance, so can't be a typedef

//***********SETUP

void setup()
{
  state = idle;

  Serial.begin(9600);

  pinMode(motorADir, OUTPUT);
  pinMode(motorBDir, OUTPUT);

  pinMode(testBtn, INPUT);

  pinMode(motorAPUL,OUTPUT);
  pinMode(motorBPUL,OUTPUT);

  pinMode(btnMotorBDown, INPUT);
  pinMode(btnMotorBUp, INPUT);

  pinMode(A0, INPUT);



//limit switches
  pinMode(motorALowLimit, INPUT);
  pinMode(motorAHighLimit, INPUT);
```

```
  pinMode(motorBLowLimit, INPUT);
  pinMode(motorBHighLimit, INPUT);

  motorAPosition = EEPROM.read(motorAStateAddress);
}

//***********MAIN PROGRAM

void loop()
{
  if (state == idle)
  {
    HandleSerial();
    HandleUI();
  }
  if (state == updateVals)
  {
    //UpdateVals()
  }
  if (state == moveMotorA) //Move the mirror motor
  {
    long i = 0;
    while(i < steps)
    {
      if (digitalRead(motorALowLimit)
     == HIGH && digitalRead(motorADir) == LOW)
      {
        Serial.println("Lower limit reached");
        break;
```

```
    }
    if (digitalRead(motorAHighLimit)
    == HIGH && digitalRead(motorADir) == HIGH)
    {
      Serial.println(”Upper limit reached”);
      break;
    }
    unsigned long currentMicros = micros();

    if (currentMicros - previousMicros >= interval)
    {
    previousMicros = currentMicros;
      if (motorAPULVar == LOW)
      {
        digitalWrite(motorAPUL,HIGH);
        motorAPULVar = HIGH;
        ++i;
      }
      else
      {
        digitalWrite(motorAPUL,LOW);
        motorAPULVar = LOW;
      }
    }

  }
  state = idle;
}
```

```
if (state == moveMotorB) //Move the diffraction grating motor
{
if (steps > 5000)
{
  backlashFlag = 1;
}
{
  long i = 0;
  while(i < steps)
  {
    if (digitalRead(motorBLowLimit)
    == HIGH && digitalRead(motorBDir) == LOW)
    {
      Serial.println(”Lower limit reached”);
      break;
    }
    if (digitalRead(motorBHighLimit)
    == HIGH && digitalRead(motorBDir) == HIGH)
    {
      Serial.println(”Upper limit reached”);
      break;
    }
    unsigned long currentMicros = micros();

    if (currentMicros - previousMicros >= interval)
    {
    previousMicros = currentMicros;
      if (motorBPULVar == LOW)
      {
```

```
         digitalWriteFast(motorBPUL,HIGH);
         motorBPULVar = HIGH;
         ++i;
         if (motorBDirVal == HIGH)
         {
         ++motorBPosition;
         }
      if (motorBDirVal == LOW)
         {
         --motorBPosition;
         }
      }
      else
      {
         digitalWriteFast(motorBPUL,LOW);
         motorBPULVar = LOW;
      }
   }

}

if (backlashFlag == 1)
{
state = backlashState;
}
else
{
Serial.println(”done”);
Serial.println(motorBPosition);
```

```
    state = idle;
    }
  }
  }

if (state == backlashState)
// activate backlash
{
  if (backlashFlag == 1)
  {
    digitalWrite(motorBDir, LOW);
  }
  if (backlashFlag == 0)
  {
    digitalWrite(motorBDir, HIGH);
  }
    long i = 0;
    while(i < backlash)
    {
      if (digitalRead(motorBLowLimit)
      == HIGH && digitalRead(motorBDir) == LOW)
      {
        Serial.println(”Lower limit reached”);
        break;
      }
      if (digitalRead(motorBHighLimit)
      == HIGH && digitalRead(motorBDir) == HIGH)
      {
        Serial.println(”Upper limit reached”);
```

```
    break;
  }

  unsigned long currentMicros = micros();

  if (currentMicros - previousMicros >= backlashInterval)
  {
  previousMicros = currentMicros;
    if (motorBPULVar == LOW)
    {
      digitalWriteFast(motorBPUL,HIGH);
      motorBPULVar = HIGH;
      ++i;
    }
    else
    {
      digitalWriteFast(motorBPUL,LOW);
      motorBPULVar = LOW;
    }
  }
}
if (backlashFlag == 1)
{
  backlashFlag = 0;
  state = backlashState;
}
else
{
  Serial.println(”done”);
```

```
        Serial.println(motorBPosition);
        state = idle;
      }
  }

    if (state == moveMotorBUI)
    //Move the diffraction grating motor
    {
      btnInterval = (-19*potRead)+20000;
      while(digitalRead(btnMotorBDown)
      == 1 || digitalRead(btnMotorBUp) == 1)
      {

        if (digitalRead(motorBLowLimit)
        == HIGH && digitalRead(motorBDir) == LOW)
        {
          Serial.println("Lower limit reached");
          break;
        }
        if (digitalRead(motorBHighLimit)
        == HIGH && digitalRead(motorBDir) == HIGH)
        {
          Serial.println("Upper limit reached");
          break;
        }
        unsigned long currentMicros = micros();

        if (currentMicros - previousMicros >= btnInterval)
        {
```

```
      previousMicros = currentMicros;
        if (motorBPULVar == LOW)
        {
          digitalWriteFast(motorBPUL,HIGH);
          motorBPULVar = HIGH;
          if (motorBDirVal == HIGH)
          {
          ++motorBPosition;
          }
        if (motorBDirVal == LOW)
          {
          --motorBPosition;
          }
        }
        else
        {
          digitalWriteFast(motorBPUL,LOW);
          motorBPULVar = LOW;
        }
      }
    }
    state = idle;
  }
}//end loop

// *************FUNCTIONS
  // ***********Serial

void HandleSerial()
```

```
{
  while (Serial.available() > 0)
  {
    char incomingCharacter = Serial.read();
    switch (incomingCharacter)
     {
     case '-': // Move the Mirror Down
     steps = 3600;
     digitalWrite(motorADir, HIGH);
     state = moveMotorA;
     break;

     case '+': // Move the mirror Up
     steps = 3600;
     digitalWrite(motorADir, LOW);
     state = moveMotorA;
     break;

     case 'd': //motor B goes down
     steps = 200;
     digitalWriteFast(motorBDir, LOW);
     motorBDirVal = LOW;
     state = moveMotorB;
     break;

     case 'u': //motor B goes up
     steps = 200;
     digitalWriteFast(motorBDir, HIGH);
     motorBDirVal = HIGH;
```

```
 state = moveMotorB;
 break;

 case 'p': //print current position
  Serial.println(motorBPosition);
 break;

 case 'l': // motor B goes to motor position X
 Serial.println(motorBPosition);
 motorBPositionNew  = Serial.parseInt();
 Serial.println(motorBPositionNew);
 steps = motorBPositionNew - motorBPosition;
if (steps < 0)
{
  digitalWrite(motorBDir, LOW);
  motorBDirVal = LOW;
  steps = -1*steps;
}
else
{
  digitalWrite(motorBDir, HIGH);
  motorBDirVal = HIGH;
}

 state = moveMotorB;
 break;
 }


}
```

```
}
// *********btnUI

void HandleUI()
{
btnState = digitalRead(testBtn);
// compare the btnState to its previous state
potRead = analogRead(A0);
//Serial.println(potRead);
//uncomment to read the potentiometer through serial

  if(digitalRead(btnMotorBDown) ==1)
  {
    digitalWrite(motorBDir, LOW);
    motorBDirVal = 0;
    state = moveMotorBUI;
  }

  if(digitalRead(btnMotorBUp) ==1)
  {
    digitalWrite(motorBDir, HIGH);
    motorBDirVal = 1;
    state = moveMotorBUI;
  }



  if (digitalRead(testBtn) == 1)
  {
    eventMotorAFlag = 1;
```

```
}

if (btnState != lastBtnState)
{
   // if the state has changed, increment the counter
  if (btnState == HIGH)
  {
    // if the current state is HIGH then the btn
    // went from off to on:
    btnPushCounter++;
    Serial.println("on");
    Serial.print("number of btn pushes:  ");
    Serial.println(btnPushCounter);
  }
  else
  {
    // if the current state is LOW then the btn
    // went from on to off:
    Serial.println("off");
   }
   // Delay a little bit to avoid bouncing
 }
  // save the current state as the last state,
  //for next time through the loop
  lastBtnState = btnState;

  if (eventMotorAFlag == 1)
  {
    if (motorAPosition == 0)
```

```
        {
          digitalWrite(motorADir, HIGH);
          tone(motorAPUL,1000);
          delay(3000);
          noTone(motorAPUL);
          eventMotorAFlag = 0;
          motorAPosition = 1;
         EEPROM.write(0,motorAPosition);
        }
        else
        {
          digitalWrite(motorADir, LOW);
          tone(motorAPUL,1000);
          delay(3000);
          noTone(motorAPUL);
          eventMotorAFlag = 0;
          motorAPosition = 0;
         EEPROM.write(0,motorAPosition);
        }
      }
}
```

B.2.1 Camera Attachment

The monochromator's output port required a coupling unit so that the Andor ICCD (Andor, 334T) could be coupled to it. After reviewing implementations in other labs for the attachment, it became clear that telescoping functionality would be extremely useful, since the sensor's distance from the image formed by the monochromator was not exactly known. Given my lack of formal engineering training, I try to design things so that they do not need to be exact so that no further of the machined parts is necessary, since these modifications tend to result in aesthetic and functional disaster. The attachment works very well and accomplishes all of the design goals. Thank you to the machine shop at Georgia Institute of Technology for machining this part; the end-product exactly matched the supplied design documents.

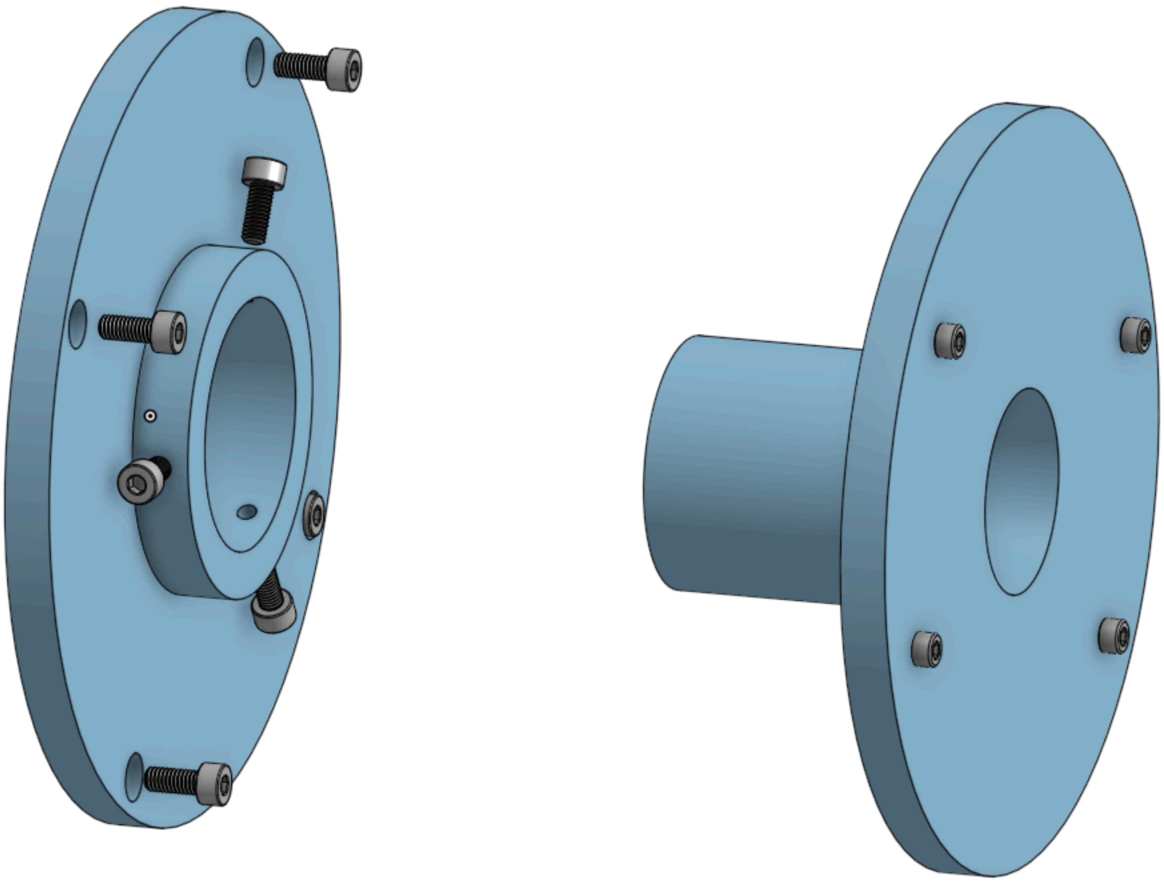

Figure B.3: CAD model of the monochromator to camera attachment (left) and camera attachment to camera (right). The triangular screw pattern locks in camera rotation and translation about the rotational axis.

Bibliography

[1] King-Chuen Lin and Raymond Vetter. Alkali-hydrogen reactions. *International Reviews in Physical Chemistry*, 21(3):357–383, jul 2002. ISSN 0144-235X. doi: 10.1080/01442350210150732. URL `https://www.tandfonline.com/doi/full/10.1080/01442350210150732`.

[2] Li-hsyan Fan, Jye-jong Chen, Yann-yow Lin, and Wei-tzou Luh. Reaction of Rb(5^2D, 7^2S) with H_2. *The Journal of Physical Chemistry A*, 103(10):1300–1305, mar 1999. ISSN 1089-5639. doi: 10.1021/jp984334a. URL `https://pubs.acs.org/doi/10.1021/jp984334a`.

[3] Xin Huang, Jianzheng Zhao, Guoqiang Xing, Xuebin Wang, and Richard Bersohn. The reaction of Cs(8^2P) and Cs(9^2P) with hydrogen molecules. *The Journal of Chemical Physics*, 104(4):1338–1343, jan 1996. ISSN 0021-9606. doi: 10.1063/1.470790. URL `http://www.journal.csj.jp/doi/10.1246/bcsj.43.3425http://aip.scitation.org/doi/10.1063/1.470790`.

[4] F.X. Gadéa, J.M. L'hermite, G. Rahmat, and R. Vetter. Hyperfine structure effect in the Cs(7P) + H^2 reaction. Experimental observation and theoretical interpretation. *Chemical Physics Letters*, 151(3):183–187, oct 1988. ISSN 00092614. doi: 10.1016/0009-2614(88)85270-9. URL `https://linkinghub.elsevier.com/retrieve/pii/0009261488852709`.

[5] Nathan D. Zameroski, Wolfgang Rudolph, Gordon D. Hager, and David A. Hostutler. A study of collisional quenching and radiation-trapping kinetics for Rb(5p) in the presence of methane and ethane using time-resolved fluorescence. *Journal of Physics B: Atomic, Molecular and Optical Physics*, 42(24):245401, dec 2009. ISSN 0953-4075. doi: 10.1088/0953-4075/42/24/245401. URL `https://iopscience.iop.org/article/10.1088/0953-4075/42/24/245401`.

[6] Z. Konefał. Observation of collision induced processes in rubidium–ethane vapour. *Optics Communications*, 164(1-3):95–105, jun 1999. ISSN 00304018. doi: 10.1016/S0030-4018(99)00161-3. URL `https://linkinghub.elsevier.com/retrieve/pii/S0030401899001613`.

[7] V. N. Azyazov, S. M. Bresler, A. P. Torbin, A. M. Mebel, and M. C. Heaven. Removal of $rb(6^2p) by h_2, ch_4, and c_2h_6$. *Optics Letters*, 41(4):669, feb 2016. ISSN

0146-9592. doi: 10.1364/ol.41.000669. URL `https://www.osapublishing.org/abstract.cfm?URI=ol-41-4-669`.

[8] A V Bogachev, Sergey G Garanin, A M Dudov, V A Eroshenko, S M Kulikov, G T Mikaelian, V A Panarin, V O Pautov, A V Rus, and Stanislav A Sukharev. Diode-pumped caesium vapour laser with closed-cycle laser-active medium circulation. *Quantum Electronics*, 42(2):95–98, feb 2012. ISSN 1063-7818. doi: 10.1070/QE2012v042n02ABEH014734. URL `http://stacks.iop.org/1063-7818/42/i=2/a=A01?key=crossref.4534d1248da98948de245d14af2b4e51`.

[9] A. Badalyan, V. Chaltykyan, Yasuhiko Fujii, Yu Malakyan, Masaki Ozawa, A. Papoyan, and S. Shmavonyan. Studies of laser induced cesium and rubidium hydride formation in vapor cells and their application for isotope separation. *Progress in Nuclear Energy*, 47(1-4):389–396, jan 2005. ISSN 01491970. doi: 10.1016/j.pnucene.2005.05.038. URL `https://linkinghub.elsevier.com/retrieve/pii/S0149197005000880`.

[10] Koji Tamura and Masaki Ozawa. Cesium (Cs) particle formation based on a laser photochemical reaction with a self-injection-seeded Ti:sapphire laser for Cs isotope separation. *Journal of Nuclear Science and Technology*, 52(6):872–877, jun 2015. ISSN 0022-3131. doi: 10.1080/00223131.2014.987184. URL `http://dx.doi.org/10.1080/00223131.2014.987184http://www.tandfonline.com/doi/full/10.1080/00223131.2014.987184`.

[11] I. N. Siara and L. Krause. Inelastic Collisions between Excited Alkali Atoms and Molecules. VIII. $6^2P_{1/2}$ – $6^2P_{3/2}$ Mixing and Quenching in Mixtures of Rubidium with H_2 , HD, D_2 , N_2 , CH_4 , and CD_4. *Canadian Journal of Physics*, 51(3):257–265, feb 1973. ISSN 0008-4204. doi: 10.1139/p73-033. URL `http://www.nrcresearchpress.com/doi/10.1139/p73-033`.

[12] Man-Lin Chen, Wei-Chou Lin, and Wei-Tzou Luh. Electronic to vibrational energy transfer between Rb(5^2P_J) and H_2. *The Journal of Chemical Physics*, 106(14):5972–5978, apr 1997. ISSN 0021-9606. doi: 10.1063/1.473244. URL `http://aip.scitation.org/doi/10.1063/1.473244`.

[13] B. V. Zhdanov and R. J. Knize. DPAL: historical perspective and summary of achievements. 2013. doi: 10.1117/12.2033923. URL `https://doi.org/10.1117/12.2033923`.

[14] F. Gao, F. Chen, J.J. Xie, D.J. Li, L.M. Zhang, G.L. Yang, J. Guo, and L.H. Guo. Review on diode-pumped alkali vapor laser. *Optik*, 124(20):4353–4358, oct 2013. ISSN 00304026. doi: 10.1016/j.ijleo.2013.01.061. URL `https://linkinghub.elsevier.com/retrieve/pii/S0030402613002234`.

[15] Raymond J. Beach, William F. Krupke, V. Keith Kanz, Stephen A. Payne, Mark A. Dubinskii, and Larry D. Merkle. End-pumped continuous-wave alkali vapor lasers: experiment, model, and power scaling. *Journal of the*

Optical Society of America B, 21(12):2151, dec 2004. ISSN 0740-3224. doi: 10.1364/JOSAB.21.002151. URL `https://www.osapublishing.org/abstract.cfm?URI=josab-21-12-2151`.

[16] Lindsay O.Brien Quarrie. The effects of atomic rubidium vapor on the performance of optical windows in Diode Pumped Alkali Lasers (DPALs). *Optical Materials*, 35(5):843–851, mar 2013. ISSN 09253467. doi: 10.1016/j.optmat.2012.10.040. URL `http://dx.doi.org/10.1016/j.optmat.2012.10.040https://linkinghub.elsevier.com/retrieve/pii/S0925346712004727`.

[17] B.V. Zhdanov and R.J. Knize. Hydrocarbon-free potassium laser. *Electronics Letters*, 43(19):1024, 2007. doi: 10.1049/el:20071587. URL `https://doi.org/10.1049/el:20071587`.

[18] Shen Yi-Fan, Dai Kang, Mu Bao-Xia, Wang Shu-Ying, and Cui Xiu-Hua. Energy-pooling collisions in rubidium: $5\mathrm{p}^{3/2} + 5\mathrm{p}_{3/2} \rightarrow 5\mathrm{s} + (\mathrm{nl} = 5\mathrm{d}, 7\mathrm{s})$. *Chinese Physics Letters*, 22(11):2805–2807, oct 2005. doi: 10.1088/0256-307x/22/11/022. URL `https://doi.org/10.1088/0256-307x/22/11/022`.

[19] O. S. Heavens. Radiative Transition Probabilities of the Lower Excited States of the Alkali Metals. *Journal of the Optical Society of America*, 51(10):1058, oct 1961. ISSN 0030-3941. doi: 10.1364/JOSA.51.001058. URL `https://www.osapublishing.org/abstract.cfm?URI=josa-51-10-1058`.

[20] William F. Krupke. Diode pumped alkali lasers (DPALs)—A review (rev1). *Progress in Quantum Electronics*, 36(1):4–28, jan 2012. ISSN 00796727. doi: 10.1016/j.pquantelec.2011.09.001. URL `http://dx.doi.org/10.1016/j.pquantelec.2011.09.001https://linkinghub.elsevier.com/retrieve/pii/S0079672711000413`.

[21] H. Bucka, B. Grosswendt, and H. A. Schssler. Level crossing-experiment im 62 p 3/2-term des rb i-spektrums. *Zeitschrift fr Physik*, 194(2):193–200, 1966. doi: 10.1007/bf01326046. URL `https://doi.org/10.1007/bf01326046`.

[22] John K. Link. Measurement of the Radiative Lifetimes of the First Excited States of Na, K, Rb, and Cs by Means of the Phase-Shift Method*. *Journal of the Optical Society of America*, 56(9):1195, sep 1966. ISSN 0030-3941. doi: 10.1364/JOSA.56.001195. URL `https://www.osapublishing.org/abstract.cfm?URI=josa-56-9-1195`.

[23] Axel D. Becke. Density-functional thermochemistry. III. The role of exact exchange. *The Journal of Chemical Physics*, 98(7):5648–5652, apr 1993. ISSN 0021-9606. doi: 10.1063/1.464913. URL `http://aip.scitation.org/doi/10.1063/1.464913`.

[24] Chengteh Lee, Weitao Yang, and Robert G. Parr. Development of the Colle-Salvetti correlation-energy formula into a functional of the electron density. *Physical Review B*, 37(2):785–789, jan 1988. ISSN 0163-1829. doi: 10.1103/PhysRevB.37.785. URL `https://link.aps.org/doi/10.1103/PhysRevB.37.785`.

[25] Karen L. Schuchardt, Brett T. Didier, Todd Elsethagen, Lisong Sun, Vidhya Gurumoorthi, Jared Chase, Jun Li, and Theresa L. Windus. Basis Set Exchange: A Community Database for Computational Sciences. *Journal of Chemical Information and Modeling*, 47(3):1045–1052, may 2007. ISSN 1549-9596. doi: 10.1021/ci600510j. URL `https://pubs.acs.org/doi/10.1021/ci600510j`.

[26] George D. Purvis and Rodney J. Bartlett. A full coupled-cluster singles and doubles model: The inclusion of disconnected triples. *The Journal of Chemical Physics*, 76(4):1910–1918, 1982. ISSN 00219606. doi: 10.1063/1.443164.

[27] Gustavo E. Scuseria, Curtis L. Janssen, and Henry F. Schaefer. An efficient reformulation of the closed-shell coupled cluster single and double excitation (CCSD) equations. *The Journal of Chemical Physics*, 89(12):7382–7387, dec 1988. ISSN 0021-9606. doi: 10.1063/1.455269. URL `http://aip.scitation.org/doi/10.1063/1.455269`.

[28] Gustavo E Scuseria and Henry F. Schaefer. Is coupled cluster singles and doubles (CCSD) more computationally intensive than quadratic configuration interaction (QCISD)? *The Journal of Chemical Physics*, 90(7):3700–3703, apr 1989. ISSN 0021-9606. doi: 10.1063/1.455827. URL `http://aip.scitation.org/doi/10.1063/1.455827`.

[29] John A. Pople, Martin Head-Gordon, and Krishnan Raghavachari. Quadratic configuration interaction. A general technique for determining electron correlation energies. *The Journal of Chemical Physics*, 87(10):5968–5975, nov 1987. ISSN 0021-9606. doi: 10.1063/1.453520. URL `http://aip.scitation.org/doi/10.1063/1.453520`.

[30] M. J. Frisch, G. W. Trucks, H. B. Schlegel, G. E. Scuseria, M. A. Robb, J. R. Cheeseman, G. Scalmani, V. Barone, B. Mennucci, G. A. Petersson, H. Nakatsuji, M. Caricato, X. Li, H. P. Hratchian, A. F. Izmaylov, J. Bloino, G. Zheng, J. L. Sonnenberg, M. Hada, M. Ehara, K. Toyota, R. Fukuda, J. Hasegawa, M. Ishida, T. Nakajima, Y. Honda, O. Kitao, H. Nakai, T. Vreven, J. A. Montgomery, Jr., J. E. Peralta, F. Ogliaro, M. Bearpark, J. J. Heyd, E. Brothers, K. N. Kudin, V. N. Staroverov, R. Kobayashi, J. Normand, K. Raghavachari, A. Rendell, J. C. Burant, S. S. Iyengar, J. Tomasi, M. Cossi, N. Rega, J. M. Millam, M. Klene, J. E. Knox, J. B. Cross, V. Bakken, C. Adamo, J. Jaramillo, R. Gomperts, R. E. Stratmann, O. Yazyev, A. J. Austin, R. Cammi, C. Pomelli, J. W. Ochterski, R. L. Martin, K. Morokuma, V. G. Zakrzewski, G. A. Voth, P. Salvador, J. J. Dannenberg, S. Dapprich, A. D. Daniels, Ö. Farkas, J. B.

Foresman, J. V. Ortiz, J. Cioslowski, and D. J. Fox. Gaussian~09 Revision E.01. Gaussian Inc. Wallingford CT 2009.

[31] H-JKPJ Werner, PJ Knowles, G Knizia, FR Manby, M Schütz, P Celani, T Korona, R Lindh, A Mitrushenkov, G Rauhut, et al. Molpro, version 2010.1, a package of ab initio programs. *See http://www. molpro. net*, 2010.

[32] Boris V. Zhdanov and Randy J. Knize. Review of alkali laser research and development. *Optical Engineering*, 52(2):021010, oct 2012. ISSN 0091-3286. doi: 10.1117/1.OE.52.2.021010. URL `http://opticalengineering.spiedigitallibrary.org/article.aspx?doi=10.1117/1.OE.52.2.021010`.

[33] Jing Liu, Xiaoyan Shen, Yifan Shen, and Kang Dai. Resonant energy transfer between highly vibrationally excited RbH(RbD) and $H_2(D_2)$. *Chemical Physics*, 425:62–72, nov 2013. ISSN 03010104. doi: 10.1016/j.chemphys.2013.08.002. URL `http://dx.doi.org/10.1016/j.chemphys.2013.08.002https://linkinghub.elsevier.com/retrieve/pii/S0301010413003297`.

[34] L. Barbier and M Cheret. Energy pooling process in rubidium vapour. *Journal of Physics B: Atomic and Molecular Physics*, 16(17):3213–3228, sep 1983. ISSN 0022-3700. doi: 10.1088/0022-3700/16/17/014. URL `https://iopscience.iop.org/article/10.1088/0022-3700/16/17/014`.

[35] Indrajit Saha, Panayiotis Nikolaou, Nicholas Whiting, and Boyd M. Goodson. Characterization of violet emission from Rb optical pumping cells used in laser-polarized xenon NMR experiments. *Chemical Physics Letters*, 428(4-6):268–276, sep 2006. ISSN 00092614. doi: 10.1016/j.cplett.2006.07.074. URL `https://linkinghub.elsevier.com/retrieve/pii/S0009261406010955`.

[36] Zining Yang, Lei Zuo, Weihong Hua, Hongyan Wang, and Xiaojun Xu. Experimental measurement of ionization degree in diode-pumped rubidium laser gain medium. *Optics Letters*, 39(22):6501, nov 2014. ISSN 0146-9592. doi: 10.1364/OL.39.006501. URL `https://www.osapublishing.org/abstract.cfm?URI=ol-39-22-6501`.

[37] R.J. Knize, B.V. Zhdanov, and M.K. Shaffer. Photoionization in alkali lasers. *Optics Express*, 19(8):7894, apr 2011. ISSN 1094-4087. doi: 10.1364/OE.19.007894. URL `https://www.osapublishing.org/oe/abstract.cfm?uri=oe-19-8-7894`.

[38] Kirk C. Brown and Glen P. Perram. Spin-orbit relaxation and quenching of cesium 7^2P in mixtures of helium, methane, and ethane. *Physical Review A*, 85(2):022713, feb 2012. ISSN 1050-2947. doi: 10.1103/PhysRevA.85.022713. URL `https://link.aps.org/doi/10.1103/PhysRevA.85.022713`.

[39] I. N. Siara, R. U. Dubois, and L. Krause. Temperature dependence of cross sections for $7^2P_{1/2} - 7^2P_{3/2}$ excitation transfer and for quenching in cesium, induced in collisions with H_2 , N_2 , CH_4 , and CD_4. *Canadian Journal of*

Physics, 60(2):239–244, feb 1982. ISSN 0008-4204. doi: 10.1139/p82-029. URL `http://www.nrcresearchpress.com/doi/10.1139/p82-029`.

[40] Hans-Joachim Werner and Peter J. Knowles. An efficient internally contracted multiconfiguration–reference configuration interaction method. *The Journal of Chemical Physics*, 89(9):5803–5814, nov 1988. ISSN 0021-9606. doi: 10.1063/1.455556. URL `http://aip.scitation.org/doi/10.1063/1.455556`.

[41] HJ Werner, PJ Knowles, G Knizia, FR Manby, M Schütz, P Celani, T Korona, R Lindh, A Mitrushenkov, G Rauhut, et al. Molpro, version 2012.1, a package of ab initio programs, 2012; see http://www. molpro. net. *Google Scholar There is no corresponding record for this reference*, 2016.

[42] Chunsheng Xia, Xingqi Xu, Jinghua Huang, Chenyi Su, and Bailiang Pan. Influences of operating parameters on deleterious processes of side-pumped cesium vapor laser amplifiers with flowing medium. *Journal of Applied Physics*, 124 (5):053102, 2018.

[43] ZJ Jabbour, RK Namiotka, J Huennekens, Maria Allegrini, S Milošević, and F De Tomasi. Energy-pooling collisions in cesium: 6 p j+ 6 p j→ 6s+ (nl= 7p, 6d, 8s, 4f). *Physical Review A*, 54(2):1372, 1996. doi: https://doi.org/10.1103/PhysRevA.54.1372.

[44] JOHN Huennekens, Z Wu, and TG Walker. Ionization, excitation of high-lying atomic states, and molecular fluorescence in cs vapor excited at λ= 455.7 and 459.4 nm. *Physical Review A*, 31(1):196, 1985. doi: https://doi.org/10.1103/PhysRevA.31.196.

[45] S Wane and M Aymar. Excited-state photoionisation and radiative recombination for ions of the potassium isoelectronic sequence. *Journal of Physics B: Atomic and Molecular Physics*, 20(12):2657, 1987.

[46] Austin J Wallerstein, Glen P Perram, and Christoper A Rice. Excitation of higher lying states in a potassium diode-pumped alkali laser. *Applied Physics B*, 125(8):1–18, 2019. doi: 10.1007/s00340-019-7258-0.

[47] E. Arimondo, F. Giammanco, A. Sasso, and M.I. Schisano. Laser ionization and time-resolved ion collection in cesium vapor. *Optics Communications*, 55 (5):329–334, 1985. ISSN 00304018. doi: 10.1016/0030-4018(85)90180-4. URL `https://linkinghub.elsevier.com/retrieve/pii/0030401885901804`.

[48] E Arimondo, Francesco Giammanco, A Sasso, and MI Schisano. Laser ionization and time-resolved ion collection in cesium vapor. *Optics communications*, 55 (5):329–334, 1985.

[49] Yoichi Momozaki and Mohamed S El-Genk. Dissociative recombination coefficient for low temperature equilibrium cesium plasma. *Journal of applied physics*, 92(2):690–697, 2002. doi: 10.1063/1.1486250.

[50] Zhi-Gang Feng, Lin-Jie Zhang, Jian-Ming Zhao, Chang-Yong Li, and Suo-Tang Jia. Lifetime measurement of ultracold caesium rydberg states. *Journal of Physics B: Atomic, Molecular and Optical Physics*, 42(14):145303, 2009. doi: 10.1088/0953-4075/42/14/145303.

[51] AJ Wallerstein, Glen Perram, and Christopher A Rice. Excitation of higher lying energy states in a rubidium dpal. In *Solid State Lasers XXVII: Technology and Devices*, volume 10511, page 105112J. International Society for Optics and Photonics, 2018.

[52] C Gabbanini, M Biagini, S Gozzini, A Lucchesini, and L Moi. Na-cs hornbeck-molnar ionization. *Journal of Physics B: Atomic, Molecular and Optical Physics*, 24(17):3807, 1991.

[53] B Carré, G Spiess, JM Bizau, P Dhez, P Gérard, F Wuilleumier, JC Keller, JL Le Gouët, JL Picqué, DL Ederer, et al. Electron spectrometry study of associative and penning ionization in laser excited sodium vapor. *Optics communications*, 52(1):29–34, 1984.

[54] Kholoud A Hamam and MA Mahmoud. Mechanisms of plasma formation in potassium vapor excited by nanosecond resonant laser pulses. *Life Science Journal*, 15(2), 2018.

[55] L Barbier and M Cheret. Energy pooling process in rubidium vapour. *Journal of Physics B: Atomic and Molecular Physics*, 16(17):3213, 1983.

[56] MA Mahmoud, YEE Gamal, and HA Abd El-Rahman. Ion formation in laser-irradiated cesium vapor. *Journal of Quantitative Spectroscopy and Radiative Transfer*, 102(2):241–250, 2006.

[57] Dimitri Pappas, Benjamin W Smith, Nicolo Omenettó, and James D Winefordner. Formation of a cesium plasma by continuous-wave resonance excitation. *Applied Spectroscopy*, 54(8):1245–1249, 2000.

[58] Jun Yamada, Kohji Shibata, Yoshiyuki Uchida, Yoshiaki Hioki, and Toshio Sahashi. Ionization mechanism of cesium plasma produced by irradiation of dye laser. *Japanese journal of applied physics*, 31(2R):377, 1992.

[59] Mi-Young Song, Jung-Sik Yoon, Hyuck Cho, Yukikazu Itikawa, Grzegorz P Karwasz, Viatcheslav Kokoouline, Yoshiharu Nakamura, and Jonathan Tennyson. Cross sections for electron collisions with methane. *Journal of Physical and Chemical Reference Data*, 44(2):023101, 2015. doi: 10.1063/1.4918630.

[60] Hal J Cambier and Timothy J Madden. Implementing and constraining higher fidelity kinetics for dpal models. *arXiv preprint arXiv:1902.10776*, 2019.

[61] Andreas F Molisch and Bernhard P Oehry. *Radiation trapping in atomic vapours*. Oxford University Press, 1998.

[62] Colin M. Western. PGOPHER: A program for simulating rotational, vibrational and electronic spectra. *Journal of Quantitative Spectroscopy and Radiative Transfer*, 186:221–242, jan 2017. ISSN 00224073. doi: 10.1016/j.jqsrt.2016.04.010. URL `https://linkinghub.elsevier.com/retrieve/pii/S0022407316300437`.

[63] AC Tam and W Happer. Spectroscopy of the csh (x 1σ+) state by laser-excited fluorescence. *The Journal of Chemical Physics*, 64(6):2456–2459, 1976. doi: https://doi.org/10.1063/1.432547.

[64] CB Alcock, VP Itkin, and MK Horrigan. Vapour pressure equations for the metallic elements: 298–2500k. *Canadian Metallurgical Quarterly*, 23(3):309–313, 1984. doi: 10.1179/cmq.1984.23.3.309.

[65] Daniel Semiaticki. *Spectroscopic Study of Kinetic Processes Occurring upon Photoexcitation of Alkali Metal Vapors Mixed with Rare Gases.* PhD thesis, Emory University, 2014.

[66] M. Alina Gearba, Philip H. Rich, Lucy A. Zimmerman, Matthew D. Rotondaro, Boris V. Zhdanov, Randall J. Knize, and Jerry F. Sell. Measurements of cesium mixing and quenching cross sections in methane gas: understanding sources of heating in cesium vapor lasers. *Optics Express*, 27(7):9676, apr 2019. ISSN 1094-4087. doi: 10.1364/OE.27.009676. URL `https://www.osapublishing.org/abstract.cfm?URI=oe-27-7-9676`.

[67] Greg A Pitz, Charles D Fox, and Glen P Perram. Pressure broadening and shift of the cesium d 2 transition by the noble gases and n 2, h 2, hd, d 2, ch 4, c 2 h 6, cf 4, and he 3 with comparison to the d 1 transition. *Physical Review A*, 82(4):042502, 2010.

[68] Timothy M True, Christopher A Rice, and Glen P Perram. The cesium 62p3/2 to 82s1/2 line shape broadened by he, ar, and kr. *Journal of Quantitative Spectroscopy and Radiative Transfer*, 250:107010, 2020.

[69] Timothy M. True, Christopher A. Rice, and Glen P. Perram. Rubidium excited state line shapes from 5p to 5d and 7s broadened by helium. *Journal of Quantitative Spectroscopy and Radiative Transfer*, 274:107879, 2021. ISSN 0022-4073. doi: https://doi.org/10.1016/j.jqsrt.2021.107879. URL `https://www.sciencedirect.com/science/article/pii/S0022407321003721`.

[70] Eyal Yacoby, Ilya Auslender, Karol Waichman, Boris D. Barmashenko, and Salman Rosenwaks. Dependence of cs atoms density and laser power on gas velocity in cs dpal. *Optics & Laser Technology*, 116:18–21, 2019. ISSN 0030-3992. doi: https://doi.org/10.1016/j.optlastec.2019.03.008. URL `https://www.sciencedirect.com/science/article/pii/S0030399219300878`.

[71] William F Krupke. Diode-pumped alkali laser, November 4 2003. US Patent 6,643,311.

[72] Benjamin Q Oliker, John D Haiducek, David A Hostutler, Greg A Pitz, Wolfgang Rudolph, and Timothy J Madden. Simulation of deleterious processes in a static-cell diode pumped alkali laser. In *High Energy/Average Power Lasers and Intense Beam Applications VII*, volume 8962, page 89620B. International Society for Optics and Photonics, 2014.

[73] Guofei An, You Wang, Juhong Han, He Cai, Zhigang Jiang, Ming Gao, Shunyan Wang, Wei Zhang, Hongyuan Wang, Liangping Xue, et al. Deleterious processes of a diode-pumped cesium vapor hollow-core photonic-crystal fiber laser. *High Power Laser Science and Engineering*, 4, 2016.

[74] A Tam, G Moe, and W Happer. Particle formation by resonant laser light in alkali-metal vapor. *Physical Review Letters*, 35(24):1630, 1975.

[75] A Badalyan, V Chaltykyan, Yasuhiko Fujii, Yu Malakyan, Masaki Ozawa, A Papoyan, and S Shmavonyan. Studies of laser induced cesium and rubidium hydride formation in vapor cells and their application for isotope separation. *Progress in Nuclear Energy*, 47(1-4):389–396, 2005.

[76] B Sayer, M Ferray, J Lozingot, and J Berlande. Experimental investigation of cesium hydride formation by reactive interaction between cs (7 p) and h2 molecules. *The Journal of Chemical Physics*, 75(8):3894–3903, 1981.

[77] Valeriy N. Azyazov, Aleksei P. Torbin, Alexander M. Mebel, Sean M. Bresler, and Michael C. Heaven. Product channels of the reactions of Rb(62P) with H2, CH4and C2H6. *Journal of Quantitative Spectroscopy and Radiative Transfer*, 196:46–52, 2017. ISSN 00224073. doi: 10.1016/j.jqsrt.2017.03.032.

[78] Chun-Yen Cheng, Chien-Ming Wu, Guan Bo Liao, and Wang-Yau Cheng. Cesium 6s 1/2→ 8s 1/2 two-photon-transition-stabilized 822.5 nm diode laser. *Optics letters*, 32(5):563–565, 2007. doi: 10.1364/ol.32.000563.

[79] Clifford V Sulham, Greg A Pitz, and Glen P Perram. Blue and infrared stimulated emission from alkali vapors pumped through two-photon absorption. *Applied Physics B*, 101(1):57–63, 2010. doi: 10.1007/s00340-010-4015-9.

[80] M Alina Gearba, Jeremiah H Wells, Philip H Rich, Jared M Wesemann, Lucy A Zimmerman, Brian M Patterson, Randall J Knize, and Jerry F Sell. Collisional excitation transfer and quenching in rb (5 p)-methane mixtures. *Physical Review A*, 99(2):022706, 2019. doi: 10.1103/PhysRevA.99.022706.

[81] James Yardley. *Introduction to molecular energy transfer*. Elsevier, 2012. doi: 10.1016/B978-0-12-768550-2.X5001-4.

[82] A Sasso, W Demtröder, T Colbert, C Wang, E Ehrlacher, and J Huennekens. Radiative lifetimes, collisional mixing, and quenching of the cesium 5dj levels. *Physical Review A*, 45(3):1670, 1992. doi: 10.1103/PhysRevA.45.1670.

[83] MS Safronova, UI Safronova, and Charles W Clark. Magic wavelengths, matrix elements, polarizabilities, and lifetimes of cs. *Physical Review A*, 94(1):012505, 2016. doi: 10.1103/PhysRevA.94.012505.

[84] M Lukaszewski and I Jackowska. Fine-structure mixing in the 9d state of caesium induced in collisions with noble-gas atoms. *Journal of Physics B: Atomic, Molecular and Optical Physics*, 21(21):L659, 1988.

[85] J Marek. Radiative lifetime of the 8s, 9s and 7d levels of csi. *Physics Letters A*, 60(3):190–192, 1977. doi: 10.1016/0375-9601(77)90810-6.

[86] 张岩文 Zhang Yanwen, 万鸿飞 Wan Hongfei, 崔秀花 Cui Xiuhua, 戴康 Dai Kang, 吕磊 Lü Lei, 王睿 Wang Rui, and 沈异凡 Shen Yifan. Excitation Transfer in Rb(5D-7S)-He,Ar,H2 Collisions. *Chinese Journal of Lasers*, 36(8):2009–2013, 2009. ISSN 0258-7025. doi: 10.3788/CJL20093608.2009. URL `http://www.opticsjournal.net/Abstract.htm?jid=m00001&year=2009&vol=36&no=8&page=2009`.

[87] 姜铁, 刘静, 王淑英, 戴康, and 沈异凡. Cs (8s-4f)-ar, h2 的碰撞能量转移. *原子与分子物理学报*, (1):97–100, 2009.

[88] Tiffany L Correll, Vlasta Horvatic, Nicoló Omenetto, James D Winefordner, and Cedomil Vadla. Experimental evaluation of the cross-sections for the cs (6d)→ cs (7pj) and cs (6d5/2)→ cs (6d3/2) collisional transfer processes induced by he and ar. *Spectrochimica Acta Part B: Atomic Spectroscopy*, 61(6):623–633, 2006.

[89] Ricardo C Davila and Glen P Perram. Spin-orbit relaxation of cesium 7 2 d in mixtures of helium and argon. *Physical Review A*, 93(3):033418, 2016.

[90] Ricardo C Davila, Glen P Perram, and Ben Eshel. Time-resolved fine structure mixing of cesium induced by helium and argon. *Journal of Physics B: Atomic, Molecular and Optical Physics*, 50(22):225204, 2017.

[91] A Lagerqvist. *Arkiv. Fysik*, 8:83–95, 1954.

[92] A Lagerqvist. *Naturwissenschaften*, 40:268–269, 1954.

[93] A. Lagerqvist M. Hultin. *Arkiv. Fysik*, 2:471–505, 1951.

[94] J. F. Harrison, R. W. Field, and C. C. Jarrold. Comparison of CaF, ZnF, CaO, and ZnO: Their anions and cations in their ground and low-lying excited states. In *ACS Symposium Series*, pages 238–259. American Chemical Society, July 2002. doi: 10.1021/bk-2002-0828.ch011. URL `https://doi.org/10.1021/bk-2002-0828.ch011`.

[95] David P. Baldwin and Robert W. Field. Dispersed laser fluorescence spectroscopy of the perturbation facilitated $B^1\Pi$ – $b^3\Sigma^+$ (1, 1) band of CaO. *Journal of Molecular Spectroscopy*, 139(1):77–83, 1990. ISSN 1096083X. doi: 10.1016/0022-2852(90)90243-J.

[96] David P Baldwin and Robert W Field. The $F^1\Pi$–$A'^1\Pi$ (0, 0) and $B^1\Pi$–$A'^1\Pi$(1, 0) Green-Band transitions of CaO. *Journal of Molecular Spectroscopy*, 139(1): 68–76, jan 1990. ISSN 00222852. doi: 10.1016/0022-2852(90)90242-I. URL `https://linkinghub.elsevier.com/retrieve/pii/002228529090242I`.

[97] J.B. Norman, K.J. Cross, H.S. Schweda, M. Polak, and R.W. Field. *Mol. Phys.*, 66:235–268, 1989.

[98] David P. Baldwin, Ernest J. Hill, and Robert W. Field. Electron Affinity of O^- and Diabatic CaO(g) Integer Charge Potential Curves. *Journal of the American Chemical Society*, 112(25):9156–9161, 1990. ISSN 15205126. doi: 10.1021/ja00181a019.

[99] David P. Baldwin, Jeffrey B. Norman, Ron A. Soltz, Abha Sur, and Robert W. Field. The $e^3\Sigma^- - a^3\Pi$(0, 0) and $E^1\Sigma^- - A'^1\Pi$ (0, 0), (1, 1), and (2, 2) bands of CaO: Multistate deperturbation of the $e^3\Sigma$– (v = 0) $\sim c^3\Sigma^+$ (v = 1) $\sim E^1\Sigma^-$ (v = 0) system. *Journal of Molecular Spectroscopy*, 139(1):39–67, jan 1990. ISSN 00222852. doi: 10.1016/0022-2852(90)90241-H. URL `https://linkinghub.elsevier.com/retrieve/pii/002228529090241H`.

[100] Ronald F Marks, Richard A Gottscho, and Robert W Field. The CaO D, $d^{1,3}\ \Delta - a^3\Pi$ System: Sub-Doppler Spectrum, Rotational Analysis, and Deperturbation. *Physica Scripta*, 25(2):312–328, feb 1982. ISSN 0031-8949. doi: 10.1088/0031-8949/25/2/010. URL `https://iopscience.iop.org/article/10.1088/0031-8949/25/2/010`.

[101] Ronald F. Marks, Hartmut S. Schweda, Richard A. Gottscho, and Robert W. Field. The orange arc bands of CaO. Analysis of a $D, d^{1,3}\Delta$–$a^3\Pi$ system. *The Journal of Chemical Physics*, 76(10):4689–4691, may 1982. ISSN 0021-9606. doi: 10.1063/1.442784. URL `http://aip.scitation.org/doi/10.1063/1.442784`.

[102] Robert W. Field, Gene A. Capelle, and C.R. Jones. The $A'^1\Pi - X^1\Sigma$ system of CaO. *Journal of Molecular Spectroscopy*, 54(1):156–159, jan 1975. ISSN 00222852. doi: 10.1016/0022-2852(75)90017-X. URL `https://linkinghub.elsevier.com/retrieve/pii/002228527590017X`.

[103] Robert W. Field. Assignment of the lowest $^3\Pi$ and $^1\Pi$ states of CaO, SrO, and BaO. *The Journal of Chemical Physics*, 60(6):2400–2413, mar 1974. ISSN 0021-9606. doi: 10.1063/1.1681375. URL `http://aip.scitation.org/doi/10.1063/1.1681375`.

[104] Steven F. Rice, Hans Martin, and Robert W. Field. The electronic structure of the calcium monohalides. A ligand field approach. *The Journal of Chemical Physics*, 82(11):5023–5034, 1985. ISSN 00219606. doi: 10.1063/1.448676.

[105] Janet N. Allison, Robert J. Cave, and William A. Goddard. Alkali oxides. Analysis of bonding and explanation of the reversal in ordering of the $^2\Pi$ and

$^2\Sigma$ states. *The Journal of Physical Chemistry*, 88(6):1262–1268, mar 1984. ISSN 0022-3654. doi: 10.1021/j150650a049. URL `https://pubs.acs.org/doi/abs/10.1021/j150650a049`.

[106] Charles W. Bauschlicher and David R. Yarkony. Electronic structure of CaO. I. *The Journal of Chemical Physics*, 68(9):3990–3997, may 1978. ISSN 0021-9606. doi: 10.1063/1.436312. URL `https://onlinelibrary.wiley.com/doi/10.1002/pssb.2220720264http://aip.scitation.org/doi/10.1063/1.436312`.

[107] Randall N. Diffenderfer and David R. Yarkony. The electronic structure of CaO. II. An MCSCF/Cl treatment of the low-lying $^1\Sigma^+$ and $^1\Pi$ states. *The Journal of Chemical Physics*, 77(11):5573–5580, 1982. ISSN 00219606. doi: 10.1063/1.443763.

[108] Hossain Khalil, Vincent Brites, Frédéric Le Quéré, and Céline Léonard. Ab initio study of the low-lying electronic states of the CaO molecule. *Chemical Physics*, 386(1-3):50–55, 2011. ISSN 03010104. doi: 10.1016/j.chemphys.2011.05.023. URL `http://dx.doi.org/10.1016/j.chemphys.2011.05.023`.

[109] H. Khalil, F. Le Quéré, V. Brites, and C. Léonard. Theoretical Study of the Rovibronic States of CaO. *Journal of Molecular Spectroscopy*, 271(1):1–9, jan 2012. ISSN 00222852. doi: 10.1016/j.jms.2011.10.004. URL `http://dx.doi.org/10.1016/j.jms.2011.10.004https://linkinghub.elsevier.com/retrieve/pii/S0022285211002645`.

[110] Junxia Cheng, Huajun Chen, Xijuan Zhu, and Xinlu Cheng. Theoretical study of the ro-vibrational spectrum of CaO molecule in its two X1Σ+ and A1Σ+ states. *Journal of Molecular Structure*, 1084:122–127, 2015. ISSN 00222860. doi: 10.1016/j.molstruc.2014.11.067. URL `http://dx.doi.org/10.1016/j.molstruc.2014.11.067`.

[111] Sergei N. Yurchenko, Audra Blissett, Usama Asari, Marcus Vasilios, Christian Hill, and Jonathan Tennyson. ExoMol molecular line lists –XIII. The spectrum of CaO. *Monthly Notices of the Royal Astronomical Society*, 456(4):4524–4532, mar 2016. ISSN 0035-8711. doi: 10.1093/mnras/stv2858. URL `https://academic.oup.com/mnras/article-lookup/doi/10.1093/mnras/stv2858`.

[112] Jonathan Tennyson and Sergei N. Yurchenko. ExoMol: molecular line lists for exoplanet and other atmospheres. *Monthly Notices of the Royal Astronomical Society*, 425(1):21–33, sep 2012. ISSN 00358711. doi: 10.1111/j.1365-2966.2012.21440.x. URL `https://academic.oup.com/mnras/article-lookup/doi/10.1111/j.1365-2966.2012.21440.x`.

[113] A.A. Berezhnoy, J. Borovička, J. Santos, J.F. Rivas-Silva, L. Sandoval, A.V. Stolyarov, and A Palma. The CaO orange system in meteor spectra. *Planetary and Space Science*, 151:27–32, feb 2018. ISSN 00320633.

doi: 10.1016/j.pss.2017.10.007. URL `https://linkinghub.elsevier.com/retrieve/pii/S0032063317302027`.

[114] C Focsa, A Poclet, B Pinchemel, R.J. Le Roy, and P.F. Bernath. Fourier Transform Spectroscopy of the $A'^1\Pi$–$X^1\Sigma^+$ System of CaO. *Journal of Molecular Spectroscopy*, 203(2):330–338, oct 2000. ISSN 00222852. doi: 10.1006/jmsp.2000.8187. URL `https://linkinghub.elsevier.com/retrieve/pii/S0022285200981876`.

[115] David P Baldwin and Robert W Field. The $C'^1\Sigma^+$ – $A'^1\Pi$ (0, 0) and (1, 1) bands of CaO. *Journal of Molecular Spectroscopy*, 133(1):90–95, jan 1989. ISSN 00222852. doi: 10.1016/0022-2852(89)90245-2. URL `https://linkinghub.elsevier.com/retrieve/pii/0022285289902452`.

[116] Jacob T Stewart, Michael N Sullivan, and Michael C Heaven. Near UV bands of jet-cooled CaO. *Journal of Molecular Spectroscopy*, 322: 18–21, apr 2016. ISSN 00222852. doi: 10.1016/j.jms.2016.02.009. URL `http://dx.doi.org/10.1016/j.jms.2016.02.009https://linkinghub.elsevier.com/retrieve/pii/S0022285216300236`.

[117] R.W. Field. Discussion of calcium oxide perturbations. personal communication.

[118] B. Ostojić, Per Jensen, P. Schwerdtfeger, and P. R. Bunker. Singlet-triplet interaction in Group 2 M_2O hypermetallic oxides. *Journal of Molecular Spectroscopy*, 301:20–24, 2014. ISSN 1096083X. doi: 10.1016/j.jms.2014.05.003. URL `http://dx.doi.org/10.1016/j.jms.2014.05.003`.

[119] B. Ostojić, Per Jensen, P. Schwerdtfeger, B. Assadollahzadeh, and P.R. Bunker. The predicted infrared spectrum of the hyperberyllium molecule BeOBe in its and electronic states. *Journal of Molecular Spectroscopy*, 263(1):21–26, sep 2010. ISSN 00222852. doi: 10.1016/j.jms.2010.06.008. URL `https://linkinghub.elsevier.com/retrieve/pii/S0022285210001359`.

[120] Houssam Salami and Amanda J. Ross. A molecular iodine atlas in ascii format. *Journal of Molecular Spectroscopy*, 233(1):157–159, sep 2005. ISSN 00222852. doi: 10.1016/j.jms.2005.06.002. URL `https://linkinghub.elsevier.com/retrieve/pii/S002228520500130X`.

[121] Robert J. Le Roy. LEVEL: A computer program for solving the radial Schrödinger equation for bound and quasibound levels. *Journal of Quantitative Spectroscopy and Radiative Transfer*, 186:167–178, jan 2017. ISSN 00224073. doi: 10.1016/j.jqsrt.2016.05.028. URL `http://dx.doi.org/10.1016/j.jqsrt.2016.05.028https://linkinghub.elsevier.com/retrieve/pii/S0022407316300978`.